Leveraging brain connectivity networks to detect mental states during motor imagery

Tiziana Cattai

Sorbonne Université
Ecole Doctorale Informatique, Télécommunications et Electronique
ARAMIS LAB at the Paris Brain Institute
&
University La Sapienza of Rome
Dept. of Information Engineering, Electronics and Telecommunication

Leveraging brain connectivity networks to detect mental states during motor imagery

Tiziana Cattai

Supervised by Fabrizio De Vico Fallani
and Stefania Colonnese

To be defended on 31/3/2021

Members of the jury :

- Congedo Marco, directeur de recherche, HDR, rapporteur
- Van De Ville Dimitri, professeur, HDR, rapporteur
- Pinna Andrea, maître de conférences, HDR, examinateur
- Scarano Gaetano, professeur, examinateur
- Colonnese Stefania, maître de conférences, co-directrice de thèse
- De Vico Fallani Fabrizio, chercheur, HDR, directeur de thèse

Abstract

The brain is a complex network and we know that inter-areal synchronization and de-synchronization mechanisms are crucial to perform motor and cognitive tasks. Nowadays, brain functional interactions are studied in brain-computer interface (BCI) applications with more and more interest. This might have strong impact on BCI systems, typically based on univariate features which separately characterize brain regional activities. Indeed, brain connectivity features can be used to develop alternative BCIs in an effort to improve performance and to extend their real-life applicability. The ambition of this thesis is the investigation of brain functional connectivity networks during motor imagery (MI)-based BCI tasks. It aims to identify complex brain functioning, re-organization processes and time-varying dynamics, at both group and individual level. This thesis presents different developments that sequentially enrich an initially simple model in order to obtain a robust method for the study of functional connectivity networks. Experimental results on simulated and real EEG data recorded during BCI tasks prove that our proposed method well explains the variegate behaviour of brain EEG data. Specifically, it provides a characterization of brain functional mechanisms at group level, together with a measure of the separability of mental conditions at individual level. We also present a graph denoising procedure to filter data which simultaneously preserve the graph connectivity structure and enhance the signal-to-noise ratio. Since the use of a BCI system requires a dynamic interaction between user and machine, we finally propose a method to capture the evolution of time-varying data. In essence, this thesis presents a novel framework to grasp the complexity of graph functional connectivity during cognitive tasks.

Keywords: Functional connectivity, signal processing, graph signal processing, brain-computer interface

Acknowledgements

First of all, I would like to thank Fabrizio De Vico Fallani, my thesis supervisor. Words are not enough to describe how precious he was during these years. Fabrizio taught me to think positive, to trust myself and not to be afraid, and a lot of BCI, connectivity and networks. Our discussions made this work passionate, and they were always an injection of confidence for me.

I would like to thank my thesis co-advisor Stefania Colonnese for having transmitted me her scientific rigour with sincere respect and affection. I am really grateful for our precious conversations about graph signal processing and statistics, but also about feminism and scout.

I would like to thank Dimitri Van De Ville and Marco Congedo to have read and evaluated this manuscript. Their comments were precious to precise and highlight some parts of the work. Then, I thank Andrea Pinna and Gaetano Scarano to be part of the jury. In particular, I sincerely thank Gaetano Scarano, for having been the first person to sincerely trust me and without whom this work would probably not exist.

The ARAMIS Lab was an extraordinary scientific laboratory, which has become a second home for me, where I learnt, discussed and laughed a lot. I can't start differently than by mentioning the ones who accompanied me during all these years. "C'est le S" means that we are a family and that's what they mean to me: Simona, because she is able to bring out the most cheerful part of me, because she is the person I can always count on, and because she is special although she doesn't know it yet. I can certainly say that I would not be the person I am today without her. Raphael, because he is a brother for me, with whom I can find myself on the top of a mountain or down in the catacombs (or only plan to do it) without losing the smile. He taught me to overcome limits and fears, but always having a person you can count on. Juliana, for her contagious smile and her extraordinary sensitivity, because she is reserved but once you enter her world, it is wonderful. For our fruitful and critical scientific discussions and her immeasurable help, for figures, presentations and anti-wrinkle treatments.

I would like to thank my twin sister Giulia, because she is a special and blunt friend, always there for me and from whom I have a lot to learn. I thank Igor, for his energy and curiosity, for being the scientific source of my knowledge on climate change, and, above all, for having shared his extra-lab life, which made me feel at home. I would like to thank all the other members of the ARAMIS team, because each of them left me something unforgettable: Alexandre R., because he is the most helpful person I know and because I know that I will always be able to count on him; Jorge, for his good mood; Pascal, because he is just extraordinary; and all the others with whom I shared some moments.

Vorrei ringraziare Lorenzo, per essermi sempre accanto con amore e per essere la mia casa in qualunque posto del mondo. Perché scoprire il mondo è bello, ma farlo insieme è meraviglioso.

Vorrei, infine, ringraziare i miei genitori, Gabriella ed Enrico, a cui tutte le parole di questa tesi e tutti i miei sforzi, sono dedicati. Perchè mi spingono a superare i miei limiti e a cercare sempre il meglio, e soprattutto perché credono in me sempre, molto di più di quanto non lo faccia io stessa.

Contents

Abstract **i**

Acknowledgements **ii**

List of Figures **xiii**

List of Tables **xv**

1 Introduction **1**

2 From brain signals to functional connectivity and graph analysis **4**
2.1 How to estimate brain connectivity from time series 4
2.2 Graph representation of brain connectivity networks 7
2.3 The Graph Signal Processing Framework 8
2.4 Representation of Time-Varying Networked Data 10

3 Graph connectivity estimation to detect mental states **14**
3.1 Introduction 15
3.2 Material and methods 16
3.2.1 Experimental protocol and preprocessing 16
3.2.2 Functional connectivity and brain network features 17
3.2.3 Statistical Analysis and Classification 19
3.3 Results 20
3.3.1 EEG network connectivity changes during motor imagery . . 20
3.3.2 Modulation of amplitude and phase synchronization between brain signals 22
3.3.3 Mental state detection in single individuals 24
3.4 Discussion 27
3.4.1 Methodological considerations 30
3.5 Conclusions 30
Appendix A: Example of Preprocessing 31

Appendix B: Brain connectivity changes during MI tasks in all frequency bands . . . 34
Appendix C: Coherence and imaginary coherence estimation for sine waves 36
Appendix D: Alternative state-of-the-art classification based on FBCSP . . 37
Appendix E: Classification analysis on BCI competition IV dataset 1 . . . 40

4 Improving graph connectivity estimation with graph signal processing 42
4.1 Introduction . . . 44
4.2 Related Work . . . 45
4.3 Signal Model . . . 47
4.4 Graph Connectivity Denoising . . . 49
4.5 Jensen divergence of connectivity states . . . 51
4.5.1 J-Divergence based Laplacian coefficients scoring . . . 55
4.6 Results on synthetic data . . . 56
4.6.1 Signal on Graph generation and connectivity estimation . . . 56
4.6.2 Subspace robustness on synthetic data . . . 60
4.6.3 J-divergence computation on synthetic data . . . 61
4.7 Real BCI measurements . . . 62
4.7.1 Experimental Protocol and Preprocessing . . . 63
4.7.2 J-divergence of brain connectivity states . . . 63
4.7.3 Scoring of Laplacian coefficients in beta band . . . 64
4.7.4 Short-time estimation of Laplacian coefficients in β band . . . 66
4.8 On the applicability in BCI systems: classification framework . . . 67
4.9 Conclusion and further work . . . 69
Appendix E . . . 70

5 Framework for short-time graph connectivity estimation 72
5.1 Introduction . . . 73
5.2 Deep L1-PCA computational framework . . . 73
5.3 Application to graph synthetic data . . . 77
5.3.1 Connectivity matrices simulation . . . 78
5.3.2 Robustness analysis via MSE . . . 79
5.3.3 Classification framework . . . 80
5.4 Results on real BCI data . . . 83
5.4.1 Experimental Protocol and Preprocessing . . . 83
5.4.2 Functional connectivity estimation procedure . . . 84
5.4.3 Classification analysis on real EEG data . . . 85
5.5 Deep L1-PCA applicability in BCI systems . . . 87
5.6 Conclusions . . . 88

6 Implementation of graph connectivity estimation on Inria OpenViBE software **90**
6.1 Introduction 91
6.2 Implementation of connectivity box 91
6.3 Results of of connectivity box 92
6.3.1 Connectivity estimation with synthetic data 92
6.3.2 Connectivity estimation with real EEG data 95
6.4 Performance tests 95
6.5 Conclusions and future work 96

7 Conclusions and future perspectives **98**

Bibliography **101**

List of Figures

2.1 Graphical representation of the most common functional connectivity estimators used in literature. They are organized in a coloured structure to identify different properties. We report undirected and directed estimators in green and red colours respectively. Then, they can be represented according to their ability to capture bivariate or multivariate interactions, in blue or green boxes. The characterization of possible non linearities is reported in grey boxes. 5

2.2 Main steps to estimate graph connectivity networks from time series. The first step is definition of graph nodes (i.e. the yellow circles on the left panel). From each node, brain signals are recorded. After choosing an appropriate FC estimator, functional connectivity is computed for each pair of nodes in order to obtain an adjacency matrix. Nodes and edges, corresponding to the elements in the adjacency matrix, constitute the final brain network. 8

2.3 Graphical representation of signals on graph with the underlying graph structure. 9

2.4 Example of network changing its edges in time (m) 11

3.1 Connectivity estimators as a function of normalized distance between EEG electrodes. Coherence values are in orange while imaginary coherence results are in green. Connectivity estimated are extracted from all the available experimental observations in the β frequency band. [31] ©2018 IEEE 18

3.2 Statistical contrast maps between motor imagery and resting states obtained with band power features. Results are shown for one-tailed permutation-based t-tests ($p<0.01$). In Panel A) the obtained t-values are illustrated for individual representative frequency bins within the *theta* band, B) *alpha* band, C) *beta* band, and *gamma* band. In the *beta* band, results also remained significant after correction for multiple comparison ($p<0.05$, FDR corrected). 20

3.3 Statistical contrast maps between motor imagery and resting states in the *beta* band. In panel *A*, we report the results in *beta* band for connectivity and node strength values. In panel *B*, we show the results of node strength for individual representative frequency bins within the *beta* band. Results for coherence-based features are in top line, while those for imagery coherence-based features are in bottom line. Only the twenty most discriminant values are represented here for illustrative purposes. 21

3.4 Statistical contrast maps between motor imagery and resting states in the *beta* band. In panel *A*, we report the results in *beta* band for connectivity and node strength values. In panel *B*, we show the results of node strength for individual representative frequency bins within the *beta* band. 23

3.5 Relationships of coherence/imaginary coherence with phase difference. In Panel A) coherence is in pink and imaginary coherence in green, showing the functional connectivity between two sine waves at 10 Hz as function of their temporal shift. The shift, corresponding here to a phase difference, varies from 0 to π in steps of π /500. At each shift value, the two connectivity estimators are evaluated. Panel B) shows the sine waves with different phase differences. In panel 1), a positive Δ of π /4 in panel 2), a negative Δ of $-\pi/4$. . . . 24

3.6 Phase difference properties and discrimination ability. Panel A), results of permutation-based t-tests in the *beta* band across all subjects are shown for brain networks reconstructed from the phase difference between EEG signals. Panel B) results of permutation-based t-tests obtained with node strength values extracted from the previous brain networks. Panel C), Spearman correlation plot between imaginary coherence and phase difference values considering all the connections including C3 electrode for one representative subject. . 25

3.7 Improvement of classification performance. Bar plots show the percentage of relative increment between the best combination of features (i.e., coherence-based node strength S^C, imaginary coherence-based node strength S^{IC} and power spectrum P. The pie diagram in the inset illustrates the percentage of times that a specific combination of features has been selected across subjects.Two different cases are considered, distiguished by a different color code. In blue, we report results of accuracy improvements when selected electrodes are located in controlateral sensorimotor area (Contra), i.e. FC5, FC3, FC1, C5, C3, C1, CP5, CP3, CP1. In red, results relate to classification analysis when electrodes are in both contralateral and ipsilateral sensorimotor areas (Contra+Ipsi), ie. FC5, FC3, FC1, C5, C3, C1, CP5, CP3, CP1, FCZ, CZ, CPZ, FC2, FC4, FC6, C2, C4, C6, CP2, CP4, CP6 27

3.8 Brain features selected by the classification procedure. The color codes for the group-averaged number of times that a specific feature - in the electrode-frequency space - has been chosen during the sequential feature selection algorithm. The results for P features are illustrated in the top line, those for S^C in the middle line and those for S^{IC} in the bottom line. Results relates to the classification analysis framework when only electrodes in the contralateral sensorimotor areas are selected. 28

3.9 EEG signals before the preprocessing for one subjects. We show the first 60s of recordings. 31

3.10 Independent component obtain with Infomax algorithm. We show the first 10 ICs and the first 60s of recording. For each component, both the signals and the associated topography are represented to facilitate the preprocessing procedure. 32

3.11 EEG signals after preprocessing for one subjects. We show the first 60s of recording. 33

3.12 Statistical contrast maps between motor imagery and resting states for connectivity features. In top line, we have results for coherence features and in the bottom line for imaginary coherence ones. In Panel A) results for coherence in *theta* band, in B) for imaginary coherence in *theta* band, in C) for coherence in *alpha* band, in D) for imaginary coherence in *alpha* band, in E) for coherence in *beta* band and in F) for imaginary coherence in *beta* band in G) for coherence in *gamma* band and in H) for imaginary coherence in *gamma* band . Only the twenty most discriminant connections are represented here for the sake of simplicity. 34

3.13 Statistical contrast maps between motor imagery and resting states for node strength features. In top line, we have results for coherence-based node strength features and in the bottom line for imaginary coherence ones. In Panel A) results for coherence in *theta* band, in B) for imaginary coherence in *theta* band, in C) for coherence in *alpha* band, in D) for imaginary coherence in *alpha* band, in E) for coherence in *beta* band and in F) for imaginary coherence in *beta* band in G) for coherence in *gamma* band and in H) for imaginary coherence in *gamma* band . Only the twenty most discriminant connections are represented here for the sake of simplicity. 35

3.14 FBCSP procedure. EEG signals recorded from N channels are band-passed in frequency intervals. Then, for each frequency interval, the common spatial pattern is computed. Finally, the posterior probability is estimated in order to weight CSP features to perform a classification fusion to integrate different type of features. 37

3.15 Scheme of the fusion procedure. Each type of feature is computed and used to train a classifier. Then, the posterior probability is computed in each case and a Bayesian approach is used to integrate the different features. 38

3.16 Improvement of classification performance. Bar plots show the percentage of relative increment between the best combination of features (i.e., coherence-based node strength S^C, imaginary coherence-based node strength S^{IC} and common spatial pattern CSP. The pie diagram in the inset illustrates the percentage of times that a specific combination of features has been selected across subjects. 38

3.17 Improvement of classification performance. Bar plots show the percentage of relative increment between the best combination of features (i.e., coherence-based node strength S^C, imaginary coherence-based node strength S^{IC} and power spectrum P. The pie diagram in the inset illustrates the percentage of times that a specific combination of features has been selected across subjects. 40

3.18 Brain features selected by the classification procedure. The color codes for the group-averaged number of times that a specific feature - in the electrode-frequency space - has been chosen during the sequential feature selection algorithm. The results for P features are illustrated in the top line, those for S^C in the middle line and those for S^{IC} in the bottom line. Results relates to the classification analysis framework when only electrodes in the contralateral sensorimotor areas are selected. 41

4.1 Example of transformation effect. In a) we have bidimensional Gaussian distributions which differ under mean and covariance matrix . In b) we have data in the transformed domain 52

4.2 J-Divergence contributions as function of mean η and standard deviation σ: a) $J^{(\sigma,\eta)}$ for variables whose conditional standard deviation differ under $\mathcal{H}_1$ and $\mathcal{H}_0$, and b) $J^{(\eta)}$ for variables with invariant conditional standard deviation. 55

4.3 Graphic interpretation of the score computed for the first element in the vector $\tilde{l}$ 56

4.4 Adjacency matrix with synthetic data. $\hat{\boldsymbol{A}}_{ij}$ is represented under $\mathcal{H}_1$ in A) and under $\mathcal{H}_0$ in panel B). 59

4.5 Example of eigenvectors on graph. They relate to the Laplacian matrix estimated from synthetic data under $\mathcal{H}_1$ 59

4.6 Results of Frobenius distance on synthetic data. Several perturbation configurations are represented: in panel a)σ_w=0 and σ_b=0,in panel b) σ_w=1.2 and σ_b=0,in panel c) σ_w=0 and σ_b=2 and in panel d) σ_w=1.2 and σ_b=2. In the different colors (in the legend) we represent the different subspaces. 61

4.7 Results of J-divergence analysis on synthetic data. Several perturbation configurations are represented: in panel a) σ_w=0 and σ_b=0, in panel b) σ_w=1.2 and σ_b=0, in panel c) σ_w=1.2 and σ_b=2. In the different colors (shown in the legend) we represent the different subspaces for the filtering. 62

4.8 Results of J-divergence analysis for real EEG data. We report the cumulative J-divergence CJ_n as function of the first 20 variables. In the different colors (shown in the legend) we represent the different subspaces used to filter Laplacian. 64
4.9 Results of score computation for real EEG data. All the eigenvectors are considered (i.e. $\mathcal{U}_{ALL}$) in panels a,c);and results associated to the proposed denoising algorithm (ie. $\mathcal{U}_{L\cup H}$) in panels b,d). In the first line, score values refer to links (i.e. extra-diagonal elements) and in the second line, they refer to elements in the principal diagonal (i.e. nodes). For sake of clarity, in all the figures we plot the 20 nodes or links with highest score. 65
4.10 Results of J-divergence analysis over a moving window on real data. We plot the J-divergence over $M = 9$, 1s long, time intervals with 50% overlapping, versus the time interval index. The J-divergence is computed in β band and averaged across subjects. 67
4.11 Procedure for classification with denoised data. The score computation is used to select features from training data to perform the classification in the testing phase. This scheme represent one fold and one repetition. In our classification, we perform a 10-repeated 10 fold LDA classification. 68

5.1 General Deep L1-PCA computation structure. 74
5.2 A) Time-variant bidimensional normal data and in B) the underlying probability density function (PDF) orientation. 77
5.3 Time-variant data and first order L1-PCA approximation at different layers : layer 1 in A), layer 2 in B) and layer 3 in C). 78
5.4 Graphical representation of Deep L1-PCA computation with an $M = 8$ original data Ξ. At each layer k ($k = 1, 2, 3$) the L1-PCAs $\mathbf{r}_k(m)$ are computed and they become the input in $\mathbf{R}_{k+1}(m)$ for the next layer. 80
5.5 Mean squared error map computed on simulated data between the degree matrix corrupted by noise with $\sigma_w = 0.6$ and its reference version (i.e. without perturbations). 81
5.6 Accuracy of classification framework for synthetic data for each layer and each batch. In the rows we have the different layers and in the columns we have the batches, which are 4 at the first layer, 2 at the second and 1 batch at the final layer. In panel A), we report accuracy results when only the Laplacian diagonal elements are taken as classification features. In panel B) results are obtained when all the Laplacian elements are considered. 82

5.7 Accuracy of classification framework for real EEG data associated to each layer and each batch. In the rows we have the different layers and in the columns we have the batches, which are 4 at the first layer, 2 at the second and 1 batch at the final layer. In panel A), we report accuracy results when only the Laplacian diagonal elements are taken as classification features. In panel B) results are obtained when all the Laplacian elements are considered as features. 86

5.8 Graphical representation of data recordings. As the time passes, we collect m time-windows in which we can estimate the graph Laplacian. As soon as new time intervals are recorded we can compute the Deep L1-PCs at several layers. Here, we indicate with red arrows the time instant (and the associated time interval) in which we can reach an higher level. In fact, after 500ms, we have the first Laplacian estimation and the first classification can be performed. After the second interval (i.e. at 1s) the first L1-PCs can be computed. We have to wait until 2s (i.e. the $4th$ interval) to collect all the samples to complete the first layer with $k = 1$ and to perform the second L1-PCA, reaching the second layer. At 4s, we have all the samples needed to compute the last L1-PCA. 88

6.1 Example of box code in OpenViBE including connectivity estimation. The connectivity measurement box is highlighted in red. 92

6.2 Configuration parameters for connectivity estimation. 93

6.3 Results of OpenViBE connectivity estimation through a novel visualization box. In the first row, we have results at 16 Hz, while in the second row, we have results for 64Hz. Right panels report results for spectral coherence and left panels those related to imaginary coherence. 94

6.4 Results of OpenViBE connectivity estimation on real EEG data. We report results at 16 Hz. Left panel shows results for spectral coherence and right panel those related to imaginary coherence. In this representation; A: Cz;B: CPz;C: C2;D: CP2;E: C4;F: CP4; G: C1; H: CP1 95

6.5 OpenViBE performance in terms of computational time for coherence (C) and imaginary coherence (IC)estimations. Results are shown for two computers (PC "Alienware" and PC "MSI"). 96

List of Tables

3.1 Table of main notation in Chapter 3. 16

3.2 Spearman correlation coefficient between IC and Δ for links including C3 for each subject. 24

3.3 Average accuracy across cross-validation fold and repetitions is reported the best feature combination for each subject. In the top rows, we have classification results obtained when selected electrodes are located in both in contralateral and ipsilateral sensorimotor areas, ie. FC5, FC3, FC1, C5, C3, C1, CP5, CP3, CP1, FCZ, CZ, CPZ, FC2, FC4, FC6, C2, C4, C6, CP2, CP4, CP6. In the bottom rows, results come from classification framework including only contralateral electrodes, ie.FC5, FC3, FC1, C5, C3, C1, CP5, CP3, CP1. . . . 26

3.4 Average accuracy across cross-validation is reported for each subject and each combination of feature when CSP is used. 39

4.1 Table of main notation in Chapter 4f. 46

4.2 J-divergence values on synthetic data. We report in bold characters the highest J-divergence value for each perturbation configuration. . 62

4.3 J-divergence values obtained with real EEG data. We highlight with bold characters the highest J-divergence value. 63

4.4 Accuracy values for 10-repeated 10 fold classification. We report results in absence of denoising ($\mathcal{U}_{ALL}$), and with our Laplacian denoising algorithm ($\mathcal{U}_{L\cup H}$). 69

5.1 Table of main notation in Chapter 5. 74

5.2 Classification accuracy for synthetic data related to the original $M = 8$ observations. In the first row, we have accuracies when only the Laplacian diagonal elements are taken as classification features. In the second row, accuracy values relates to when all the Laplacian elements are considered. 83

5.3 Classification accuracy for real EEG data related to the original $M = 8$ observations. In the first row, we have accuracies when only the Laplacian diagonal elements are taken as classification features. In the second row, accuracy values relate to when all the Laplacian elements are considered as features. 86

Chapter 1

Introduction

Functional connectivity (FC), measuring statistical dependences between different brain signals, captures crucial information to investigate brain functioning during cognitive tasks. Indeed, we currently interpret the brain as a complex network [14, 183], where neurons belonging to different regions collaborate to integrate information through anatomical and functional connections [27]. The possibility to explore brain interaction mechanisms in cognitive tasks, such as those involved during brain-computer interface (BCI) experiments, is gaining more and more interest [50, 69].

This thesis aims to provide new insight by adopting a signal processing and graph signal perspective for the application of functional brain connectivity in the BCI context. In particular, we intend to study the importance of brain interactions in the characterization of brain states. We specifically focus on the study of motor imagery-based BCIs.

BCIs are communication systems in which the interaction between the subject and the external world is realized without the peripheral neuro-muscolar activity [207, 209, 210]. BCI systems are based on the identification of mental states from brain signals, and because they depend on the subject's ability to voluntarily modulate the brain activity, they are being increasingly investigated for control, communication and rehabilitation [208]. Unfortunately, the real-life applicability of BCIs is still limited. It is estimated that a significant percentage of users (around 30%) cannot correctly interact with the interface (i.e. reaching the accuracy level needed to control BCIs) because BCIs are not simple systems and even trained subjects might not be able to voluntarily modulate their brain activity. This phenomenon is generally indicated as BCI-inefficiency [191, 199] and it globally limits the usability of BCI systems in clinical applications [38, 180].

In the last decade, great effort has been made to improve of BCI accuracy. One

possibility consists in finding the best mental strategy to identify the user's intent, looking for the most suitable feedback to efficiently interact with the subject [86, 160, 173]. Another possibility concerns the development of advanced classification algorithms to improve the detection of the user intention, using refined signal processing tools to improve signals' characterization [106, 107]. These methods are able to enhance BCIs performances, but they are blind to the brain mechanisms underlying the classification and they do not allow a clear neuro-physiological interpretation. This aspect has a crucial importance in most clinical applications, where the brain's structure or functioning is damaged and other solutions able to take it into account are needed.

This thesis aims to present a possible solution. It consists in looking for alternative features, able to characterize brain functional mechanisms involved during complex tasks, such as motor imagery [50, 69]. Functional connectivity (FC) describes interactions between spatially distributed areas by evaluating functional dependencies between activities localized in different regions [16]. Those features appear more representative of brain processes than univariate ones, such as power spectral density [89, 100, 139].

Our first question is to investigate the actual possibility of applying functional connectivity and basic graph estimators to characterize mental states. To answer this question we consider two state-of-the-art FC estimators, i.e. the spectral-coherence and imaginary-coherence [16, 69, 77]. We find that integrating network-based features enables a better characterization of brain states and we uncover the presence of a twofold mechanism of amplitude and phase synchronization between brain signals during motor imagery. At the same time, the inclusion of FC-based features in the classification, generally allows to increase the accuracy in the detection of the user's intent, with respect to standard univariate techniques only.

After testing the potential of graph connectivity features in the identification of mental states, we ask what improvement in states' separability can be obtained through robust functional connectivity estimation. To understand it, we use tools from different fields, from neuroscience to signal processing and graph signal processing [52, 135, 178]. We develop an original algorithm to denoise the graph Laplacian in order to obtain a more robust graph FC estimation. This procedure simultaneously preserves the signal-to-noise ratio and the graph connectivity properties. The validity of the denoising algorithm is verified by measuring the distance between Laplacians related to two states. The distance between those mental states is quantified with a novel formulation of the Jensen divergence [15].

Then, we present a new framework to provide short-time estimations of graph

functional connectivity to discriminate different mental states. To study the dynamics of time-variant signals, we introduce an innovative formulation of the classic norm-1 principal component analysis (L1-PCA)[113], suitable to obtain the description of the dynamics of time-varying signals. We apply this framework to simulated and real EEG BCI data including a classification procedure, with the final goal of identifying the brain state at each time-interval.

Taken together, these elements provide fresh evidence towards the application of graph functional connectivity and graph descriptors to BCI applications.

To test the feasibility of our approach, we finally implement a new box into the Inria Openvibe sofwtare, dedicated to real-time BCI processing. [159]. We finally show the applicability of the new box in terms of computational time.

This dissertations proceeds as follows. **Chapter** 2 presents an overview of the state-of-the-art procedures to extract functional brain networks from time signals and to analyse graphs, using graph theory and graph signal processing tools. **Chapter** 3 shows the application of functional connectivity and graph based features to motor imagery-based BCI data. **Chapter** 4 describes the denoising algorithm to filter graph connectivity and it presents a novel formulation of the Jensen divergence to measure separability. **Chapter** 5 presents the framework for time-varying graph FC estimation by means of iterative application of L1-PCA. **Chapter** 6 concludes the dissertation and presents future developments of this research.

Chapter 2

From brain signals to functional connectivity and graph analysis

Modern neuroscience has started with the characterization of the human brain as a system of interacting neurons [158]. Indeed, research has demonstrated that the brain is not constituted by isolated systems, but neurons cooperate and interact [14, 90] to perform complex tasks. Today we interpret the brain as a complex network [183] and new techniques have been developed to deeply investigate its functioning by merging different fields, such as network theory and graph signal processing [52, 81, 84, 116, 143].

These methodological advances have provided novel insights into fundamental and clinical neuroscience as well as into several applications from neuro-rehabilitation, to disease modelling and therapy [49, 59, 73, 138]. This includes the study of BCIs, which have been mainly explored by using univariate brain features [89, 139]. Indeed, functional connectivity and network features have been recently applied in BCI-applications [69, 77]. However, state-of-the-art results do not uniquely show the advantage of using those features instead of classical univariate ones [77].

To facilitate the reader in the comprehension of the advanced methods presented here, we are going to propose in the following a concise overview of the state-of-the-art associated to FC estimation from time series data, graph signal processing theory and models to capture time-varying dynamics. Note, that a more specific bibliography is directly presented in each chapter.

2.1 How to estimate brain connectivity from time series

In the last decades, many methods have been proposed to measure functional interactions between brain signals, based on tools coming from several domains,

from signal processing to information theory. Although each estimator has its own characteristics, the general idea consists in quantifying the functional dependencies between each pair of signals.

The first distinction between FC estimators is between those able to capture mutual interactions and those able to quantify causal information flows [52]. We commonly refer to them as undirected and directed estimators, respectively. Further distinctions can be done according to the possibility to capture linear or non linear interactions, or to measure bivariate or multivariate connections, or the potential to quantify FC in time or in frequency domain, as well as to describe time-varying dynamics [16]. In Fig. 2.1, we graphically present some examples of FC estimators, organized in a subjective way. We remark that it is a non-exhaustive list and other distinctions are possible.

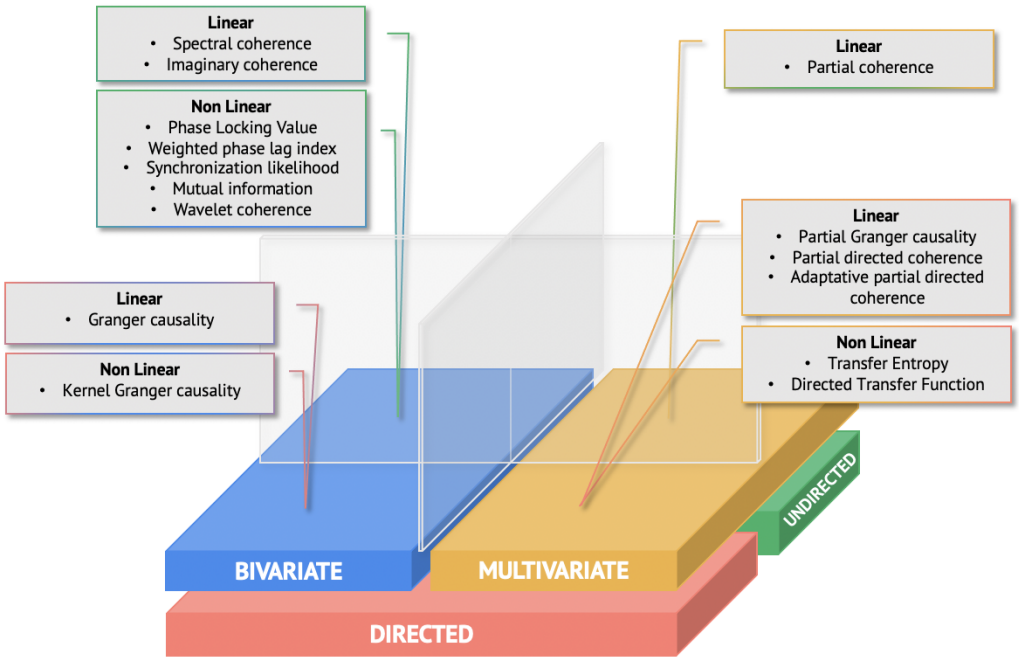

Figure 2.1: Graphical representation of the most common functional connectivity estimators used in literature. They are organized in a coloured structure to identify different properties. We report undirected and directed estimators in green and red colours respectively. Then, they can be represented according to their ability to capture bivariate or multivariate interactions, in blue or green boxes. The characterization of possible non linearities is reported in grey boxes.

The choice of the FC estimator can be a tricky task [52]. Comparative studies between several FC estimators have been proposed, but conclusions are not unambiguous since methods' performances depend both on the estimator itself and

data characteristics [11, 97, 203]. A first possible approach consists in applying all the methods to converge in the same estimation. This procedure completely lacks rationale because each estimator measures the signals' interactions in a different way and it captures different properties [16].

The key solution to choose the connectivity estimator consists in a clear hypothesis according to the specific study. In practice, the scientific question underlying the research naturally determines the appropriate FC estimator. We consider as example the case of epileptic crises, which are episodes characterised by the increasing of brain activity causing convulsions or loss of awareness. A nonlinear estimator provides an appropriate description of this transient and rapid phenomenon. Since the epileptic crisis generally starts in the temporal lobe to propagate throughout the cortex, a directed method can be suitable to identify information sources [196]. In this scenario, kernel Granger causality can be applied [111]. Otherwise, if researcher are interested is the identification of synchronization mechanisms during the crisis, an undirected measure will be used, such as phase-locking value [9], mutual information [198], or wavelet coherence [39].

Some other technical aspects guide the choice of the FC estimator [78]. In fact, the study of rhythmic oscillatory phenomena requires a particular attention. Estimators defined in the frequency domain, such as the classical spectral coherence [30] and directed transfer function (DTF) [93], are suitable for the investigation of FC behaviours defined in frequency bands. Time signals can be transformed in the frequency domain through parametric (i.e. autoregressive models) or non parametric (i.e. Fourier or Hilbert transform). Since signals lie in the frequency domain, the frequency band of interest can be easily extracted. In the case of FC estimators defined in time-domain, like partial Granger causality [213] and transfer entropy [198], band passing procedure can be applied.

Another important element to correctly choose the FC estimator is the available type of neuro-imaging data, because different techniques correspond to different temporal resolutions. EEG and MEG signals are characterized by high temporal resolution, in order of milliseconds, while fMRI typically have low time changes, in the order of seconds. Consequently, frequencies describing the EEG or MEG activities spans a broad interval, from portions of Hz to 100 Hz, according to the subject condition and the experiment [6, 17, 214]. Conversely, fMRI data are characterized by a limited frequency range (less than 1 Hz) and FC estimators defined in time-domain are more appropriate [61].

In [69], we presented in detail state-of-the-art FC estimators with some associated critical aspects, such as the ability of some FC estimators to avoid the presence of spurious connections (e.g. imaginary coherence [131], partial directed

coherence [168]) or to capture non-linear interactions (e.g. mutual information [198] and phase amplitude synchronization [9]).

2.2 Graph representation of brain connectivity networks

To build a brain network, the first step consists in the identification of nodes and edges. The graph nodes are typically defined according to the specific neuroimaging technique used to extract the brain data. For voxel-based techniques, like fMRI and PET, nodes classically correspond to regions of interests (ROIs), identified using anatomical atlas [43, 166]. For sensor-based techniques, such as EEG and MEG, nodes usually correspond to recording sensors [101]. In this latter case, brain nodes lies at the scalp level, but source-reconstruction techniques can be applied to re-define nodes on the cortex [56, 91].

Neuroimaging techniques measure in specific modalities brain regional activities, without having access to their mutual relationships. Consequently, the edges' weights have to be inferred from signals through statistical procedures. Functional connectivity (FC) estimators, described in the previous section, are typically used to quantify links in a graph setting.

Considered together, nodes and links give rise to a new type of networked data, which cannot be analysed with standard techniques but requires appropriate tools coming from network science, a research domain merging graph theory, statistical mechanics and inferential modelling [3]. Network science provides a novel perspective to analyse interacting data at several level [22, 186]. The networks of traffic movements, social relationships and molecular or protein interactions are only some examples [8, 79, 155, 201] . In this scenario, a complex network is modelled as a graph [129]. A graph $G = \{V, E, \boldsymbol{A}\}$ is defined as a set of nodes (or vertices) V with $|V| = N$, a set of links (or edges) E and an adjacency matrix $\mathbf{A}$ [129]. The $A_{i,j}$ element differs from zero if there is a link $e = (i, j)$ between the nodes i and j. At this stage, the graph is fully connected and weighted.

Widely used techniques in network domain involve thresholding strategies to reduce the number of links or to obtain a binary adjacency matrix. Reducing graph links provides advantages in improving the interpretabilty and mitigating false connections [53, 179]. The most intuitive way to proceed consists in defining a threshold on the number of edges or on the functional connectivity values. This simple approach is parametric and the same analysis has to be often performed several times before obtaining stable results. Another possibility is to use nonparametric methods, based on the statistical or topological properties of the network [53, 194]. After thresholding, networks can be weighted or unweighted,

depending on whether the links' weights are binarized. In Fig. 2.2, we report a graphical representation of the main steps needed to estimate graph connectivity networks from time series.

Once the graph is completely defined through its nodes and edges, it is possible to extract some metrics, which concisely capture graph topological properties [69]. Network properties are defined at several scales. At a local scale, which refers to the node level, we typically have measures quantifying the node importance in the network. One example is the node strength which is computed as the weighted sum of the links including a node. At a meso-scale, which is denoted as the node group level, measures of nodes' tendency to group are defined. One example is the study of modules and communities. At the global-level, we study properties related to the information transfer in the graph, such as global- or local-efficiency [60].

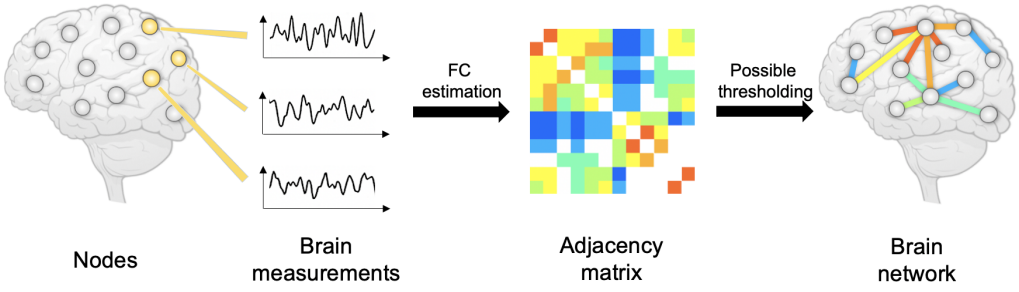

Figure 2.2: Main steps to estimate graph connectivity networks from time series. The first step is definition of graph nodes (i.e. the yellow circles on the left panel). From each node, brain signals are recorded. After choosing an appropriate FC estimator, functional connectivity is computed for each pair of nodes in order to obtain an adjacency matrix. Nodes and edges, corresponding to the elements in the adjacency matrix, constitute the final brain network.

2.3 The Graph Signal Processing Framework

There are many tools coming from different domains which are suitable to analyse graphs from different perspectives. This section presents graph signal processing (GSP) [167] tools from a theoretical and practical point of view. The goal of GSP is to develop signal processing methods for data defined over graphs [135]. Signals defined over graphs (SoGs) are a set of values lying on the graph nodes, linked by edges. Fig. 2.3 graphically shows SoGs with the underlying graph structure.

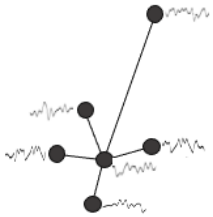

Figure 2.3: Graphical representation of signals on graph with the underlying graph structure.

Graph signals have properties, as in signal processing, which have to be redefined in the specific scenario of graphs. For instance, one classical property is the smoothness, but the signal smoothness in this context needs to be defined. A smooth SoG can be a signal assuming similar values in close nodes. At the same time, smoothness can be referred to the frequency domain [135].

Even basic and intuitive concepts in classical signal processing become challenging where signals are defined over a graph. One example is the translation operation, which does not have a direct meaning in the graph setting because the shift invariant property is not defined on irregular domains [167]. Also the downsampling procedure, consisting on eliminating some samples in the classical signal processing, here is tricky because of the vertex dimension [135, 187].

Another fundamental tool in signal processing is the Fourier Transform, which has been redefined as Graph Fourier transform (GFT) [178] in GSP. For the presentation of this transformation, a step back is needed. After defining the edges' weights obtaining the adjacency matrix **A**, we can compute the graph Laplacian, as follows:

$$\boldsymbol{L} = \boldsymbol{D} - \boldsymbol{A} \tag{2.1}$$

where $\boldsymbol{D}$ is the degree matrix, which is a diagonal matrix collecting in the i-diagonal element the sum of the edges including the node i.

We identify the set of orthonormal eigenvectors $\{\boldsymbol{u}_i\}_{i=0,1,...,N-1}$, where N is the number of graph vertices. $\{\boldsymbol{u}_i\}$ relates to increasingly ordered eigenvalues $0 = \lambda_0 \leq \lambda_1 \leq \lambda_2 ... \leq \lambda_{N-1} = \lambda_{max}$.

Laplacian eigenvectors $\{\boldsymbol{u}_i\}$ play a fundamental role in GSP. In fact they are used as signals on graphs (**s**) and they represent a basis for the Graph Fourier Transform. The GFT for SoG **s** is computed as the projection of the SoG on the Laplacian eigenvectors:

$$\hat{s}(\lambda_l) = \boldsymbol{s}^H \boldsymbol{u}_l \tag{2.2}$$

Graph Laplacian eigenvalues defined in the graph setting, have the similar notion of frequencies in the classical Fourier transform. Indeed, small eigenvalues correspond to eigenvectors which have small variation on connected vertices. Conversely, eigenvectors associated to large eigenvalues rapidly vary over connected nodes [135, 145, 178].

These considerations on graph eigenvectors will be used in Chapter 4 to define the denoising algorithm.

Among the other applications, GSP has been recently leveraged in brain network scenarios [81]. Indeed, GSP can be applied to neuroimaging data and it provides tools to simultaneously investigate brain structure, contained in the graph, and the brain functioning, contained in the SoGs [121]. Medaglia et al. in [115] applied the GSP metrics of alignment and liberality to deepen the problem of attention switching with fMRI data. Findings show that subjects characterized by signals aligned with white matter structure can switch attention more rapidly. The same metrics (i.e. alignement and liberality, deriving from spectral graph filtering) have been applied by Bolton et al. in [23] to predict behavioural variables, such as cognitive features, task skills and motor abilities. Specifically, authors studied the presence of temporal dynamics in the alignment and liberality. Results from the temporal investigation, have demonstrated the possibility of detecting network transitions through changes in GSP metrics.

Graph signal processing has recently been applied for brain-computer interface applications. Petrantonakis et al. [144] have used GSP tools to extract novel features to improve the classification performances in NIRS-based BCIs systems.

Taken together, these first results show potential in the application of GSP to brain data analysis. In fact, GSP provides complete and flexible tools to analyse interacting systems, which find application in brain behaviour investigation at several levels and in a large set of applications, such as BCIs.

2.4 Representation of Time-Varying Networked Data

Nowadays networked data are studied by different perspectives and with several innovative tools. One intrinsic property characterizing almost all the data is the time-varying evolution. Social, biological, traffic networks change their descriptors in time and investigation tools must be able to capture this dynamic behaviour [95, 156]. Concerning the brain investigation, many studies limit the analysis to static functional connectivity networks, assuming that the interactions between brain

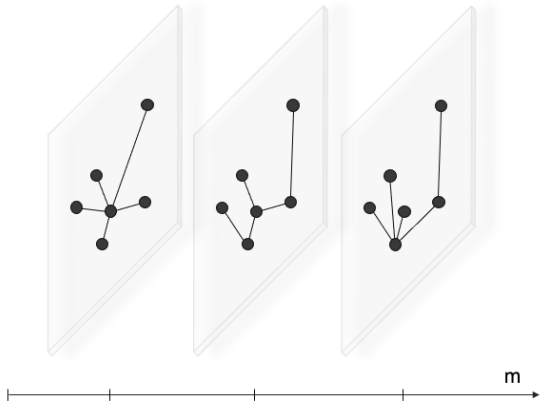

Figure 2.4: Example of network changing its edges in time (m)

signals are stationary. Today we know the brain coupling mechanisms are time-varying processes [24, 36, 172] with a dynamic alternation of synchronizations and desynchronizations that constitutes the basis for many neuro-physiological tasks, as perception and memory [62, 82].

In order to investigate the time-varying brain functioning, the simplest strategy is to reduce the length of the time interval, considering sliding windows with possible overlap. While reducing the time windows assures the signal (quasi) stationarity, the reliability of the FC estimates can rapidly decrease. This situation becomes even more critical when multivariate or non-linear FC estimators are adopted, since they need even longer time signals to compute reliable estimates [126, 142].

To overcome this limitation, a possible strategy for time-varying FC estimation consists in using techniques specifically designed for non-stationary signals, such as detrended fluctuation analysis [68] and wavelet transformation [39]. Among the other FC measures [69], some have been specifically developed for time-varying scenarios, such as wavelet coherence [189] and adaptive partial directed coherence [168].

This is a first-level analysis that deals only with short-time FC estimation procedures. Another possibility is to go further and model graph temporal evolution. Fig. 2.4 represents an example of network changing its edges over time windows.

One strategy is presented in [137], where Ozdemir et al. performed a tensor decomposition of FC networks. The proposed algorithm enables to track time-varying connectivity networks, extracted from brain EEG data. This method firstly performs a decomposition of the graph Laplacian into a low rank + a sparse structure. Then, a tracking algorithm gradually updates subspaces at each new

time interval. The hypothesis behind this decomposition is that FC slowly changes across time. As a consequence, the FC is modelled as a low rank matrix while the sparse component models noise and outliers. Shen et al. developed in [176] an alternative algorithm to track $3-D$ tensor representing time-varying graphs. In this study, authors proposed an original structural equation model (SEM), which requires a tensor decomposition, obtained by means of the well-known parallel factor decomposition [96].

State-of-the-art graph learning methods use either simplified graph models for SoGs or models that are more expensive in terms of computational cost. In the case of time-varying graphs, these aspects are even exacerbated. Ghoroghchian et al. [66] proposed a graph learning method based on representation learning on graphs. Specifically, the representation learning algorithm produces embeddings for graph vertices, by considering neighbouring nodes. This procedure was tested on intra-cranial electroencephalographic (iEEG) data recorded from epileptic patients.

In the context of graph learning, many recent studies address the problem of time-varying graph characterization by assuming the smoothness on the temporal domain [66, 125]. In this direction, Kalofolias et al. [92] and Yamada et al. [212] proposed advanced optimization algorithms. Specifically, in [212], authors introduced a method to combine several regularizations for graph learning applications even when few observations are available. Jiang et al. [87] developed a model to characterize graph temporal evolution in human connectome. Authors mathematically describe the problem as a quadratic objective function on graph vertices across short-time intervals. A regularization procedure is applied to reflect the smoothness and other properties, such as the graph Laplacian evolution.

Another strategy consists in modelling the spatio-temporal structure of a $3-D$ graph. To this aim, Romero et al. [161] developed a kernel-based decomposition. The advantage of this method consists in simultaneously estimating the graph structure on time and space domain, with a reduction of the number of vertices to be analysed. Liu et al. [105] proposed an alternative way to estimate $3-D$ graph, by introducing a different algorithm based on smoothness prior to learn the graph and simultaneously identify the time-correlation pattern.

Ortiz et al. [136] presented a different strategy based on the structure of product graphs, that, whenever obtained by applying Kronecker and Cartesian products, can be used for sampling and reconstruction applications. This method has broad applicability since product graphs can be used to model sensors' values acquired at different time points.

In [83], Isufi et al. developed a sampling procedure for time-varying SoGs, to

observe and track signals described by a linear state-space model. A mathematical study to identify the role of graph, graph signals and sample location is provided.

In conclusion, novel tools coming from different research domains pave the way for the study of brain organizational processes and time varying dynamics from an original perspective, constituted by merging signal processing, network theory and graph signal processing.

Chapter 3

Graph connectivity estimation to detect mental states

Functional connectivity (FC) is widely explored for its ability to capture functional interactions between brain signals. However, the role of FC in the context of brain-computer interface applications is still poorly understood. To address this gap in knowledge, we consider a group of 20 healthy subjects performing a motor imagery (MI) task. We study two state-of-the-art FC estimators, i.e. spectral- and imaginary-coherence, and we describe how they change during MI tasks. We characterize the resulting FC networks by computing the node strength of each EEG sensor and we compare its discriminant ability with respect to standard univariate features. At the group level, we show that while spectral-coherence based features increase in the sensorimotor areas, those based on imaginary-coherence significantly decrease. We demonstrate that this opposite, but complementary, behaviour is caused by the increase in amplitude and phase synchronization between the brain signals during MI task. At the individual level, we demonstrate the potential of network connectivity features in an *off-line* classification framework. Taken together, our findings offer new insights into the oscillatory mechanisms underlying brain network during MI task and open new perspectives to improve BCI performance.

In this chapter are reported figures and part of text from a submitted paper: Cattai, T., Colonnese, S., Corsi, M. C., Bassett, D. S., Scarano, G., & De Vico Fallani, F. (2019). Phase/amplitude synchronization of brain signals during motor imagery BCI tasks. arXiv preprint arXiv:1912.02745. [33]

3.1 Introduction

Based on the detection of cognitive states from brain signals, brain-computer interfaces (BCIs) are explored for control, communication and rehabilitation, via the ability of subjects to voluntary modulate their brain activity through mental imagery [207, 209, 210]. The ability to correctly identify the user's intent is therefore a key point to design BCI systems[5, 21, 29, 57, 191, 199].

In this direction, investigators have explored different approaches based on various theoretical and experimental perspectives. One possibility is to look for the best mental strategy to detect the user response or to identify the adapted feedback to convey the most relevant information to the user [2, 123, 200].

Another possibility is to develop advanced signal processing methods and sophisticated classification algorithms to improve the signal-to-noise ratio and to correctly identify the user's intent [106, 107]. Although these methods provide performance increments, they are intrinsically blind to the neural mechanisms that enable to identify the user's cognitive state and may not have a direct physical or physiological interpretation[195]. However, this is crucial especially in clinical applications where brain functioning can be compromised and other solutions must be identified.

A different strategy consists in looking for alternative - potentially more informative - features reflecting the human brain organization processes. To this end, functional connectivity (FC) can be adopted to estimate the interaction between spatially distributed brain areas by quantifying the dependences between the regional activities [52]. In contrast to univariate features such as frequency band power, FC appears more appropriate to grasp the oscillatory network processes involved in brain (re)organization during cognitive tasks [50]. Recent studies have demonstrated the potential of FC features in BCI, albeit the results are variable and difficult to compare because of the different FC estimators, tasks and limited number of subjects [25, 77, 181, 205]. More importantly, the neurophysiological interpretation of FC features is still poorly understood in motor imagery tasks but this is crucial to eventually design alternative FC-based BCIs.

In order to investigate the actual possibility of applying FC features in BCI context, we consider two state-of-the-art FC estimators, i.e. the spectral coherence and imaginary coherence [30, 131]. From a theoretical perspective, these estimators bring complementary information because the first quantifies the synchronization between the signal amplitudes while the latter also depends on their phase difference [131, 162]. Our hypothesis is that the integration of these complementary features will allow a better characterization of the BCI-related cognitive

Notation	Description
C	spectral coherence estimate
IC	imaginary coherence estimate
Δ	phase difference
N	total number of nodes
S^C	coherence-based node strength
S^{IC}	imaginary coherence-based node strength
S^{IC}	phase difference-based node strength

Table 3.1: Table of main notation in Chapter 3.

states and that including them in the feature extraction block will improve the BCI accuracy as compared to standard approaches solely based on univariate features. To verify our predictions, we explore brain FC networks extracted from EEG data recorded in a group of 20 healthy subjects performing the motor imagery (MI) of the right hand. In order to compare our approach with power spectrum features (P), we compute for each sensor the node strength, an intuitive graph metric which describes for each node its overall connectivity within the network. At the group level, we statistically compare the spatial patterns obtained from graph-related features associated to motor imagery and resting state. At the individual level, we evaluate the discriminant potential of network metrics by means of an *off-line* classification simulation.

To facilitate the reader, we list in In Table 3.1 the main notation used in this chapter.

3.2 Material and methods

3.2.1 Experimental protocol and preprocessing

Twenty healthy subjects (aged 27.60 $\pm$ 4.01* years, 8 women), all right-handed, participated in the study. The subjects were recruited for a BCI training protocol and they did not have any medical or psychological disorder. The study was approved by the ethical committee CPP-IDF-VI of Paris and each subject signed a written informed consent. Each participant received financial compensation for the participation.

The BCI experiment consisted in a standard 1D, two-target box task [210]. The subject was in front of a screen with a distance of 90 cm. When the target was up, the subject was instructed to imagine moving his/her the right hand (i.e. grasping); when the target was down, the subject had to remain at rest. EEG

*mean and standard deviation

data were recorded with a 74-channel system, with Ag/AgCl sensors (Easycap, Germany) in a 10-10 standard configuration. The reference for the EEG signals were mastoid signals and the ground electrode was set on the left scalpula. Data were recorded in a shielded room. Impedances were lower than 20 kOhms, the sampling frequency was 1 kHz, then downsampled to 250 Hz. All the subjects were naive BCI users and participated in a training protocol. For each subject we collected 64 trials of motor imagery and 64 trials of resting state. In each trial, the first second corresponded to the inter-stimulus interval (ISI), when a black screen was presented to the subject. During the following 5s, the target appeared on the screen and during this period subjects had to imagine a sustained grasping of their right dominant hand. During the experiments, hand muscular activity was recorded with EMG (electromyogram) to check the presence of involuntary movements during the motor imagery tasks. On-line, the experimenter ensured that subjects were not generating muscular artefacts during the task. Off-line, all the recorded signals have been checked to exclude the presence of evident muscular artefacts. We remind the reader to [46] for a detailed description of the experiments.

A pre-preprocessing step preceded the analysis/ Specifically, we performed on the entire dataset an independent component analysis (ICA) to eliminate ocular and cardiac artefacts, via the Infomax algorithm [18] available in the Fieldtrip toolbox [133]. The ICA was operated by the visual inspection of both time signals and their associated topographies. We removed no more than two independent components in average. In Appendix A we report one example of preprocessing on the first subject.

3.2.2 Functional connectivity and brain network features

We consider two state-of-the-art functional connectivity estimators [16], i.e. spectral coherence (C) [30] and imaginary coherence (IC) [131].

While other FC estimators, directed and undirected, have been already applied in the BCI context [72, 75, 77, 98, 150], here we explore C and IC because of their relatively simplicity and intuitiveness.

Given two EEG time series y_i and y_j in a time interval T_s, the computation of C_{ij} and IC_{ij} at the frequency ω_k can be respectively obtained as:

$$C_{ij}(\omega_k) = \frac{\left|P_{ij}(\omega_k)\right|}{\left(P_i(\omega_k) \cdot P_j(\omega_k)\right)^{1/2}} \tag{3.1}$$

$$IC_{ij}[\omega_k] = \frac{\left|\Im\left(P_{ij}(\omega_k)\right)\right|}{\left(P_i(\omega_k) \cdot P_j(\omega_k)\right)^{1/2}} \tag{3.2}$$

where $P_i(\omega_k)$ contains the samples of the power spectral density $P_{ii}(e^{i\omega})$; and $P_{ij}[\omega_k]$ are samples of the cross-spectrum $P_{ij}(e^{i\omega_k})$ between y_i and y_j.

These quantities are evaluated by means of Welch's method with Hanning time windows of 1s and an overlap of 50% [206]. While C has an intuitive interpretation because it captures linear correlations in the frequency domain, IC, by neglecting zero-lag contributions, is more robust to spurious connectivity due to volume condition [131].

As evident from Fig. 3.1, spectral coherence is generally higher and it more sensitive to short-distance interactions than imaginary coherence [31].

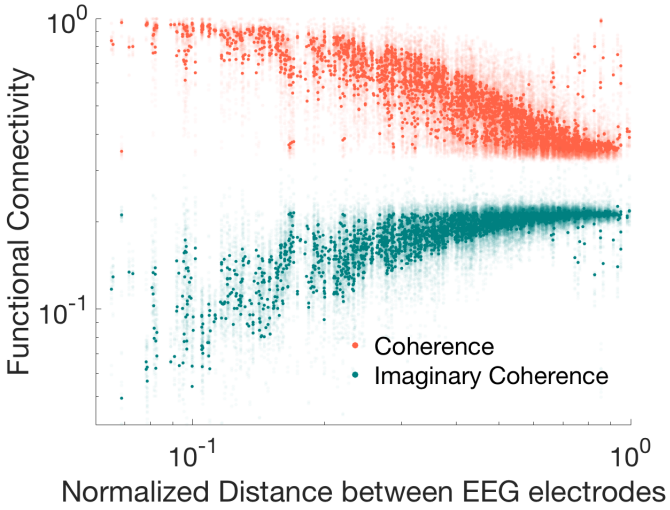

Figure 3.1: Connectivity estimators as a function of normalized distance between EEG electrodes. Coherence values are in orange while imaginary coherence results are in green. Connectivity estimated are extracted from all the available experimental observations in the β frequency band. [31] ©2018 IEEE

In order to measure the phase relationship between two signals at the frequency ω_k, we compute their phase difference Δ as follows:

$$\Delta_{ij}(\omega_k) = \left|\phi_i(\omega_k) - \phi_j(\omega_k)\right| \tag{3.3}$$

where $\phi_i(\omega_k)$, $\phi_j(\omega_k)$ are the phase terms of the discrete Fourier transforms (DFTs) computed from y_i and y_j.

After estimating C, IC and Δ for each pair of EEG channel, we obtain symmetric $N \times N$ matrices where $N = 74$ is the number of EEG electrodes. These matrices

correspond to fully connected and weighted graphs of N nodes or edges, possibly studied via graph theoretic tools [52]. In this thesis, we focus on an intuitive local centrality measure, i.e. the node strength S, which is computed as the sum of the weights of all links coming into each node. This metric describes in a simple and intuitive way how much one brain node, or EEG channel, is connected to all the others at a certain frequency ω_k. thereby, node strengths are derived for each connectivity estimator used to extract the network, as follows :

$$S_i^C(\omega_k) = \sum_{j=1}^{N} C_{ij}(\omega_k), \tag{3.4}$$

$$S_i^{IC}(\omega_k) = \sum_{j=1}^{N} IC_{ij}(\omega_k), \tag{3.5}$$

$$S_i^{\Delta}(\omega_k) = \sum_{j=1}^{N} \Delta_{ij}(\omega_k) \tag{3.6}$$

3.2.3 Statistical Analysis and Classification

At group level, we average for each subject the associated connectivity matrices across trials and within frequency bands, namely: $theta(\theta) = 4 - 7\text{Hz}$, $alpha(\alpha) = 8 - 13\text{Hz}$, $beta(\beta) = 14 - 29\text{Hz}$ and $gamma(\gamma) = 30 - 40\text{Hz}$. Node strength features are computed from each of these resulting networks. The same procedure is performed for power spectrum-based features.

We statistically compared connectivity and node strength values between the two mental states of MI and resting conditions. More specifically, for each condition we consider the distributions of the connectivity-based features obtained from the entire population of 20 subjects. We used non parametric permutation statistical tests (2000 permutations) with a statistical threshold of 0.05 [215] corrected for multiple comparisons with false discovery rate [19]. .

At individual level, we did not average the features across trials or within frequency bands. We let the classification procedure automatically select the set of best discriminant features for MI and resting for each subject. We only impose some constraints to limit the research complexity. First, we consider frequency bins from 4 to 40 Hz, because state-of-the-art results prove their involvement in similar motor tasks [128]. Second, we limit the research among a subset of electrodes spatially covering the sensorimotor areas [147].

In order to investigate the contribution of the three different types of features (S_C,S_{IC} and P) to the classification we considered all their possible combinations, i.e. seven in total. To normalize the values in each combination, we apply a z-

score transformation to original features, i.e. channels $\times$ frequency bins. Then, we perform a 100 repeated ten-fold cross-validation classification with linear discriminant analysis (LDA) [106, 107]. In addition, we perform a sequential feature selection procedure [58] within a nested cross-validation framework to automatically identify the best discriminant features for each subject.

3.3 Results

3.3.1 EEG network connectivity changes during motor imagery

In order to verify that subjects were actually performing a proper motor imagery task, we show sensorimotor power decreases in Fig. 3.2 mainly in frequency bins within *alpha* and, more pronouncedly, *beta* band ($p < 0.05$, FDR-corrected).

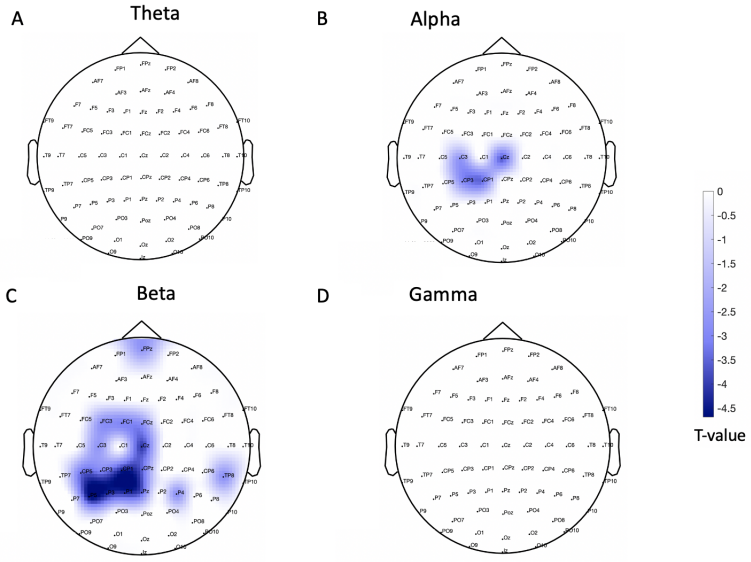

Figure 3.2: Statistical contrast maps between motor imagery and resting states obtained with band power features. Results are shown for one-tailed permutation-based t-tests ($p<0.01$). In Panel A) the obtained t-values are illustrated for individual representative frequency bins within the *theta* band, B) *alpha* band, C) *beta* band, and *gamma* band. In the *beta* band, results also remained significant after correction for multiple comparison ($p<0.05$, FDR corrected).

Network connectivity changes between MI and rest conditions are evident in all the frequency bands (Appendix B, Fig. 3.12, Fig. 3.13). Interestingly, in the *beta* band, results tend to occur in motor-related areas contralateral to the imagined movement. It is evident both for single connection and node strength values (Fig. 1A). These changes were even stronger when considering node strength values at

individual frequency bins ($p < 0.05$, FDR-corrected) (Fig. 3.3B).

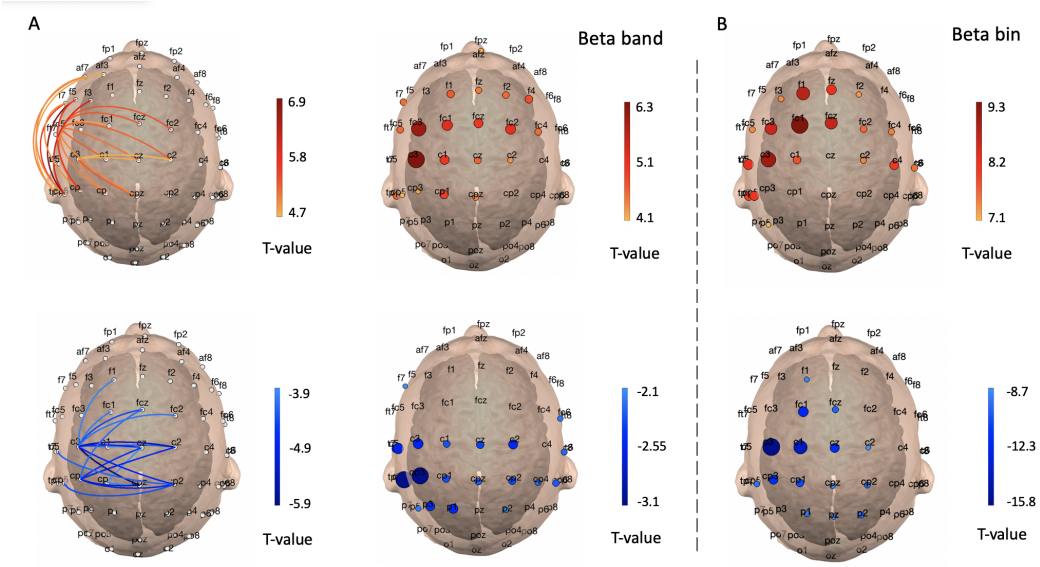

Figure 3.3: Statistical contrast maps between motor imagery and resting states in the *beta* band. In panel *A*, we report the results in *beta* band for connectivity and node strength values. In panel *B*, we show the results of node strength for individual representative frequency bins within the *beta* band. Results for coherence-based features are in top line, while those for imagery coherence-based features are in bottom line. Only the twenty most discriminant values are represented here for illustrative purposes.

Notably, the direction of the change is opposite depending on whether we estimate EEG networks with spectral-coherence (C) or with imaginary-coherence (IC). From our results, we report significant MI-related increases when we consider C estimators, while we observe significant decreases when using IC. In terms of spatial locations these differences involve both intra-hemispheric and inter-hemispheric interactions, while the largest changes in node strength tend to concentrate around the brain areas corresponding to the EEG electrode $C3$.

We observe a similar behaviour for *gamma* frequency band, although the most involved regions are more heterogeneously distributed. On the contrary, we cannot recognize similar trends for *theta* and *alpha* bands, where connectivity changes are in the same direction (Appendix B, Fig. 3.12 ,3.13).

We remark that the intensity of network changes is generally larger compared to power spectral P features (Fig. 3.3B, 3.2). For sake of clarity, we preliminary verified that results obtained with node strength are not correlated with those obtained by using P values (Pearson's correlation < 0.1).

These results indicate that the motor imagery of the hand grasping produces significant brain network changes that might be useful to characterize MI-based

BCI tasks. These changes uncover the existence of two parallel connectivity behaviours (i.e. increase for C and decrease for IC) that primarily involved sensorimotor areas within *beta* frequencies.

Real part of coherence In order to completely investigate the behaviour of the different contributions of coherence [45], we also study the real part of coherence [141], defined as follows:

$$RC_{ij}[\omega_k] = \frac{\left|\Re\left(P_{ij}(\omega_k)\right)\right|}{\left(P_i(\omega_k) \cdot P_j(\omega_k)\right)^{1/2}} \tag{3.7}$$

Node strengths are derived for when the real part of coherence is the connectivity estimator used to extract the network, as follows:

$$S_i^{RC}(\omega_k) = \sum_{j=1}^{N} RC_{ij}(\omega_k) \tag{3.8}$$

We perform the statistical analysis among the twenty subjects previously described with connectivity features and node strength. At both single connection and node strength level, we find a global significant increase which is actually similar, in terms of magnitude and spatial localisation, to what observed with C (Fig. 3.6A,B). This improvement is evident both for single connection and node strength values (Fig. 3.4).

Our results demonstrate that the effect at zero-lag, which are measured by the real part of coherence while completely neglected by the imagery coherence, strongly influence the spectral coherence estimation. This behaviour is demonstrated by the similar results obtained from statistical tests based on spectral coherence and the real part of coherence.

3.3.2 Modulation of amplitude and phase synchronization between brain signals

To deepen the nature of such dichotomy, we investigated more in detail the behaviour of C and IC estimators. C is computed from the cross-spectrum of the two signals and it is sensitive to the signals' amplitude synchronization, i.e. when signals oscillate (or vary) at the same frequency. IC is also sensitive to the phase synchronization measuring possible time shifts between the signals.

To study these behaviours, we consider an example of two equal sine waves oscillating at $10Hz$, but shifted one with respect to the other within the $[-\pi/2, \pi/2]$ interval. Fig. 3.5 shows that while C value is constant along the entire phase shift range, IC varies in a way that it tends to zero when the two signals are

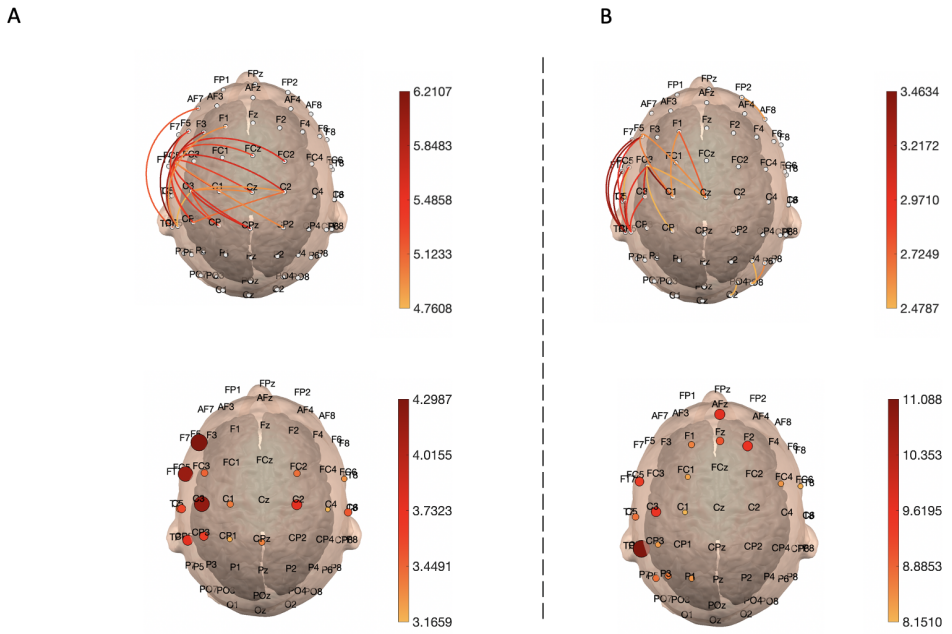

Figure 3.4: Statistical contrast maps between motor imagery and resting states in the *beta* band. In panel *A*, we report the results in *beta* band for connectivity and node strength values. In panel *B*, we show the results of node strength for individual representative frequency bins within the *beta* band.

perfectly in phase (i.e. $\Delta = 0$).We report in Appendix C an additional analysis to demonstrate that imaginary coherence between those signals can be analytically written as a function of their relative time delay.

Our experimental results in terms of statistical tests show the presence of a twofold brain mechanism happening during MI, characterized by: i) amplitude synchronization (captured by *C*) and ii) phase-synchronization (captured by *IC*), suggesting a significant signal phase alignment. To confirm this finding, we re-compute the task-related brain networks by means of the phase difference Δ between the EEG signals. At both single connection and node strength level, we find a global significant decrease which is actually similar, in terms of magnitude and spatial localisation, to what observed with *IC* (Fig. 3.3A,B).

To deepen the interpretation of FC changes, we focus on the MI task-related relationship between imaginary coherence and relative phase difference. For each subject, we consider all the FC links including the *C*3 electrode, representing the controlateral primary motor area of the right hand. Results show a moderate correlation (group-median Spearman's $R = 0.38$) with lower Δ values predicting lower *IC* values (Fig. 3.6, Table 3.2).

Taken together, our findings highlight a twofold mechanism which occurs dur-

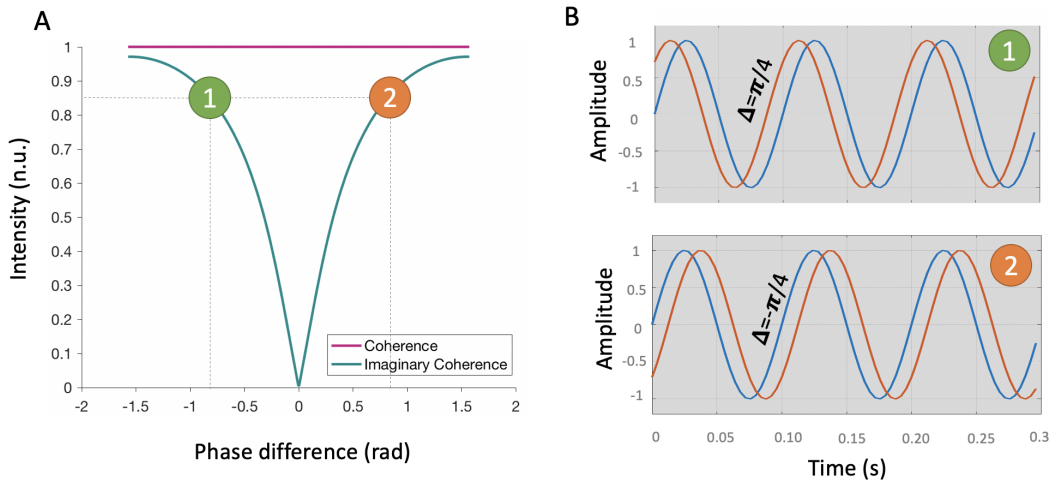

Figure 3.5: Relationships of coherence/imaginary coherence with phase difference. In Panel A) coherence is in pink and imaginary coherence in green, showing the functional connectivity between two sine waves at 10 Hz as function of their temporal shift. The shift, corresponding here to a phase difference, varies from 0 to π in steps of π /500. At each shift value, the two connectivity estimators are evaluated. Panel B) shows the sine waves with different phase differences. In panel 1), a positive Δ of π /4 in panel 2), a negative Δ of $-\pi/4$.

	Subjects																			
	1	2	3	4	5	6	7	8	9	10	11	12	13	14	15	16	17	18	19	20
Correlation (IC,Δ)	0,49	0,19	0,46	0,54	0,43	0,35	0,46	0,14	0,40	0,28	0,55	0,22	0,58	0,46	0,37	0,23	0,58	0,15	0,34	0,20

Table 3.2: Spearman correlation coefficient between IC and Δ for links including C3 for each subject.

ing MI tasks. It consists in a simultaneous amplitude and phase synchronization among sensorimotor brain regions.

3.3.3 Mental state detection in single individuals

Finally, we test the ability of these brain connectivity features to discriminate MI and resting states at single subject level. To increase specificity, we consider a finer frequency resolution of 1 Hz - from 4 to 40 Hz - and we reduce the features to the EEG electrodes in the sensorimotor areas.

For each subject and each condition (i.e. MI and rest) we extract three type of features: power spectrum P, coherence-based node strength S^C and imaginary coherence-based node strength S^{IC}. We perform an automatic sequential forward

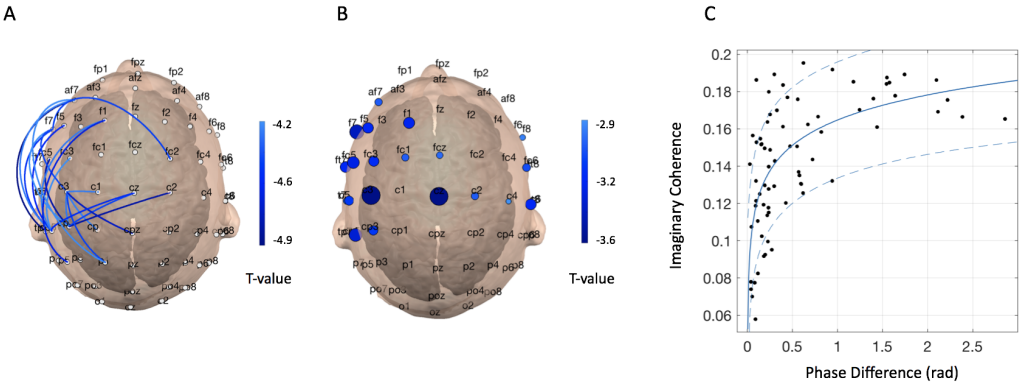

Figure 3.6: Phase difference properties and discrimination ability. Panel A), results of permutation-based t-tests in the *beta* band across all subjects are shown for brain networks reconstructed from the phase difference between EEG signals. Panel B) results of permutation-based t-tests obtained with node strength values extracted from the previous brain networks. Panel C), Spearman correlation plot between imaginary coherence and phase difference values considering all the connections including C3 electrode for one representative subject.

feature selection within a cross-validation linear discriminant analysis (LDA). We consider the overall accuracy to quantify the average classification performance across cross-validation folds.

We report classification accuracies in Table 3.3. Results show that the best classification accuracy was in general moderate regardless of the feature combination.

After collecting accuracy values, for each subject we compute the relative difference between the accuracy obtained with the best feature combination and the accuracy referred to P features. Let us remark that we consider the relative difference equal to zero when the best feature combination is P. We report results in Fig. 3.16. Interestingly, we observe that the inclusion of node strength features leads to improve performances in terms of relative difference with respect to P features alone.

The improvement of classification performances when node strength features are included is particularly evident when features are selected from the controlateral hemisphere only (16 subjects over 20) as compared to when we consider both hemispheres (12/20). For features in controlateral areas, the performance improvement associated to the best features combination was 13% in average across subjects. To identify the spatial and spectral characteristics of the selected features, we show their cumulative occurrence in a frequency-sensor plot (Fig. 3.8). In general, we observe a concentration of features in the $10-14$ Hz range within the C-CP zone. For both P and S^C , the occurrences at higher frequencies tends

Subjects	1	2	3	4	5	6	7	8	9	10	11	12	13	14	15	16	17	18	19	20
Accuracy (CONTRA+IPSI)	**71,38**	**64,41**	**63,70**	**54,90**	**60,19**	**61,17**	**61,14**	**64,48**	**62,28**	**60,86**	**68,29**	**66,12**	**66,12**	**56,08**	**64,15**	**56,60**	**50,03**	**50,53**	**60,35**	**67,33**
Best feature combination (CONTRA+IPSI)	S^C + P	P + S^{IC}	S^C + P	P	P	S^C	S^C	P	S^{IC}	P	S^C	P	S^C + P	P	P	S^{IC}	S^{IC}	S^{IC}	S^C + S^{IC}	P
Accuracy (CONTRA)	**74,35**	**61,95**	**61,80**	**60,65**	**59,37**	**62,95**	**58,38**	**69,85**	**64,33**	**58,62**	**69,58**	**71,54**	**58,81**	**52,84**	**69,19**	**56,96**	**53,80**	**61,30**	**69,28**	**56,08**
Best feature combination (CONTRA)	S^C + P	S^C + S^{IC}+P	S^C + S^{IC}+P	P	S^C + S^{IC}+P	S^C + P	S^C + P	S^C + S^{IC}+P	P + S^{IC}	S^C + S^{IC}	P + S^{IC}	S^C + P	P	S^C + S^{IC}+P	S^C + P	S^C + S^{IC}+P	P	S^C + P	S^C + S^{IC}	P

Table 3.3: Average accuracy across cross-validation fold and repetitions is reported the best feature combination for each subject. In the top rows, we have classification results obtained when selected electrodes are located in both in contralateral and ipsilateral sensorimotor areas, ie. FC5, FC3, FC1, C5, C3, C1, CP5, CP3, CP1, FCZ, CZ, CPZ, FC2, FC4, FC6, C2, C4, C6, CP2, CP4, CP6. In the bottom rows, results come from classification framework including only controlateral electrodes, ie.FC5, FC3, FC1, C5, C3, C1, CP5, CP3, CP1.

to fade out (Fig. 3.8A,B), while the situation appears more heterogeneous for S^{IC} features (Fig. 3.8C).

For comparison's sake, we perform an alternative classification by substituting power spectrum features with those obtained with another state-of-the-art method, namely the filter bank common spatial pattern (FBCSP) [7], widely used in MI -based BCI applications. Results show that using FBCSP features does not significantly improve the overall accuracy and that node strength features still contribute to the relative performance improvement (Appendix D).

In order to measure the potential of connectivity-based features to characterize other motor imagery tasks, we used the EEG data from dataset 1 of BCI competition IV [20]. EEG data were recorded from 59 electrodes, which enabled us to obtain a number of nodes similar to our data. From this dataset we considered 4 healthy subjects each one performing different MI tasks (left hand/ foot for subject a; left hand/ right hand for subject b; left hand/ foot for subject f and left hand/ right hand for subject g). Results showed in Appendix E demonstrated that the inclusion of S^C features allowed to slightly increase classification accuracy in three over four subjects.

Taken together, these results show the potential of brain network features, de-

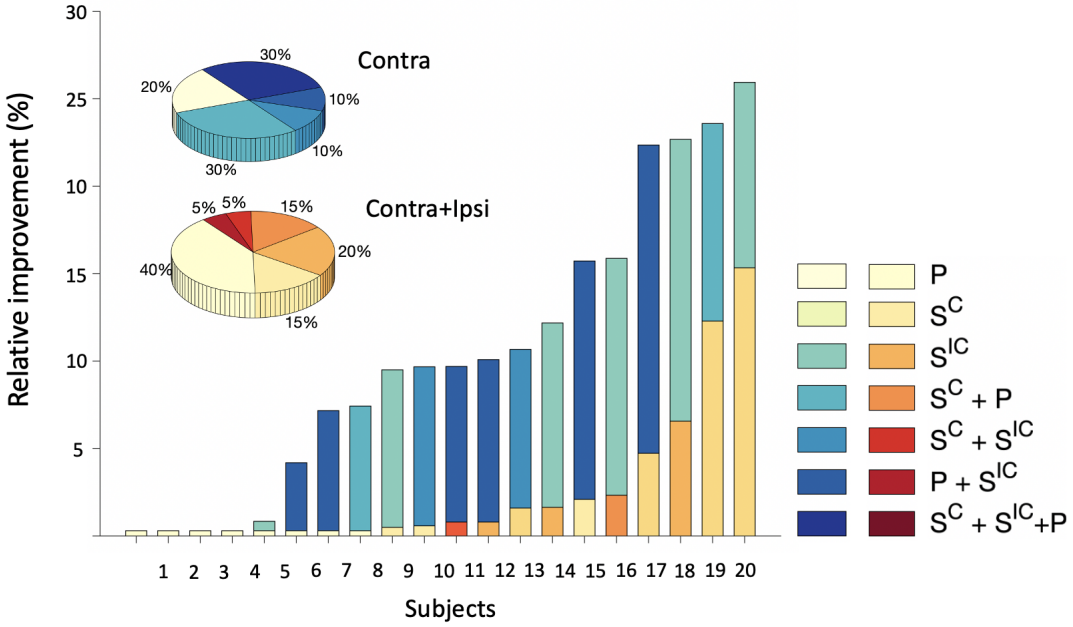

Figure 3.7: Improvement of classification performance. Bar plots show the percentage of relative increment between the best combination of features (i.e., coherence-based node strength S^C, imaginary coherence-based node strength S^{IC} and power spectrum P. The pie diagram in the inset illustrates the percentage of times that a specific combination of features has been selected across subjects.Two different cases are considered, distiguished by a different color code. In blue, we report results of accuracy improvements when selected electrodes are located in controlateral sensorimotor area (Contra), i.e. FC5, FC3, FC1, C5, C3, C1, CP5, CP3, CP1. In red, results relate to classification analysis when electrodes are in both contralateral and ipsilateral sensorimotor areas (Contra+Ipsi), ie. FC5, FC3, FC1, C5, C3, C1, CP5, CP3, CP1, FCZ, CZ, CPZ, FC2, FC4, FC6, C2, C4, C6, CP2, CP4, CP6

rived from both amplitude and phase synchronization, to play an important role in the characterization of motor imagery states in healthy subjects.

3.4 Discussion

Brain activity changes during motor tasks have been largely documented by means of invasive and non-invasive neuroimaging techniques in non-human and human primates, as well as in animal models [124, 148, 149]. These changes are not limited to specific brain areas, but also occur in a synchronized manner across larger spatial scales reflecting the need for coordination of information exchanges to perform the task [47, 55, 88, 117].

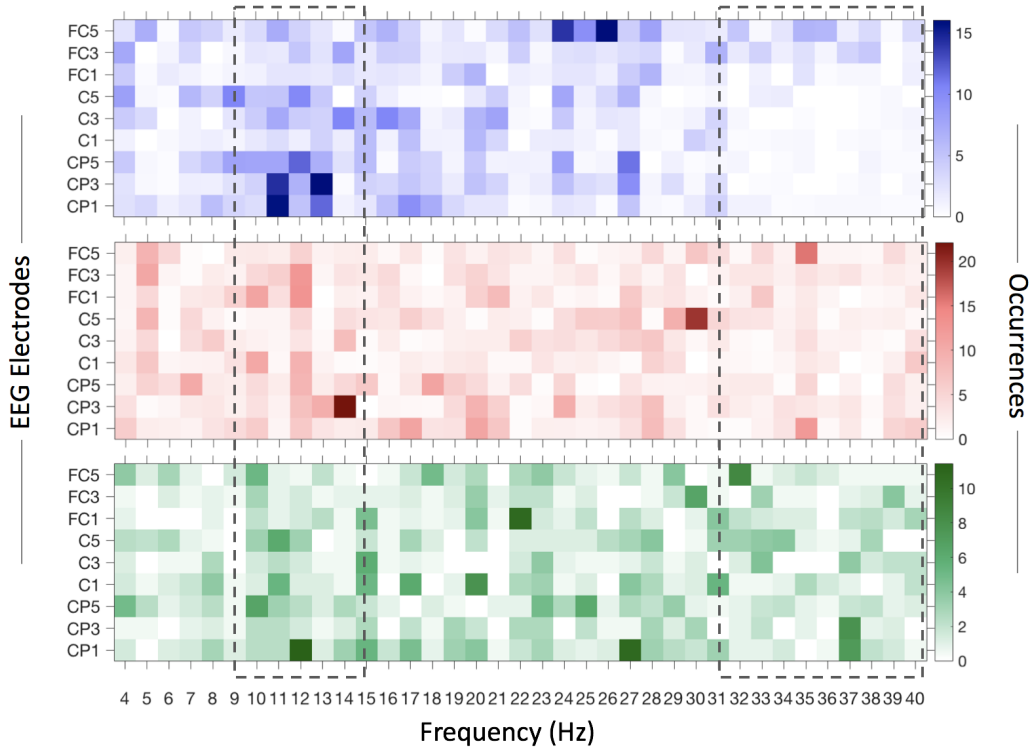

Figure 3.8: Brain features selected by the classification procedure. The color codes for the group-averaged number of times that a specific feature - in the electrode-frequency space - has been chosen during the sequential feature selection algorithm. The results for P features are illustrated in the top line, those for S^C in the middle line and those for S^{IC} in the bottom line. Results relates to the classification analysis framework when only electrodes in the contralateral sensorimotor areas are selected.

Functional connectivity methods, measuring dependences between spatially remote brain areas, represent a unique opportunity to investigate large-scale brain network changes during motor imagery tasks from EEG recordings. Previous works reported FC changes in both healthy and diseased subjects [51, 108], as well as in BCI contexts [72, 75, 77, 98, 150]. However, different FC estimators have been applied in those studies and a deeper interpretation of obtained FC mechanisms was in general overlooked. As a result, a common direction and key interpretation of the FC processes observed during BCI motor-related tasks is still lacking [98].

To deepen this aspect, we study the intrinsic nature of two popular FC estimators, spectral coherence and imaginary coherence, extracted during motor imagery tasks in a group of healthy subjects. Our results indicate that motor imagery elicits two major parallel oscillatory phenomena in the *beta* frequency band: *i)* the increase of synchronization between the EEG signals' amplitudes, *ii)* a decrease

of phase difference, which means an increase of synchronization between signals' phases. Both amplitude and phase synchronization increases have been respectively reported in previous studies. The former typically codes for a basic substrate of neural communication [197], while the latter favours a further information binding [127]. These FC modulations were region-specific and more localized in the sensorimotor areas. They particularly emerge at the node strength level and are not correlated with other regional measures, such as standard power spectral densities. We observe the presence of complementary mechanisms of amplitude and phase synchronization in the higher frequency bands (i.e. *beta* and *gamma*), but not in *theta* and *alpha* bands. While this is in line with previous results reporting high-frequency FC changes in motor imagery-based BCI, the role the lowest frequency bands needs to be further explored [72]. Future research should assess whether these network changes only reflect direct motor-related response or, also include indirect effects due to mirror-neuron activity as well as attentional efforts associated to the task complexity [124].

The ability to detect cognitive states from non-invasive neuroimaging recordings has concrete consequences in our daily-life, from the early detection of brain diseases to the design of brain-computer interface systems [122]. In the BCI context, much of the efforts has focused on the improvement of the classification algorithms, such as the recent developments in Riemannian geometry-based approaches [13, 65]. Although these methods improve the overall classification performances, they generally lack of physical and physiological interpretations [50, 106, 107]. Looking for alternative features, beyond the characterization of regional responses, is therefore a fruitful research field. [26, 48, 76, 98, 100, 205].

Whether the use FC and network-based features enable to significantly improve BCI classification improvements, is still under debate [28, 48, 70, 75, 98, 205]. Our results demonstrate that FC-based features bring complementary information with respect to power spectrum and have the potential to improve cognitive states' identification. This might have implications in the design of future BCIs, where the features selection is typically performed in the training phase. However, we remark the performance improvements measured here significantly vary across individuals and overall accuracies are generally moderated. Although our contribution highlights the potential of brain network features to address BCI inefficiency problem [191, 199], further studies are crucial to assess the actual ability to discriminate between multiple mental states [165].

3.4.1 Methodological considerations

The estimation of spectral- and imaginary coherence assumes the stationarity of time series within the time window of computation. [131]. In our study, we considered time windows lasting 5 s, which could be too long the stationarity hypothesis [94]. More in general, for real-time BCI applications the use of shorter time windows and FC estimators not requiring stationarity assumptions (e.g. wavelets [102], tracking algorithms [137]), would naturally allow to circumvent this issue.

We perform the study of FC networks on the EEG sensor space. Coherence-based FC estimates are affected by volume conduction distortions which cause spurious signal interactions [131, 140]. Although source-reconstruction techniques can be used to mitigate such effect [85], we choose to work on the sensor space for two main reasons. The first motivation is a practical one. Indeed, we do not have access to the individual magnetic resonance images (MRIs) needed to have a realistic model of the head and its structures [10, 56, 119]. The second motivation is more methodological because FC estimators can be really sensitive to signal transformations and results can strongly depend to the selected reconstruction algorithm [110]. A detailed study on the effects of source-reconstruction is beyond the scope of our analysis. Future research is necessary to better investigate the stability of our results at source space level.

In order to combine intrinsically different estimators of brain activity (i.e. power, node strengths), we perform a fusion at the feature level [164]. An alternative possibility is to perform the fusion at the classifier level, by combining the posterior probabilities of each separate classification [46]. The disadvantage of the latter approach is that it forces the research of significant features in each modality despite their absolute discriminant power. We prefer let the classifier to automatically select the best absolute combination of features.

3.5 Conclusions

Consistent with our hypothesis, we demonstrate the contribution of brain network connectivity features to detect cognitive states during typical MI-based BCI tasks. More importantly, we find that hand MI is characterized by a twofold connectivity mechanisms, consisting in a simultaneous amplitude and phase synchronization of large-scale brain activity. Taken together, our results provide new insight into the network behaviours sub-serving brain functional changes during MI, and open new perspectives to improve BCI systems.

Appendix A: Example of Preprocessing

Here, we show an example of the preprocessing procedure on one subject. In Fig. 3.9, we report the first 60s recorded for EEG signals. EEG channels are ordered from frontal to parietal, and we recognize blink effects in the data recorded from the first channels as regular spikes.

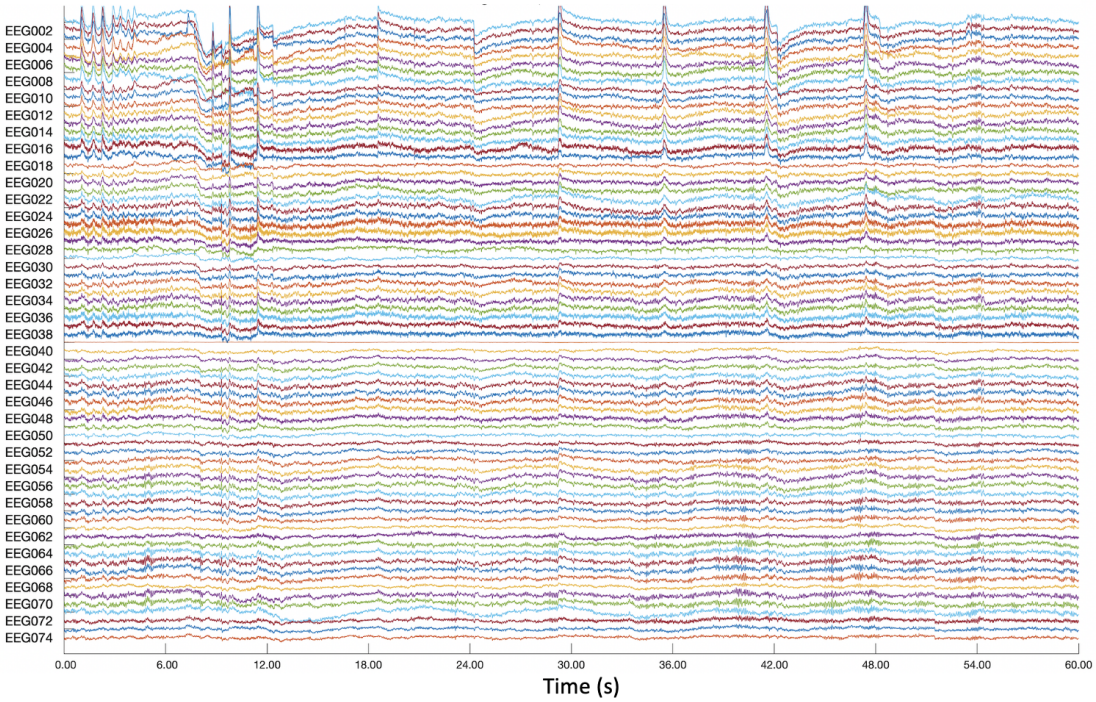

Figure 3.9: EEG signals before the preprocessing for one subjects. We show the first 60s of recordings.

Then, we perform an independent component analysis (ICA) using the Infomax algorithm to preprocess original signals. We visualize in Fig. **??** the first 10 ICs. The first independent component appears located on the frontal electrodes and the signal as blinks' characteristic spikes. For these reasons, we decide to eliminate the first ICA, and we eventually reconstruct EEG signals for each and every EEG channels.

We report in Fig. 3.11 EEG signals after ICA. Comparing EEG data with those in Fig. 3.9, we remark the significant decrease of high and regular spikes in the first components, caused by the elimination of the blink component.

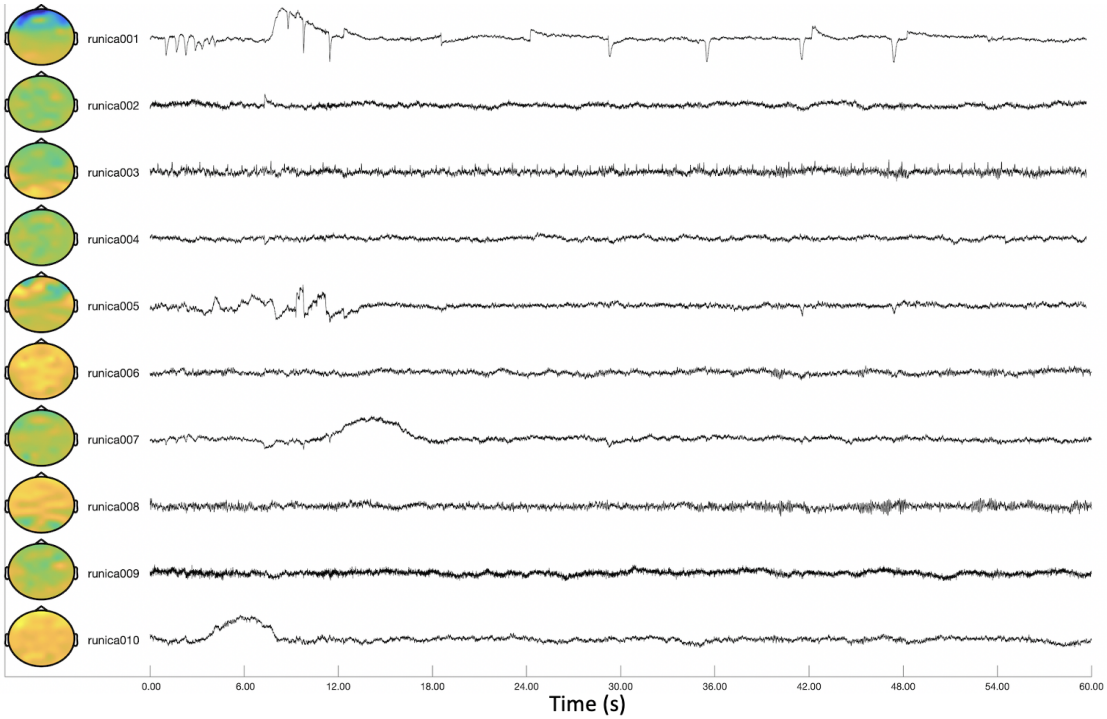

Figure 3.10: Independent component obtain with Infomax algorithm. We show the first 10 ICs and the first 60s of recording. For each component, both the signals and the associated topography are represented to facilitate the preprocessing procedure.

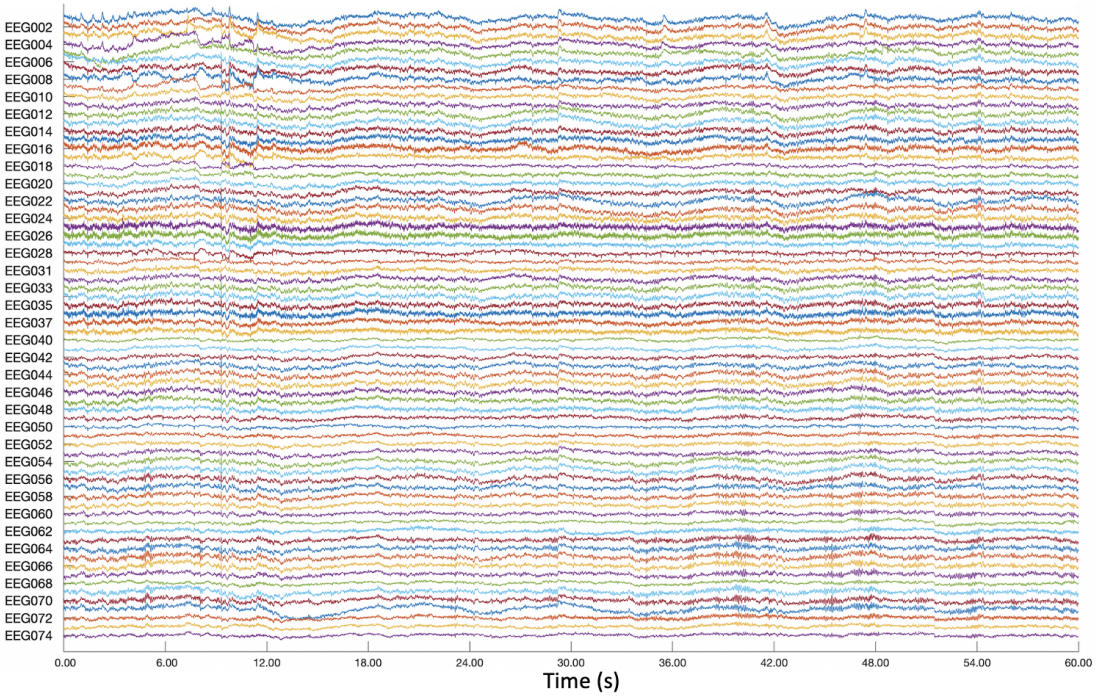

Figure 3.11: EEG signals after preprocessing for one subjects. We show the first 60s of recording.

Appendix B: Brain connectivity changes during MI tasks in all frequency bands

We report the results of permutation t-test in all the frequency bands of interest, i.e. *theta*, *alpha*, *beta* and *gamma*, in order to compare brain mechanisms in all the frequencies. We consider the case of connectivity changes in Fig. 3.12 while node strength behaviours are in Fig. 3.13

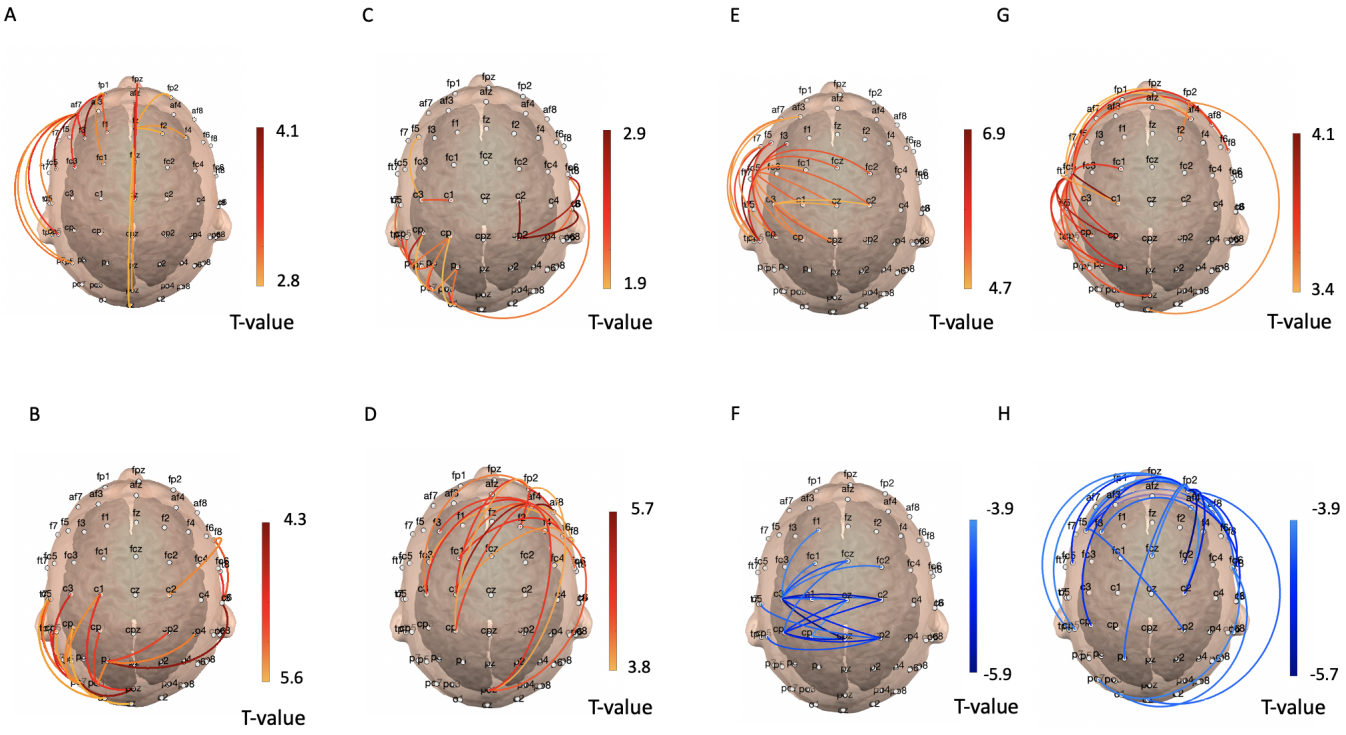

Figure 3.12: Statistical contrast maps between motor imagery and resting states for connectivity features. In top line, we have results for coherence features and in the bottom line for imaginary coherence ones. In Panel A) results for coherence in *theta* band, in B) for imaginary coherence in *theta* band, in C) for coherence in *alpha* band, in D) for imaginary coherence in *alpha* band, in E) for coherence in *beta* band and in F) for imaginary coherence in *beta* band in G) for coherence in *gamma* band and in H) for imaginary coherence in *gamma* band . Only the twenty most discriminant connections are represented here for the sake of simplicity.

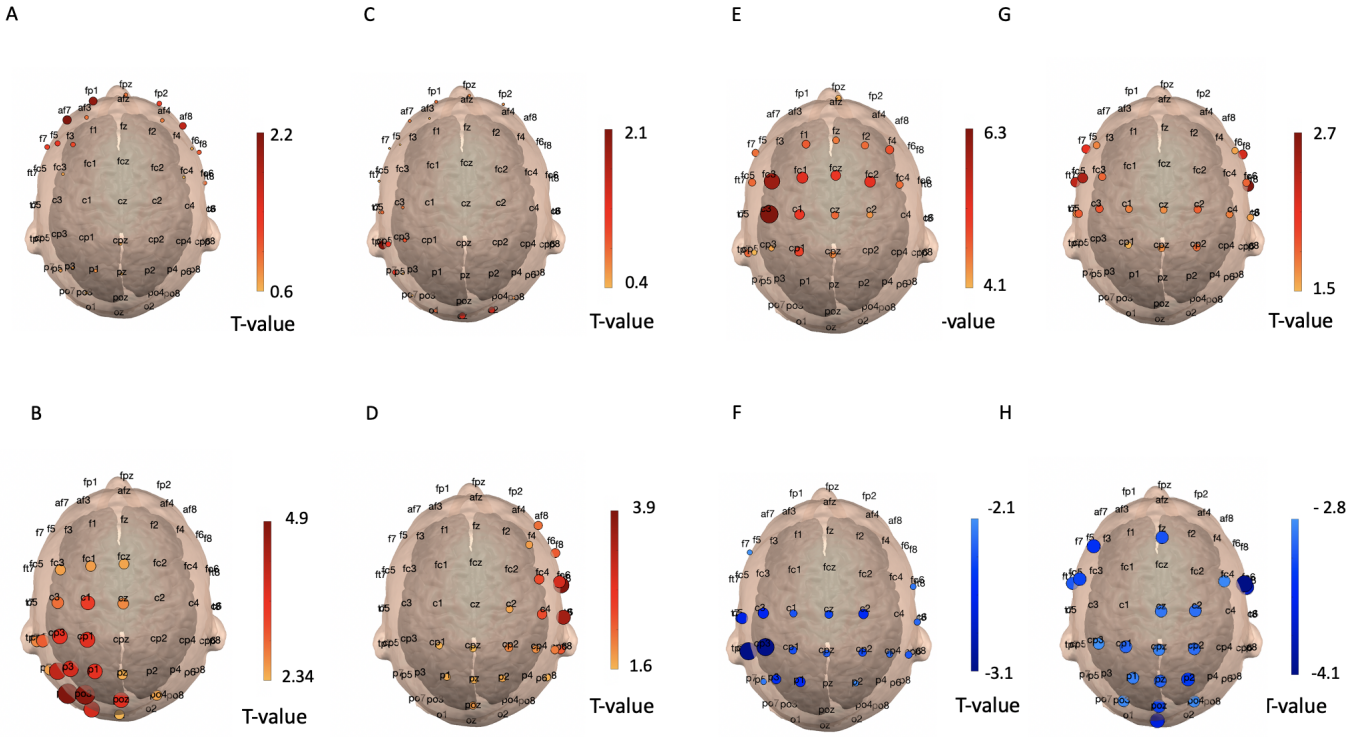

Figure 3.13: Statistical contrast maps between motor imagery and resting states for node strength features. In top line, we have results for coherence-based node strength features and in the bottom line for imaginary coherence ones. In Panel A) results for coherence in *theta* band, in B) for imaginary coherence in *theta* band, in C) for coherence in *alpha* band, in D) for imaginary coherence in *alpha* band, in E) for coherence in *beta* band and in F) for imaginary coherence in *beta* band in G) for coherence in *gamma* band and in H) for imaginary coherence in *gamma* band . Only the twenty most discriminant connections are represented here for the sake of simplicity.

Appendix C: Coherence and imaginary coherence estimation for sine waves

Let y_i and y_j be two signals of length T such that they only differ of a time shift t_0. In this simple situation, their cross-spectrum in the continuous domain reads as

$$P_{ij}(e^{i\omega}) = P_j(e^{i\omega})e^{i\omega t_0} \tag{3.9}$$

where ω is the angular frequency of a signal [206]. In the discrete domain, this can be rewritten as

$$P_{ij}(\omega_k) = P_j(\omega_k)e^{i2\pi\omega_k t_0/T} \tag{3.10}$$

where the time shift t_0 becomes a linear phase term.

In the mathematical formulation of coherence C

$$C_{ij}(\omega_k) = \frac{\left|P_{ij}(\omega_k)\right|}{\left(P_j(\omega_k) \cdot P_k(\omega_k)\right)^{1/2}} \tag{3.11}$$

the numerator is the real part of the cross-spectrum and the exponential term in Eq. 2 is cancelled out. This indicates that C values do not depend on the amount of time shift between the signals.

Instead, in imaginary coherence IC,

$$IC_{ij}(\omega_k) = \frac{\left|\Im\left(P_{ij}(\omega_k)\right)\right|}{\left(P_i(\omega_k) \cdot P_j(\omega_k)\right)^{1/2}} \tag{3.12}$$

it is trivial to show that there is a remaining term related to t_0 in the numerator. Indeed, by rewriting the cross-spectrum via trigonometric functions:

$$P_{ij}(\omega_k) = P_j(\omega_k)(\cos\left(2\pi\omega_k t_0/T\right) + i\sin\left(2\pi\omega_k t_0/T\right)) \tag{3.13}$$

Hence, by taking the imaginary part one obtains

$$\Im(P_{ij}(\omega_k)) = P_j(\omega_k)\sin\left(2\pi\omega_k t_0/T\right) \tag{3.14}$$

This indicates that IC values do depend on the relative delay between the signals in a very specific way. More in general, in it has been emphasized that the estimated imaginary coherency between two time series can be expressed as a function of the instantaneous phase difference of their analytic signals[184].

Appendix D: Alternative state-of-the-art classification based on FBCSP

In order to compare network-based feature with another state-of-the-art method, we perform a shrinkage LDA classification with FBCSP (filter bank common spatial pattern) features [7], alone and in combination with network features (S^C and S^{IC}). For the FBCSP computation, we firstly band-pass signals with Chebyshev Type II filters and we obtain 9 intervals of 4 Hz each: 4-8,...36-40. After, for each band-passed signals, we compute CSP algorithm as graphically presented in Fig. 3.14. In order to allow a fair comparison, connectivity-based features are extracted for 4 to 40 Hz in steps of 4 HZ.

This computation is then added to our classification framework: feature selection and then 100 repeated 10-fold LDA classification. A different approach is used in this scenario for the fusion. In fact, in the previous classification the fusion between P, S^C and S^{IC} was a feature fusion, while here we perform a fusion of classifiers given the heterogeneity of the features (Fig. 3.15). More specifically, to integrate different features we used a Bayesian approach similar to what done in a previous work [46]: posterior probabilities of each feature (p_f) are linearly combined to derive the parameters:

$$\mu_f = \frac{p_f}{p_{CSP} + p_{s^C} + p_{s^{IC}}} \tag{3.15}$$

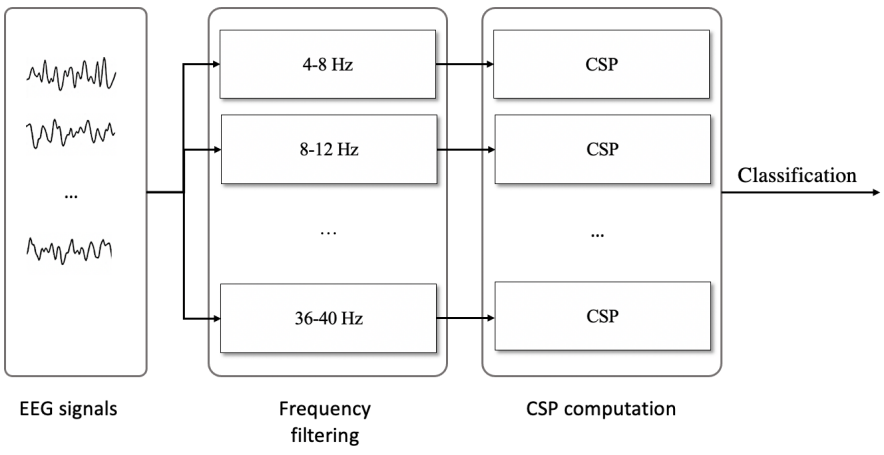

Figure 3.14: FBCSP procedure. EEG signals recorded from N channels are band-passed in frequency intervals. Then, for each frequency interval, the common spatial pattern is computed. Finally, the posterior probability is estimated in order to weight CSP features to perform a classification fusion to integrate different type of features.

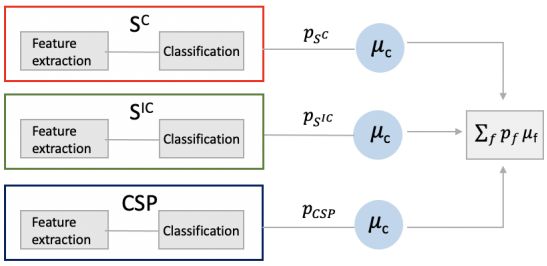

Figure 3.15: Scheme of the fusion procedure. Each type of feature is computed and used to train a classifier. Then, the posterior probability is computed in each case and a Bayesian approach is used to integrate the different features.

The parameter μ_f corresponds to a weight for each type of feature f. We observe from accuracy results that the classification with CSP did not perform better than classification with P, in our specific application.

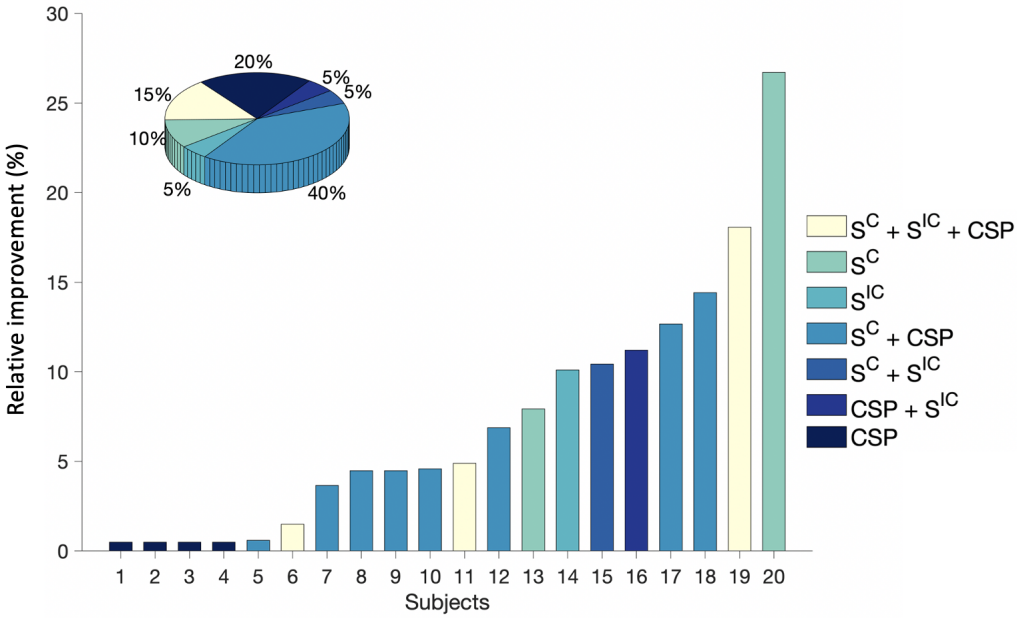

Figure 3.16: Improvement of classification performance. Bar plots show the percentage of relative increment between the best combination of features (i.e., coherence-based node strength S^C, imaginary coherence-based node strength S^{IC} and common spatial pattern CSP. The pie diagram in the inset illustrates the percentage of times that a specific combination of features has been selected across subjects.

Subjects

	1	2	3	4	5	6	7	8	9	10	11	12	13	14	15	16	17	18	19	20
Accuracy	**73,05**	**57,95**	**62,53**	**60,91**	**56,09**	**56,63**	**67,3**	**60,61**	**67,75**	**57,98**	**68,29**	**65,13**	**63,62**	**54,53**	**51,24**	**56,36**	**56,00**	**50,53**	**67,69**	**60,97**
Best feature combination	S^c + CSP	$S^c + S^{ic}$	$S^c + S^{ic}$ + CSP	S^c + CSP	CSP	S^c	S^c + CSP	S^c + CSP	S^c + CSP	CSP	$S^c + S^{ic}$ + CSP	S^c + CSP	S^c + CSP	CSP	CSP	CSP + S^{ic}	CSP + S^{ic}	S^c + CSP	S^c	$S^c + S^{ic}$ + CSP

Table 3.4: Average accuracy across cross-validation is reported for each subject and each combination of feature when CSP is used.

Appendix E: Classification analysis on BCI competition IV dataset 1

In order to measure the ability of connectivity features to characterize other motor imagery tasks, we also used the EEG data from dataset 1 of BCI competition IV [20]. EEG data were recorded from 59 electrodes, which enabled us to obtain a number of nodes similar to our data. From this dataset we considered 4 healthy subjects each one performing different MI tasks (left hand/ foot for subject a; left hand/ right hand for subject b; left hand/ foot for subject f and left hand/ right hand for subject g). To ensure consistency, we performed the very same analysis described in the Materials and methods of the main text. The obtained results confirmed that the inclusion of connectivity features (coherence-related ones) helps the classification accuracy in 3 over 4 subjects (Figure 3.17). In Figure 3.18 we present the location in terms of space and frequency of selected features. In blue, PSD features, in red coherence-based features and in green imaginary coherence-based features are reported. The intensity of the colors represents the occurrences of each feature.

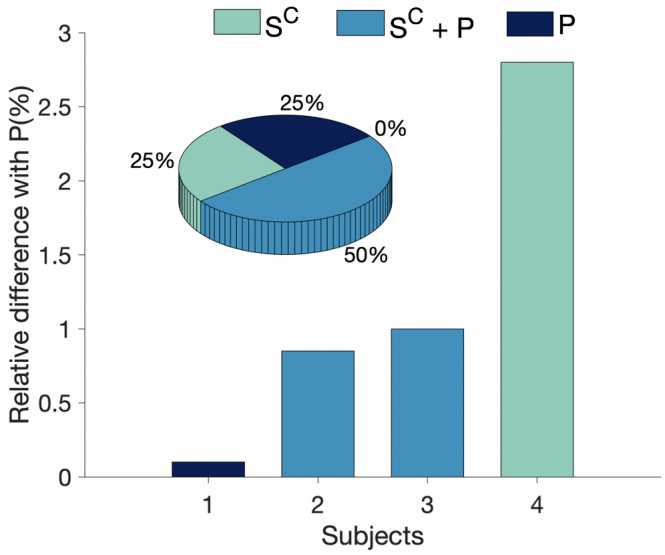

Figure 3.17: Improvement of classification performance. Bar plots show the percentage of relative increment between the best combination of features (i.e., coherence-based node strength S^C, imaginary coherence-based node strength S^{IC} and power spectrum P. The pie diagram in the inset illustrates the percentage of times that a specific combination of features has been selected across subjects.

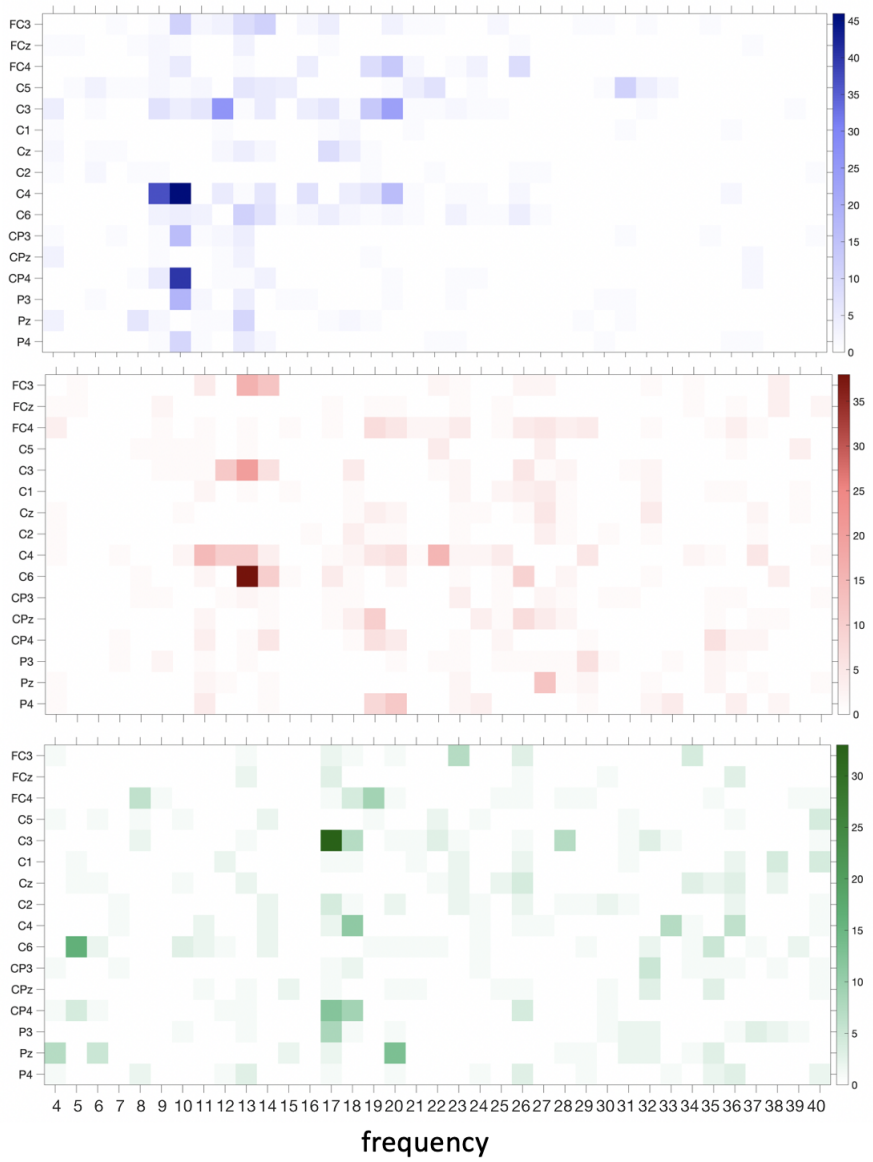

Figure 3.18: Brain features selected by the classification procedure. The color codes for the group-averaged number of times that a specific feature - in the electrode-frequency space - has been chosen during the sequential feature selection algorithm. The results for P features are illustrated in the top line, those for S^C in the middle line and those for S^{IC} in the bottom line. Results relates to the classification analysis framework when only electrodes in the contralateral sensorimotor areas are selected.

Chapter 4

Improving graph connectivity estimation with graph signal processing

Functional connectivity (FC) can be adopted to uncover brain (re)organization processes and it is applied to detect cognitive tasks, such as motor imagery (MI). The detection performances are strongly affected by the errors in FC estimation. In this chapter, we address the problem of robust graph FC estimation to improve the separability of cognitive states. Specifically, we propose a denoising algorithm based on graph signal processing (GSP) tools which acts on graph Laplacian. In order to quantify the separation between different states, we derive a novel formulation of the Jensen divergence. We firstly apply the denoising procedure to synthetic data, demonstrating its potential in the improvement of the Jensen divergence between two simulated conditions. Then, we perform analyses with real EEG data recorded during motor imagery-based BCI experiments. The novel formulation of the J-divergence enables to simultaneously quantify the distance between FC networks in motor imagery and resting, as well as to highlight the contribution of each Laplacian variable to total J-divergence. Experimental results on real data demonstrate the potential of the denoising algorithm on short time-windows. This approach provides new practical tools to robustly estimate FC networks and it opens new possibilities in the implementation of real-time BCI systems.

In this chapter are reported figures and part of the text from a recently submitted paper: Cattai, T., Scarano, G., Corsi, M. C., Bassett, D. S., De Vico Fallani, F., & Colonnese, S. (2020). Improving J-divergence of brain connectivity states by graph Laplacian denoising. arXiv preprint arXiv:2012.11240. [34]

4.1 Introduction

Functional connectivity (FC) describes the interactions between brain areas[16]. It can be modelled as a graph, which represent one possible formalism to represent networked systems [129, 192]. It has been recently demonstrated that graph statistics, such as node strength, efficiency and modularity [69]. The detection of brain FC-based features can boost several applications, such as brain-computer interfaces (BCIs). BCIs are communication systems enabling a subject to interact with external work without neuro-muscular activity [207, 210]. A critical requirement for BCI to work is the correct detection of the user's intent. Although the research significantly advanced on BCIs, there is still a limitation, commonly known as BCI inefficiency [191]. It indicates the fact that there is a non-neglecting percentage of users who cannot be trained to use the interface and cannot correctly use it. This limitation motivated us to propose novel techniques to increase the detectability of the user's cognitive states. Our intent is to develop original tools to have a more robust brain FC features to better separate two cognitive states. The practical implementation of FC estimation from signals acquired at graph vertices (e.g. EEG electrodes) is a not an easy task because of the noise, the high number of edges, artefacts (e.g. ocular, cardiac) and non-stationarity of brain signals.

In order to address the problem of robust connectivity estimation together with the improvement of separability between mental states for BCI control, the combination of tools from different fields is fundamental. For instance graph signal processing is suitable for this scenario[135, 167, 178]. It has already been applied in context of biological data, and specifically with brain data [81, 115]. GSP has the potential to simultaneously integrate properties of the brain structure, represented by the graph itself, and brain functioning, represented by signals on graph.

Other fundamental tools to deal with the functional connectivity estimation problem come from signal detection theory. Detection techniques can be applied to measure statistical differences between FC features associated to two brain states, corresponding to motor imagery and resting state in our application. There are several measures that can be adopted in this context, such as the Likelihood Ratio (LR) of the features [99, 146, 154, 169, 170, 174, 190, 193] and the linear detector which maximizes the so-called *deflection* [41, 151–153].

Obtaining a measure of the distance between two states is simplified under the assumption of normally distributed observations. Indeed, the maximum deflection test coincides with the LR test for normally distributed observations with equal conditional variance and different conditional means. Under this hypoth-

esis, LR test can be extended to a linear quadratic detector so as to deal with observations with different conditional variances [151, 153]. To evaluate a measure of separability between features under the two conditions, the Jensen divergence can be explored, corresponding the maximum deflection test performance [146, 169, 174].

In this chapter we propose a novel graph Laplacian denoising algorithm, able to improve the brain connectivity estimates. We propose a subspace-based Laplacian denoising which simultaneously preserves graph connectivity structure and rejects noise components. This algorithm preserves i) the subspaces more directly associated to the graph topology, summarized by the eigenvectors corresponding to the smallest Laplacian eigenvalues, ii) the subspaces associated to favourable signal-to-noise ratio, summarized by the eigenvectors corresponding to the largest Laplacian eigenvalues. We demonstrate that this twofold approach enhances the separability between two states.

In order to quantify the separability between two conditions and to measure the improvement achieved by the Laplacian denoising in the FC estimates, we present an original formulation of the Jensen divergence. The improvement of the J-divergence of the graph Laplacian coefficients under different states is proved by numerical simulations on synthetic data.

Finally, we test our method on real EEG data recorded during motor imagery-based BCI experiments, and we prove that our denoising algorithm increases the J-divergence evaluated between motor imagery and resting states, even when graph Laplacians are computed from short time-windows. As result of the J-divergence analysis, we attribute a score to each Laplacian coefficient representing its marginal contribution to the total J-divergence. The score admits a relevant biological interpretation confirming the efficacy of the approach. These results can be assessed by further studies on the brain connectivity features.

To facilitate the reader, we list in Table 4.1 the main notation used in the chapter.

4.2 Related Work

The problem of graph connectivity estimation has been widely explored in literature in several fields, from neuroscience to signal processing and graph theory [22, 27, 175]. Many state-of-the-art graph learning approach present over-simplified models to signals defined over graphs to overcome computational and memory issues. Some recent works propose different methods to address graph learning problems. For example, in [66] authors propose a new technique to ef-

Notation	Description
$\mathbf{A}$,$\hat{\mathbf{A}}$	adjacency matrix (real, estimated)
V	set of all nodes
N	total number of nodes
E	set of all links
$\mathbf{D}$, $\hat{\mathbf{D}}$	degree matrix (real, estimated)
$\mathbf{L}$, $\hat{\mathbf{L}}$	Laplacian matrix (real, estimated)
λ, $\hat{\lambda}$	eigenvalue (real, estimated)
$\mathbf{u}$, $\hat{\mathbf{u}}$	eigenvector (real, estimated)
$\mathcal{U}_{\mathcal{L}}, \mathcal{U}_{\mathcal{M}}, \mathcal{U}_{\mathcal{H}}$	subset of smallest, central, larger eigenvalues
$\tilde{\mathbf{L}}$, $\tilde{\mathbf{I}}$	filtered graph laplacian matrix and vector
$\mathbf{T}$	transformation matrix
$\mathbf{x}$	vectorized laplacian in the transformed domain
J	J-divergence
$\mathbf{S}$	score

Table 4.1: Table of main notation in Chapter 4f.

ficiently estimate the adjacency matrix by creating and modifying embeddings related to each graph vertex. Since the estimation of FC requires a lot of time and computational resources, it is possible to cluster FC in communities of synchronous components. One example is the method introduced i n[64]. It consists in the application of k-means clustering followed by a tensor decomposition in order to reduce the FC data.

Classical signal processing operations have been generalized into the graph setting, where signals are associated to graph nodes, giving rise to the research domain of graph signal processing (GSP) [135, 167, 178]. GSP has already demonstrated the potential to characterize brain functioning in [80] and [81]. Indeed, GSP representation naturally reflects the human brain, where the structure is described by the graph itself while brain functioning corresponds to graph signals. An interesting application is represented by graph filtering [135, 157], that is useful to extract brain properties [163]. In [204], authors present a mathematical method to track brain fibers in order to describe neurophysiological processes. The model, based on GSP techniques, selects a subset of graph eigenvectors representing a basis for filtering fiber tracts from brain imaging data.

GSP has already been applied in the context of brain-computer interfaces with NIRS signals [144]. Specifically, GSP analysis is applied in [144] for feature extraction to obtain spatial information from the NIRS signals and it is proved to increase classification performances.

Classical signal processing and eigenvector-based filtering have already been

adopted with brain data [182, 185]. In [40] and [216], eigenvector-based filtering has been applied to fetal magnetic signals and diffuse optic imaging data to have more localized activities and reduce artefacts and noise. In particular, in [216], classical eigenvector-filtering, which is typically based on eigenvectors associated to larger eigenvalues, is used in diffuse optical imaging in order to improve connectivity estimation.

In the following sections, we propose a novel Laplacian denoising algorithm, and we demonstrate that it improves the detectability of two states. To this aim, we provide an analysis of the J-divergence, which naturally quantifies the distance between two distributions. Recently, the J-divergence has been applied in [103] to investigate the time series' irreversibility . Another recent application of the J-divergence is described in [130], where authors propose a novel framework to vector-skew the J-divergence. This method allows to preserve J-divergence properties and simultaneously to fine tune parameters for specific applications.

J-divergence has been also adopted in BCI design, to address one of the most challenging problem of EEG-based BCIs, that is the long calibration time. Indeed, the number of data necessary to calibrate the model is generally high, because of the presence of noise and artifacts the non-stationarity of EEG data. In [67], authors propose a subject-to-subject transfer learning to improve the classification performance when limited training data are available. J-divergence is used in a transfer learning framework to test the method by comparing the data of the target subject with the data from previous subjects.

In the following sections, we study the J-divergence under a different points of view, specifically i) we assess the performance of the denoising algorithm in distinguishing brain states and ii) we provide a score definition for Laplacian coefficients based on their contribution to the total J-divergence.

4.3 Signal Model

We analyse signals defined on an undirected, connected, weighted graph $G = \{V, E, \boldsymbol{A}\}$, which consists in a finite set of vertices (or nodes) V with $|V| = N$, a set of edges (or links) E and a weighted adjacency matrix $\mathbf{A}$. If there is an link $e = (i, j)$ connecting nodes i and j, the element $A_{i,j}$ represents the weight of the link; otherwise, $A_{i,j} = 0$.

The graph Laplacian, is a real symmetric matrix defined* as:

$$\boldsymbol{L} = \boldsymbol{D} - \boldsymbol{A} \tag{4.1}$$

*We refer here to the non-normalized graph Laplacian, also called the combinatorial Laplacian.

where $\boldsymbol{D}$ is the degree matrix, which is a diagonal matrix whose i^{th} diagonal element d_i is equal to the sum of the weights of all the edges incident to vertex i.

We define the set of orthonormal eigenvectors $\{\boldsymbol{u}_i\}_{i=0,1,...,N-1}$, corresponding to increasingly ordered eigenvalues $0 = \lambda_0 \leq \lambda_1 \leq \lambda_2 ... \leq \lambda_{N-1} = \lambda_{max}$.

In GSP, the Laplacian eigenvectors are represented as SoGs and constitute a basis for the Graph Fourier Transform (GST). The GFT is defined for a SoG $\mathbf{s}$ as the projection of $\mathbf{s}$ on the $l-$th eigenvector of the graph Laplacian:

$$\hat{s}(\lambda_l) = \mathbf{s}^H \mathbf{u}_l \tag{4.2}$$

The graph Laplacian eigenvalues $\lambda_l, l = 0, \cdots N-1$ have an similar interpretation to Fourier transform frequencies. Indeed, eigenvectors associated to smaller eigenvalues present smoother variations over connected nodes.

In many applications, such as brain functional connectivity estimation, SoGs are represented by discrete sequences, obtained by sampling time signals acquired at each graph node.

We denote the discrete sequences collected during an observation period T_{oss} with sampling pace T_s as $y_n[\nu T_s],\ n = 0, \dots N-1, k = 0, \dots N_s$, $N_s = \lfloor T_{oss}/T_s \rfloor$, or in vector form as $\boldsymbol{y}[\nu T_s] = [y_0[\nu T_s] \dots y_{N-1}[\nu T_s]]$ The vector sequence $\boldsymbol{y}[\nu T_s],\ k = 0, \dots N_s$ is used to compute the adjacency matrix A by estimating a similarity metric on each pair of nodes. There are many state-of-the-art procedures to estimate $A_{i,j}, i, j = 0, \cdots N-1$, which quantify links' weights according to specific interaction property [16, 30, 63, 131]. Since we do not have access to the real adjacency matrix $\mathbf{A}$, its estimated version $\hat{\mathbf{A}}$ is actually used. It contains the connectivity values $\hat{A}_{i,j}$ estimated for each graph node pair $(i, j), i, j = 0, \cdots N-1$.The estimated degree matrix $\hat{\mathbf{D}}$ is derived, so as to compute the estimated Laplacian $\hat{\mathbf{L}}$ as in Eq. (4.1), that becomes here:

$$\hat{\boldsymbol{L}} = \hat{\boldsymbol{D}} - \hat{\boldsymbol{A}} \tag{4.3}$$

Le us remark that any estimation error on the adjacency matrix affects the Laplacian estimate, and it results into less distinguishable connectivity states. In the following section we propose a denoising algorithm of the graph Laplacian in order to improve the separation of connectivity states. We generally refer to functional connectivity pattern associated to one condition as connectivity state.

4.4 Graph Connectivity Denoising

In order to describe the graph Laplacian denoising algorithm, we consider the eigenvalue decomposition of the estimated Laplacian $\hat{\mathbf{L}}$ as follows:

$$\hat{\mathbf{L}} = \sum_{i=0}^{N-1} \hat{\lambda}_i \hat{\mathbf{u}}_i \hat{\mathbf{u}}_i^H \tag{4.4}$$

Perturbations affect graph Laplacian estimation in terms of eigenvalues and/or eigenvectors. To elaborate on the effect of perturbations, we explicit the first, second and third order error contributions to $\hat{\mathbf{L}}$ as:

$$\begin{aligned}\hat{\mathbf{L}} &= \sum_{i=0}^{N-1} (\lambda_i + \boldsymbol{\epsilon}_{\lambda_i})(\mathbf{u}_i + \boldsymbol{\epsilon}_{u_i})(\mathbf{u}_i + \boldsymbol{\epsilon}_{u_i})^H \\ &= \sum_{i=0}^{N-1} \underbrace{\lambda_i \mathbf{u}_i \mathbf{u}_i^H}_{\boldsymbol{L}} + \underbrace{\lambda_i \mathbf{u}_i \boldsymbol{\epsilon}_{u_i}^H + \lambda_i \boldsymbol{\epsilon}_{u_i} \mathbf{u}_i^H + \boldsymbol{\epsilon}_{\lambda_i} \mathbf{u}_i \mathbf{u}_i^H}_{\textit{first order error}} \\ &+ \underbrace{\lambda_i \boldsymbol{\epsilon}_{u_i} \boldsymbol{\epsilon}_{u_i}^H + \boldsymbol{\epsilon}_{\lambda_i} \mathbf{u}_i \boldsymbol{\epsilon}_{u_i}^H + \boldsymbol{\epsilon}_{\lambda_i} \boldsymbol{\epsilon}_{u_i} \mathbf{u}_i^H}_{\textit{second order error}} + \underbrace{\boldsymbol{\epsilon}_{\lambda_i} \boldsymbol{\epsilon}_{u_i} \boldsymbol{\epsilon}_{u_i}^H}_{\textit{third order error}}\end{aligned} \tag{4.5}$$

We can approximate the estimated graph Laplacian at the first order as the sum of N terms:

$$\hat{\mathbf{L}} \approx \sum_{i=0}^{N-1} (\lambda_i + \boldsymbol{\epsilon}_{\lambda_i}) \boldsymbol{u}_i \boldsymbol{u}_i^H + \lambda_i (\boldsymbol{u}_i \boldsymbol{\epsilon}_{u_i}^H + \boldsymbol{\epsilon}_{u_i} \boldsymbol{u}_i^H) \tag{4.6}$$

Eq.(4.6) shows that the first order error is due to relative perturbation of the Laplacian eigenvalues as well as of the eigenvectors' direction. We are interested in the Laplacian components whose perturbation is low because either the relative eigenvalue perturbation $\epsilon_{\lambda_i}/\lambda_i$ or the eigenvector perturbation ϵ_{u_i} is small. We consider the set of orthonormal eigenvectors $\mathcal{U}_{ALL} = \{\hat{\boldsymbol{u}}_l, l = 0, 1, ..., N-1\}$ with increasingly eigenvalues $0 = \hat{\lambda}_0 \leq \hat{\lambda}_1 \leq \hat{\lambda}_2 ... \leq \hat{\lambda}_{N-1} := \hat{\lambda}_{max}$, and we consider three subsets of eigenvalues and associated eigenvectors: 1) the subset $\mathcal{U}_L$ with the N_L smallest eigenvalues; 2) the subset $\mathcal{U}_H$ with the N_H largest eigenvalues; and 3) the subset $\mathcal{U}_M$ with the remaining $N_M = N - N_L - N_H$ central eigenvalues, with $\mathcal{U}_L \cup \mathcal{U}_M \cup \mathcal{U}_H = \mathcal{U}_{ALL}$.

The first consideration is that the N_H largest eigenvalues are more robust to eigenvalue perturbations; this hypothesis is widely adopted in classical signal processing, where the subspace $\mathcal{U}_H$ is used for the estimation of the covariance matrix because of its favourable signal-to-noise ratio [132].

The second consideration is based on recent results [35], according to which the subspace $\mathcal{U}_L$ is partially robust in terms of eigenvector perturbations. In fact, Ceci and Barbarossa [35] demonstrated that a connectivity estimation error on the A_{ij} adjacency matrix element, i.e. on the weight of the link between the i-th and the j-th nodes, causes a perturbation $\boldsymbol{\epsilon}_{u_i}$ of the i-th eigenvector related to the difference between the i-th and the j-th coefficients of $\mathbf{u_i}$. As consequence, eigenvectors smoothly varying across the i-th and the j-th nodes are less affected by errors on A_{ij}.

On the other hand, it is well known in GSP theory that $\mathcal{U}_L$ eigenvectors corresponds to low frequency elements in the Graph Fourier Transform [202],[178] since they are characterized by the smallest changes over connected graph nodes. Thereby, the eigenvectors in $\mathcal{U}_L$ are characterized by a natural resilience to connectivity estimation error between connected nodes. To sum up, the eigenvectors in $\mathcal{U}_L$ are strongly related to the network topology, and therefore they need to be involved in the proposed denoising method.

Stemming on these observations, we introduce a novel denoising method which preserves the contribution to the Laplacian associated to the subspaces $\mathcal{U}_L$, $\mathcal{U}_H$ while eliminating those associated to the subspace $\mathcal{U}_M$. In formulas, given the estimated Laplacian

$$\hat{\mathbf{L}} = \sum_{i \in \mathcal{U}_L \cup \mathcal{U}_M \cup \mathcal{U}_H} \hat{\lambda}_i \hat{\mathbf{u}}_i \hat{\mathbf{u}}_i^H \tag{4.7}$$

we write the denoised Laplacian $\tilde{\mathbf{L}}$ as follows:

$$\tilde{\mathbf{L}} = \sum_{i \in \mathcal{U}_L} \hat{\lambda}_i \hat{\mathbf{u}}_i \hat{\mathbf{u}}_i^H + \sum_{i \in \mathcal{U}_H} \hat{\lambda}_i \hat{\mathbf{u}}_i \hat{\mathbf{u}}_i^H \tag{4.8}$$

The proposed graph Laplacian denoising algorithm presents a twofold approach which simultaneously preserves

- the subspace $\mathcal{U}_L$, which is directly related to the graph functional connectivity;
- the subspace $\mathcal{U}_H$, which is estimated with a favourable signal-to-noise ratio.

The proposed Laplacian denoising method, is synthetically presented in Algorithm 1. In essence, our method preserves the information relevant for graph connectivity characterization, and it rejects noisy components. In order to measure the improvement achieved in terms of connectivity states' separability, we use to the J-divergence as a measure of the distance between two states. In the following section we derive a novel formulation of the J-divergence.

4.5 Jensen divergence of connectivity states

Many state-of-the-art measures can be adopted to quantify the separability of two connectivity states [15], as represented by the Laplacian matrices L. Here, we apply the J-divergence to describe the separability of two connectivity states, and we propose a novel formulation to adapt it to our problem. Thus, J-divergence is applied to identify the Laplacian coefficients that are mostly relevant for detection and to measure the improvement achieved by the denoising algorithm.

We will assume in this analysis that the Laplacian coefficients obtained after the denoising algorithm are normally distributed. We remark that the Gaussian assumption stands in many applications*, including the case of FC estimation on real brain signals, and thereby it is often assumed in the literature, e.g. for Laplacian computation procedures [135]. In our case, we assume that the vector $\tilde{\mathbf{l}} = \mathrm{Vec}(\tilde{L})$ is distributed according to a multidimensional Gaussian probability whose mean vector and covariance matrix differ under two connectivity states, referred to as the *null* and the *alternative* hypotheses $\mathcal{H}_0$, $\mathcal{H}_1$ in the following: †

$$\begin{cases} \mathcal{H}_0 : \widetilde{\boldsymbol{l}} & \sim \mathcal{N}(\boldsymbol{\eta}_0, \mathbf{K}_0) \\ \mathcal{H}_1 : \widetilde{\boldsymbol{l}} & \sim \mathcal{N}(\boldsymbol{\eta}_1, \mathbf{K}_1) \end{cases} \tag{4.9}$$

We compute the Jensen divergence in order to obtain an information theoretic measure of distance between $\tilde{\mathbf{l}}$ under $\mathcal{H}_0$ and $\mathcal{H}_1$.The J-divergence is defined as the expected value of the difference of the Log Likelihood Ratio under the two hypothesis $\mathcal{H}_0$ and $\mathcal{H}_1$ [146]. The J-divergence formulation enables us to evaluate to which extent the connectivity states represented by the Laplacian elements are distinguishable from each other.

Let us first assume that the moments of the Laplacians $\boldsymbol{\eta}_0$,$\boldsymbol{\eta}_1$,$\mathbf{K}_0$,$\mathbf{K}_1$ are known. Detection procedure can be applied on a linear transformation of original observations:

$$\mathbf{x} = \mathbf{T}\left(\widetilde{\boldsymbol{l}} - \boldsymbol{\eta}_0\right)$$

where $\boldsymbol{\eta} \stackrel{\text{def}}{=} \mathbf{T}(\boldsymbol{\eta}_1 - \boldsymbol{\eta}_0)$ and $\mathbf{T} = \mathcal{T}(\mathbf{K}_0, \mathbf{K}_1)$ is an affine transformation that simultaneously‡ whitens the observations in the $\mathcal{H}_0$ hypothesis and produces uncorre-

*The reason why this occurs is that the Gaussian assumption tightly models laplacian diagonal elements, computed in each row as the sum of extradiagonal elements in that column, as well as extradiagonal elements which are often computed as the result of correlation estimates.

†The notation $\widetilde{\boldsymbol{l}} \sim \mathcal{N}\left(\boldsymbol{\eta}_j, \mathbf{K}_j\right)$, with $j \in \{0,1\}$ indicates that the random vector $\widetilde{\boldsymbol{l}}$ is Gaussian distributed with mean vector $\boldsymbol{\eta}_j$ and covariance matrix $\mathbf{K}_j$.

‡The matrix $\mathbf{T}$ and the diagonal matrix $\boldsymbol{\Sigma}^2 \stackrel{\text{def}}{=} \mathrm{diag}(\sigma_1^2, \ldots, \sigma_n^2, \ldots, \sigma_{N'}^2)$ are computed as the *gen-*

lated observations in the $\mathcal{H}_1$ hypothesis. A graphical example of the effect of the transform T, is presented in Fig. 4.1 for the case of bidimensional Gaussian data whose mean and covariance matrix differ under the $\mathcal{H}_0, \mathcal{H}_1$. The original data are represented in Fig. 4.1 a), whereas their transformed versions are plotted in Fig. 4.1 b). The transformed data are unitary variance, zero-centered under $\mathcal{H}_0$ and they are uncorrelated under $\mathcal{H}_1$.

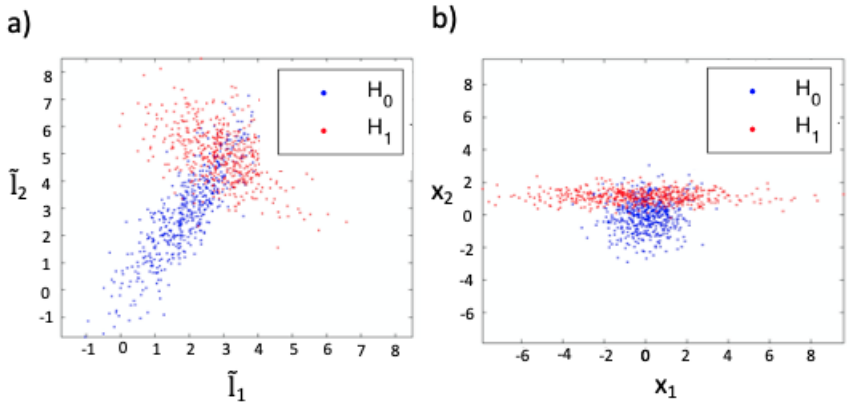

Figure 4.1: Example of transformation effect. In a) we have bidimensional Gaussian distributions which differ under mean and covariance matrix . In b) we have data in the transformed domain

In real systems, the Laplacian moments $\boldsymbol{\eta}_0, \boldsymbol{\eta}_1, \mathbf{K}_0, \mathbf{K}_1$ can be either estimated in a training set, e.g. during a BCI training, or tracking procedures can be applied [37, 71, 74]. Besides, data in the transformed domain $\mathbf{x}$ can be obtained even avoiding computation of moments and of T, by applying the Laplacian coefficients $\tilde{\mathbf{I}}$ to a trained network [4], in order to enforce the afore-mentioned statistical constraints.

The observation model becomes:

$$\mathcal{H}_0 : \mathbf{x} \sim \mathcal{N}(\mathbf{0}, \mathbf{I}) \text{ versus } \mathcal{H}_1 : \mathbf{x} \sim \mathcal{N}(\boldsymbol{\eta}, \boldsymbol{\Sigma}^2) \tag{4.10}$$

The J-divergence is defined as:

$$J \stackrel{\text{def}}{=} \mathbb{E}(\mathcal{R}(\mathbf{x})|\mathcal{H}_1) - \mathbb{E}(\mathcal{R}(\mathbf{x})|\mathcal{H}_0) \tag{4.11}$$

eralized eigenvectors and the *generalized eigenvalues* matrices of the pencil $(\mathbf{K}_1, \mathbf{K}_0)$, respectively. Given any square root $\mathbf{Q}_0$ of $\mathbf{K}_0^{-1}$, *i.e.* such that $\mathbf{Q}_0^{\mathrm{H}} \cdot \mathbf{K}_0 \cdot \mathbf{Q}_0 = \mathbf{I}$, we may conveniently employ the unitary transformation $\mathbf{V}_1$ obtained from the eigenanalysis $\mathbf{Q}_0^{\mathrm{H}} \cdot \mathbf{K}_1 \cdot \mathbf{Q}_0 = \mathbf{V}_1 \cdot \boldsymbol{\Lambda}_1 \cdot \mathbf{V}_1^{\mathrm{H}}$; in fact, it is easily proved that the matrix $\mathbf{T} = \mathbf{V}_1^{\mathrm{H}} \cdot \mathbf{Q}_0^{\mathrm{H}}$ verifies $\mathbf{T} \cdot \mathbf{K}_0 \cdot \mathbf{T}^{\mathrm{H}} = \mathbf{I} \quad ; \quad \mathbf{T} \cdot \mathbf{K}_1 \cdot \mathbf{T}^{\mathrm{H}} = \boldsymbol{\Sigma}^2$ with $\boldsymbol{\Lambda}_1 = \boldsymbol{\Sigma}^2$.

being $\mathcal{R}(\mathbf{x})$ the Log-Likelihood Ratio*:

$$\mathcal{R}(\mathbf{x}) = \mathbf{x}^{\mathrm{H}} \left(\mathbf{I} - \boldsymbol{\Sigma}^{-2}\right) \mathbf{x} + 2\boldsymbol{\eta}^{\mathrm{H}} \boldsymbol{\Sigma}^{-2} \mathbf{x} \tag{4.12}$$

Here, we associate the variables x_n whose variance $\sigma_n^2 \neq 1$ to the first P indexes and the remaining ones to the indexes $n = P+1, \ldots, N'$† so as to rewrite the LLR as follows:

$$\begin{aligned} \mathcal{R}(\mathbf{x}) &= \sum_{n=1}^{N'} \frac{1}{\sigma_n^2} \left[\left(\sigma_n^2 - 1\right) x_n^2 + 2\eta_n \cdot x_n\right] \\ &= \sum_{n=1}^{P} \frac{\left(\sigma_n^2 - 1\right) |x_n|^2 + 2\eta_n \cdot x_n}{\sigma_n^2} \\ &\quad + \sum_{n=P+1}^{N'} 2\eta_n^* \cdot x_n \end{aligned} \tag{4.13}$$

By adding and subtracting the term $|\eta_n^2|/[\sigma_n^2(\sigma_n^2 - 1)]$ we rewrite the equation (4.13) as:

$$\mathcal{R}(\mathbf{x}) = \underbrace{\sum_{n=1}^{P} \frac{\sigma_n^2 - 1}{\sigma_n^2} \left| x_n + \frac{\eta_n}{\sigma_n^2 - 1} \right|^2}_{P \text{ quadratic terms}} + \underbrace{\sum_{n=P+1}^{N'} 2\eta_n \cdot x_n}_{N'-P \text{ linear terms}} \quad \underbrace{- \sum_{n=1}^{P} \frac{|\eta_n^2|}{\sigma_n^2 \left(\sigma_n^2 - 1\right)}}_{\text{constant to be included in the threshold}} \tag{4.14}$$

The P variates $x_n,\ n = 1, \ldots, P$, have different conditional variances under the hypotheses $\mathcal{H}_0, \mathcal{H}_1$ and they contribute to the LLR by the P terms quadratic terms. The $N'-P$ variates $x_n,\ n = P+1, \ldots, N'$, with equal unitary conditional variances under the hypotheses $\mathcal{H}_0, \mathcal{H}_1$, contribute to the LLR by the $N'-P$ linear terms.

To deepen the J-divergence, we present the following theorem, whose demonstration is in Appendix E.

THEOREM 1 *Let $\boldsymbol{\xi}$ be a vector formed by the N statistically independent random variables:*

$$\begin{aligned} \xi_n &= \left(x_n + \frac{\eta_n}{\sigma_n^2 - 1}\right)^2,\ n = 1, \ldots, P \\ \xi_n &= x_n,\ n = P+1, \ldots, N' \end{aligned} \tag{4.15}$$

---

*The Log-Likelihood Ratio $\mathcal{R}(\mathbf{x})$ is widely adopted classical detection problems: $\mathcal{R}(\mathbf{x}) \underset{\mathcal{H}_0}{\overset{\mathcal{H}_1}{\gtrless}} \theta$, where θ is selected according to the desired detection versus missing probability trade-off.

†We might have $P = N$ or $P = 0$.

The LLR is written as $\mathcal{R}(\mathbf{x}) = \mathbf{a}_{\mathrm{LLR}}^{\mathrm{H}} \cdot \boldsymbol{\xi}$ *being* $\mathbf{a}_{\mathrm{LLR}}$ *constant coefficients defined as in Eq.*(4.26) *and the J-divergence in Eq.*(4.11) *is computed as follows:*

$$\begin{aligned} J &= \sum_{n=1}^{P} \left(\sigma_n - \sigma_n^{-1}\right)^2 \left[1 + \frac{|\eta_n^2|}{\sigma_n} \frac{\sigma_n + \sigma_n^{-1}}{\left(\sigma_n - \sigma_n^{-1}\right)^2}\right] + \sum_{n=P+1}^{N'} 2|\eta_n^2| \\ &= \sum_{n=1}^{P} J_n^{(\sigma,\eta)} + \sum_{n=P+1}^{N'} J_n^{(\eta)} \end{aligned} \tag{4.16}$$

Theorem 1 generalizes the result in [146, 170] where only the case of variables having equal conditional means and different covariances (i.e. $\boldsymbol{\eta}_1 = \boldsymbol{\eta}_0$, $\mathbf{K}_1 \neq \mathbf{K}_0$) has been considered.

The J-divergence as formulated in Eq.(4.16) is a measure of the statistical distance of the Laplacian coefficients under two conditions, and it is suitable to quantify the separability of connectivity states achieved by the denoising algorithm described in section 4.4.

In addition, the J-divergence analysis provides an information on the variables that mostly contribute to the states separability. From Eq.(4.16), we see a one-to-one correspondence between the transformed variables $\boldsymbol{x}_n$ and the terms of the J-divergence J; besides, this term can be:

$$\begin{aligned} J_n^{(\sigma,\eta)} &= \left(\sigma_n - \sigma_n^{-1}\right)^2 \left[1 + \frac{|\eta_n^2|}{\sigma_n} \frac{\sigma_n + \sigma_n^{-1}}{\left(\sigma_n - \sigma_n^{-1}\right)^2}\right] \\ J_n^{(\eta)} &= 2|\eta_n^2| \end{aligned} \tag{4.17}$$

The nature of J-divergence terms depends on whether the variable changes both in conditional mean and standard deviation, or in conditional mean only. The functions $J_n^{(\sigma,\eta)}, J_n^{(\eta)}$ are plotted in Fig.4.2 for η between 0 and 1 and σ^{-1} from 0 to 10. Fig.4.2 shows that a conditional variance change gives a higher contribution to J than an equal conditional mean change.

In conclusion, the J-divergence analysis highlights the contribution of each transformed variable to the separability of the connectivity states. Consequently, it suggests a ranking procedure for $\boldsymbol{x}_n$ according to their contribute to J_n, in order to identify variables which mostly differ under the two hypothesis. This opens new ways to score Laplacian coefficients.

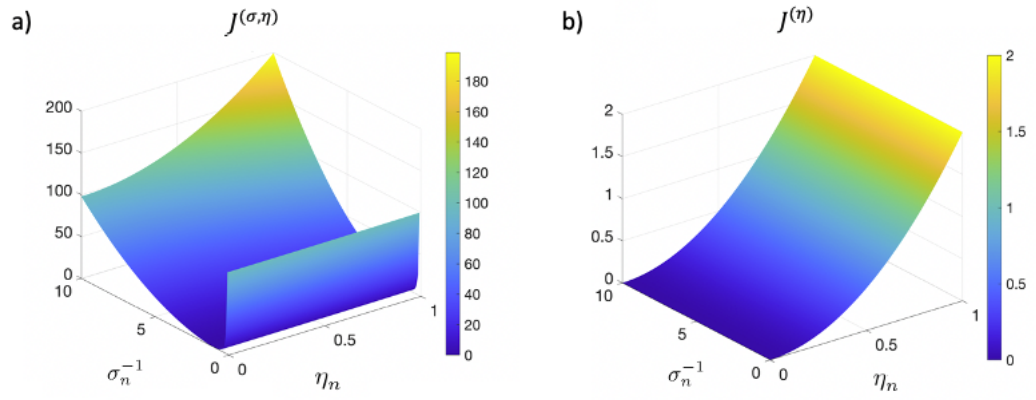

Figure 4.2: J-Divergence contributions as function of mean η and standard deviation σ: a) $J^{(\sigma,\eta)}$ for variables whose conditional standard deviation differ under $\mathcal{H}_1$ and $\mathcal{H}_0$, and b) $J^{(\eta)}$ for variables with invariant conditional standard deviation.

4.5.1 J-Divergence based Laplacian coefficients scoring

After the J-divergence analysis, we are able to identify Laplacian elements (i.e. links weights or nodes degrees), mostly contributing to the connectivity states separability. This is obtained by associating a score to each Laplacian element according to its contribution to the J-divergence.

By definition, the Laplacian elements $\tilde{l}_{\overline{n}}$, $\overline{n} = 0, \cdots N' - 1$, are combined in the transformed domain and they generate the variable x_n. We define a score $S_{\overline{n}}$ computed by means of a backpropagation procedure of the J_n terms on each contributing Laplacian coefficient. Specifically, the $\overline{n}$-th coefficient score is computed as

$$S_{\overline{n}} = \sum_n J_n \cdot \frac{t_{n\overline{n}}}{\sum_k t_{nk}} \tag{4.18}$$

where we recognize that the weight $t_{n\overline{n}}$ that brings the contribution of the $\overline{n}$-th Laplacian coefficient to the n-th transformed variable is normalized with respect to the sum $\sum_k t_{nk}$ of the weights of all the contributing coefficients.

A representation of the score rational is provided in Fig.4.3, where we have a set of variables $\tilde{\mathbf{l}}$ belonging to the original domain (left), a set of variables $\mathbf{x}$ belonging to the transformed domain (center) and the corresponding marginal contributions to J (right). The relationship between $\tilde{\boldsymbol{l}}$ and $\boldsymbol{x}$ is defined by the transformation matrix $\boldsymbol{T}$. Each J-divergence component J_n (coloured circle on the right) directly corresponds to the variable $\boldsymbol{x_n}$ in the transformed domain, which is originated by several $\tilde{\boldsymbol{l}}_n$ (shaded colored box on the left). Follwing the proposed procedure, J_n is backprojected to the original space by weighting its contribution

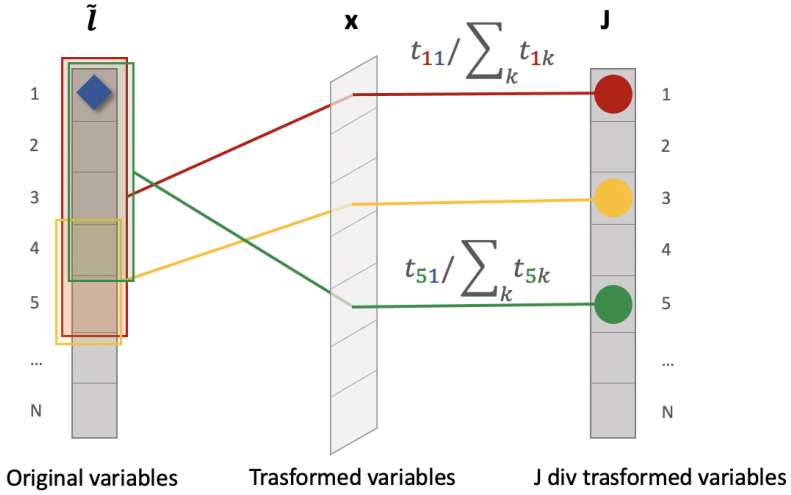

Figure 4.3: Graphic interpretation of the score computed for the first element in the vector $\tilde{l}$

as in Eq. (4.18). Back-projection and accumulation can also be performed by limiting the summation in Eq.(4.18) to the largest ranking J_n terms.

To sum up, the score procedure enables to numerically quantify the relevance of the Laplacian elements $\tilde{\mathbf{l}}_{\overline{n}}$ to separate connectivity states. The Algorithm 2 presents the main steps of the J-divergence computation and scoring procedure.

4.6 Results on synthetic data

In this section, we investigate the ability of graph Laplacian denoising described in section 4.4 to increase the J-divergence between two connectivity states derived from synthetic SoGs. We firstly define a graph and a model for SoGs under two connectivity states, identified to simulate an over-simplified model of brain EEG signals functional connectivity.

For comparison's sake, we also consider the case of Laplacian without filtering $\mathcal{U}_{ALL}$ and and other eigenvector-based filters (i.e. $\mathcal{U}_L$, $\mathcal{U}_H$). Here, we explain in detail the Laplacian generation procedure and the analyses we perform.

4.6.1 Signal on Graph generation and connectivity estimation

In order to test our procedure on synthetic data, we define signals at graph nodes under two hypothesis $\mathcal{H}_0$ and $\mathcal{H}_1$ to obtain graphs related to two connectivity

Algorithm 4.1 Graph Laplacian denoising

Input: Estimated Laplacian $\tilde{L}$
Output: Denoised Laplacian $\tilde{L}$

1: Compute the eigen-decomposition

$$\hat{L} = \sum_{i=0}^{N-1} \hat{\lambda}_i \hat{\mathbf{u}}_i \hat{\mathbf{u}}_i^H$$

2: Compute the denoised Laplacian $\tilde{L}$ by
a: Selecting the number N_L, of smallest eigenvalues and the number N_H of largest eigenvalues to retain
b: Computing

$$\tilde{L} = \sum_{i=0}^{N_L-1} \hat{\lambda}_i \hat{\mathbf{u}}_i \hat{\mathbf{u}}_i^H + \sum_{i=N-N_H}^{N-1} \hat{\lambda}_i \hat{\mathbf{u}}_i \hat{\mathbf{u}}_i^H$$

states.

Under $\mathcal{H}_1$, we model the brain activity by considering H generator signals $s^{(h)}[\nu T_s], h = 0, \cdots H-1$. Each generator signal contributes to the signals measured over a subset $\mathcal{G}^{(h)}, h = 0, \cdots H-1$ of nodes identified by the non-zero components of the $N \times 1$ binary vector $\mathbf{g}^{(h)}, h = 0, \cdots H-1$. Perturbations are also present on the model, both in term of a noise component $\mathbf{w}[\nu T_s]$ as well as a common component across all the nodes $b[\nu T_s] \cdot \mathbf{1}$. Under $\mathcal{H}_0$, only these perturbation-related components are observed. Taken together, we define the vector of the observed signals $\mathbf{y}[\nu T_s]$ under the two hypotheses $\mathcal{H}_1$ and $\mathcal{H}_0$ as follows:

$$\begin{aligned} \mathcal{H}_1 &: \mathbf{y}[\nu T_s] = \sum_{h=0}^{H-1} s^{(h)}[\nu T_s] \cdot \mathbf{g}^{(\mathbf{h})} + \mathbf{w}[\nu T_s] + b[kT_s] \cdot \mathbf{1} \\ \mathcal{H}_0 &: \mathbf{y}[\nu T_s] = \mathbf{w}[\nu T_s] + b[\nu T_s] \cdot \mathbf{1} \end{aligned} \tag{4.19}$$

The noise $\mathbf{w}[\nu T_s]$ is a realization of a discrete, stationary, white Gaussian process, with $E\{\mathbf{w}[\nu]\} = 0$, $E\{\mathbf{w}[\nu]\mathbf{w}[\nu]^T\} = \sigma_w^2 I \ \forall \nu$; the samples of discrete sequences $b[\nu T_s]$ are extracted from a zero mean Gaussian random distribution with variance σ_b^2; and $s^{(h)}[\nu T_s], h = 0, \cdots H-1$ are extracted from a zero mean unit variance Gaussian random variable.

Once SoG samples $\mathbf{y}[\nu T_s]$ are defined, we estimate the adjacency matrix. There are many state-of-the-art methods to estimate the adjacency matrix such as spectral coherence [30], wavelet coherence [39], Granger causality [213] which describe brain interactions between two nodes i, j in different ways. Here, we use spectral coherence:

Algorithm 4.2 J-divergence and score computation

Input: Conditional means μ_0, μ_1 and covariance matrices K_0, K_1 of $\tilde{\mathbf{l}} = \text{Vec}(\tilde{l})$ under $\mathcal{H}_1$ and $\mathcal{H}_0$
Output: J_n, S_n, $n = 0, \cdots N-1$

1: Step 1: Transform computation
   a: Compute the square root matrix

$$Q_0 \leftarrow K_0^{-1/2}$$

   and the eigenvectors V_1 and the eigenvalues $\sigma_0^2, \cdots \sigma_{N-1}^2$ of the eigen-decomposition

$$Q_0^H K_1 Q_0 = V_1 \,\text{diag}\left(\sigma_0^2, \cdots \sigma_{N-1}^2\right) V_1^H$$

   b: Compute T as $\leftarrow V_1^H Q_0^H$ and $\Sigma \leftarrow \sqrt{(eig(Q_0^H K_1 Q_0)')}$
2: Step 2: J-divergence computation
   a: Define a threshold θ
   b: Compute J_n, $n = 0, \cdots N' - 1$ as

$$J_n \leftarrow \begin{cases} 2|\eta_n^2|, \iff \left(\sigma_n^2 > \theta\right) \cup \left(|\sigma_n^2 - 1| > \theta\right) \\ \left(\sigma_n - \sigma_n^{-1}\right)^2 \left[1 + \dfrac{|\eta_n^2|}{\sigma_n} \dfrac{\sigma_n + \sigma_n^{-1}}{\left(\sigma_n - \sigma_n^{-1}\right)^2}\right], \text{otherwise} \end{cases}$$

   ,
3: Step 3: Score computation
   a: Compute $S_{\overline{n}}$, $\overline{n} = 0, \cdots N-1$ as

$$S_{\overline{n}} = \sum_n J_n \cdot \frac{t_{n\overline{n}}}{\sum_k t_{nk}}$$

$$C_{ij}(\omega_k) = \frac{|\hat{P}_{ij}(\omega_k)|}{\sqrt{\hat{P}_i(\omega_k) \cdot \hat{P}_j(\omega_k)}} \tag{4.20}$$

In Eq. (5.11), $\hat{P}_i(\omega_k)$, $\hat{P}_j(\omega_k)$ and $\hat{P}_{ij}(\omega_k)$ are the the estimated auto-spectra and cross-spectrum of the signals $y_i[\nu T_s]$, $y_j[\nu T_s]$ at the nodes i and j, computed at the frequency bin* $\omega_k = \dfrac{2\pi}{N_s} k$. Given $C_{ij}(\omega_k)$ as in Eq. (5.11), the adjacency matrix $\hat{\boldsymbol{A}}$, is estimated by averaging across the N_s frequency bins as follows:

$$\hat{A}_{ij} = \sum_{k=0}^{N_s - 1} C_{ij}(\omega_k) \tag{4.21}$$

*All the power spectral estimates are computed with Welch method, with 1s length Hanning windows and overlap of 50%.

The proposed signal model for synthetic data generates a simple graph connectivity under the two hypotheses $\mathcal{H}_1$ and $\mathcal{H}_0$. This model successfully simulates graphs characterized by distinct connectivity states in presence of controlled perturbations.

Fig. 4.4 represents the estimated adjacency matrices under the two conditions $\mathcal{H}_1$ and $\mathcal{H}_0$ in presence of perturbations. Under $\mathcal{H}_1$ some strong connections are present and their value is affected by the perturbations. Under $\mathcal{H}_0$ (4.4 B) there are no evident link and $\hat{A}$ fluctuates around zero because of the perturbations.

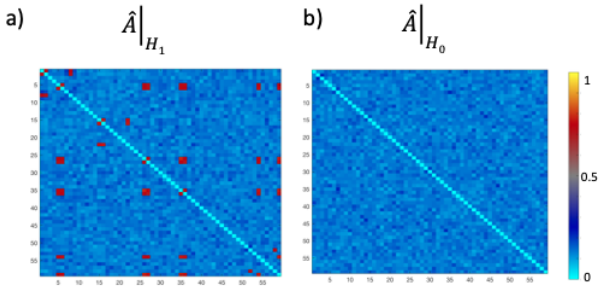

Figure 4.4: Adjacency matrix with synthetic data. $\hat{A}_{ij}$ is represented under $\mathcal{H}_1$ in A) and under $\mathcal{H}_0$ in panel B).

Once we have computed the adjacency matrix under $\mathcal{H}_1$ and $\mathcal{H}_0$, we derive the estimated Laplacians as in Eq. (5.9) and then, we decompose it with its eigenvalues and eigenvectors as in Eq. (4.4). In order to visualize the eigenvectors' behaviour on graph, we represent in Fig. 4.5 the first and the $10th$ eigenvectors on graph under $\mathcal{H}_1$ hypothesis. The first eigenvector, in Fig. 4.5 A) is completely smooth on the graph and within a subset of connected nodes. Fig. 4.5 B) represents the $10th$ eigenvector on graph. Its variations over the graph highlight another community, but it has higher variability over connected node compared to the first eigenvector.

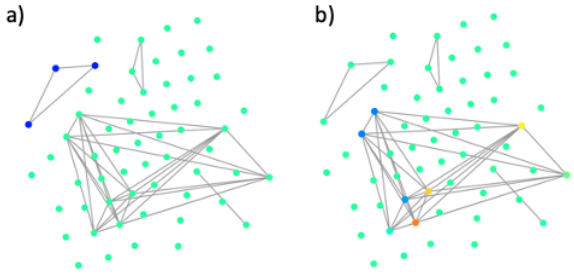

Figure 4.5: Example of eigenvectors on graph. They relate to the Laplacian matrix estimated from synthetic data under $\mathcal{H}_1$

The proposed generation model will be applied in the following to validate

the Laplacian denoising framework. In this direction, we produce 20 random repetitions (or trials) of synthetic SoGs for each statistical hypothesis, as i.i.d. realizations of our model with a fixed set of parameters.

4.6.2 Subspace robustness on synthetic data

In this subsection, we investigate the robustness of Laplacian denoising based on $\mathcal{U}_L \cup \mathcal{U}_H$, shortly denoted as $\mathcal{U}_{L\cup H}$, and we compare it with other subspaces, notably $\mathcal{U}_{ALL}$, $\mathcal{U}_L$ and $\mathcal{U}_H$.

In order to quantify the subspace robustness, for each subspace (ie. $\mathcal{U}_{L\cup H}$, $\mathcal{U}_{ALL}$, $\mathcal{U}_L$ and $\mathcal{U}_H$) we take into consideration two cases, namely the absence and the presence of perturbation, which we indicate as the ground truth (GT) and the noisy cases, respectively. Each GT subspace is compared to several noisy configurations, corresponding to $\sigma_w = 0, 1.2$ for noise and $\sigma_b = 0, 2$ for polarization. To measure subspace robustness on synthetic data, we compute the Frobenius subspace distance F [12] between the GT case and the noisy configurations, changing the perturbation levels*. We report results of Frobenius distance analysis in Fig. 4.6. We plot F as function of trials for the different subspaces, specifically $\mathcal{U}_H$ (red), the subspace $\mathcal{U}_L$ (green), and the subspace $\mathcal{U}_{L\cup H}$ (blue) in several perturbation scenarios. In Fig. 4.6a) the GT case is represented, in which, not surprisingly, $F = 0$ for every subspace and every trial. If we gradually increase perturbations (i.e. only noise in Fig.4.6b) or only polarization in Fig.4.6c)), the most favourable case is $\mathcal{U}_H$ for almost every trial. When perturbations dramatically increase Fig.4.6d), performances decrease in particular for $\mathcal{U}_H$ configuration. In this figure, we do not have results for $\mathcal{U}_{ALL}$ case because $F = 0$ for all the trials and independently from perturbations.

It is then clear that the eigenvectors in $\mathcal{U}_H$ are more robust compared to the others. This result is not surprising, since in classical signal processing $\mathcal{U}_H$ eigenvectors are widely used because of their advantages in terms of signal-to-noise-ratio (SNR). Besides, the subspace $\mathcal{U}_{L\cup H}$ maintains the robustness, while being relevant to describe the network topology In the following analyses. In the folloowing, we verify that the Laplacian denoising based on the subspace $\mathcal{U}_{L\cup H}$ leads to more separate connectivity states in presence of perturbations.

*For each subspace configuration, we compute the Frobenius distance F between its noisy and GT versions. See **Definition 2** in [12] for the mathematical formulation.

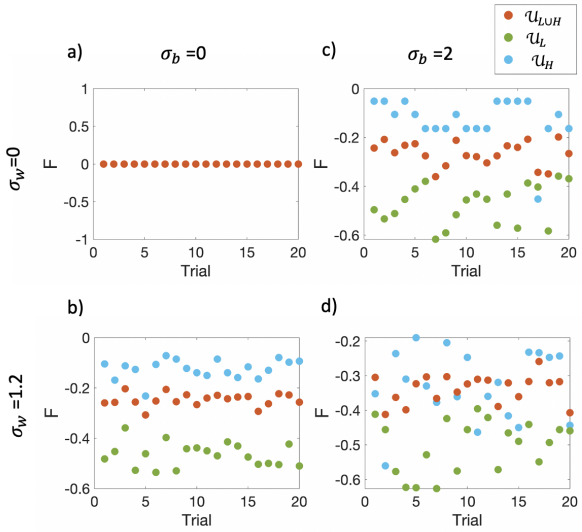

Figure 4.6: Results of Frobenius distance on synthetic data. Several perturbation configurations are represented: in panel a)σ_w=0 and σ_b=0,in panel b) σ_w=1.2 and σ_b=0,in panel c) σ_w=0 and σ_b=2 and in panel d) σ_w=1.2 and σ_b=2. In the different colors (in the legend) we represent the different subspaces.

4.6.3 J-divergence computation on synthetic data

Finally, we test the ability to separate graph Laplacians under $\mathcal{H}_1$ and $\mathcal{H}_0$. The J-divergence analysis in Section 4.5 ends with a measure of the statistical distance J between two states. In the following subsection, we apply this analysis to graph Laplacians derived from synthetic data in order to compare the discriminant ability of the proposed denoising method with respect to the other subspace configurations, i.e. $\mathcal{U}_{ALL}$, $\mathcal{U}_L$ and $\mathcal{U}_H$.

In several perturbation configurations, we compute the total J as a measure of statistical distance between the two conditions i.e. related to the hypothesis that the Laplacian matrix comes from $\mathcal{H}_1$ or $\mathcal{H}_0$) and we estimate the marginal J_n as measure of the contribution of each n-variable to the total separability. Table 4.2 contains J-divergence values obtained for several perturbation levels and for the different subspaces. Results show that in absence of perturbations the most favourable subspace is $\mathcal{U}_{ALL}$. This result is quite intuitive because without perturbations there is no reason why reduced subspaces should better discriminate. If perturbations (i.e. noise and polarization) increase, the most favourable case becomes $\mathcal{U}_{L\cup H}$, which gives the highest J. It means that graph Laplacian denoising based on $\mathcal{U}_{L\cup H}$ offers the highest separability between the two connectivity states, even in presence of high perturbation. Fig 4.7 shows the marginal J-divergence J_n as function of the first 20 variables only for U_{ALL} and $U_{L\cup H}$ subspaces. These

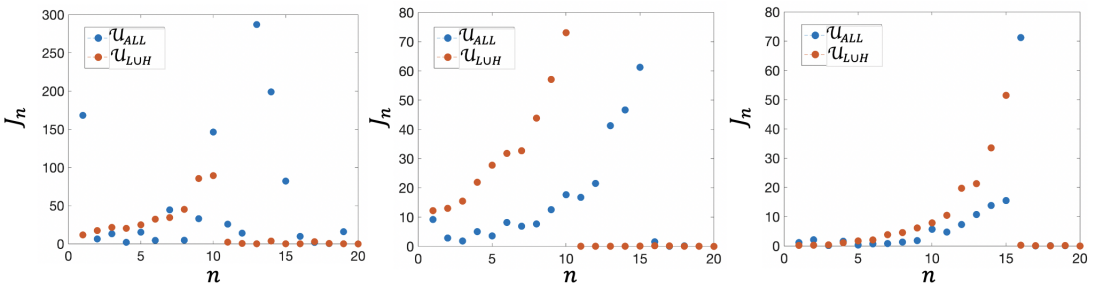

Figure 4.7: Results of J-divergence analysis on synthetic data. Several perturbation configurations are represented: in panel a) σ_w=0 and σ_b=0, in panel b) σ_w=1.2 and σ_b=0, in panel c) σ_w=1.2 and σ_b=2. In the different colors (shown in the legend) we represent the different subspaces for the filtering.

representations show the contribution of n variables to the total J and we find that increasing perturbations, variables in $U_{L\cup H}$ generally give higher J_n contributions compared to U_{ALL}.

	$\mathcal{U}_H$	$\mathcal{U}_L$	$\mathcal{U}_{L\cup H}$	$\mathcal{U}_{ALL}$
σ_w=0 σ_b=0	85.42	265.15	392.98	**1073.93**
σ_w=1.2 σ_b=0	223.58	294.25	**329.19**	264.38
σ_w=1.2 σ_b=2	188.10	106.77	**313.53**	150.60

Table 4.2: J-divergence values on synthetic data. We report in bold characters the highest J-divergence value for each perturbation configuration.

To conclude, our results with synthetic data demonstrate that in presence of perturbations the Laplacian denoising algorithm succeeds in distinguishing graphs under two conditions. This consideration remains true if the system is perturbed by noise but also if there is an artefact of a different nature , i.e. a common artefact that we indicated as polarization.

4.7 Real BCI measurements

In this section, we apply the Laplacian denoising procedure on real data, recorded during motor-imagery BCI experiments. In this case the $\mathcal{H}_1$ and $\mathcal{H}_0$ hypotheses directly correspond to the hypotheses that subject performs motor imagery ($\mathcal{H}_1$) or he/she is in resting state ($\mathcal{H}_0$).

4.7.1 Experimental Protocol and Preprocessing

Twenty healthy subjects (aged 27.60 ± 4.01 years, 8 women), all right-handed, participated to the study. They received financial compensation for their participation and signed a written informed consent. The ethical committee CPP-IDF-VI of Paris approved the experimental protocol. During the experiments, subjects were seated in front of a screen with a target. They were instructed to perform a right hand-based motor imagery task (i.e. grasping movement) when the target was up, and to rest when the target was down [210]. EEG data were recorded with 74 channels in a standard 10-10 configuration.

The reference for EEG recordings was set to mastoids and the ground electrode was located on the left scalpula; the impedences were lower than 20 kOhms. The sampling frequency was originally 1 kHz, and then downsampled to 250 Hz. For each subject, EEG data have been segmented to obtain N_T trials for motor imagery and N_T trials for resting state. The length of each trial was 5s.

A preliminary preprocessing analysis was performed. More precisely, an Independent Component Analysis (ICA) with the Infomax Algorithm [18] was applied to original data to eliminate artefacts, such as ocular and cardiac signals [54].

4.7.2 J-divergence of brain connectivity states

We perform the J-divergence analysis on real EEG data. To this aim, we consider EEG signals from one subject and N_T trials for $\mathcal{H}_1$ and N_T trials for $\mathcal{H}_0$, with $N_T = 20$. We use spectral coherence to estimate the connectivity matrix, as in Eq. (5.11). Then, we derive the estimated adjacency matrix $\hat{\boldsymbol{A}}$ as in Eq. (4.21), and through the Eq. (5.9), we can compute $\hat{\boldsymbol{L}}$. As for synthetic data, we derive the filtered graph Laplacian $\tilde{\boldsymbol{L}}$ with $\mathcal{U}_{L\cup H}$. In order to compare results of denoising procedure applied to real data, we also consider the $\mathcal{U}_{ALL}$, $\mathcal{U}_H$, $\mathcal{U}_L$ subspaces. In each case, we estimate the J-divergence J as in Eq. (4.11) and the marginal contribution J_n associated to the n-th variable as in Eq.(4.16).

	$\mathcal{U}_H$	$\mathcal{U}_L$	$\mathcal{U}_{L\cup H}$	$\mathcal{U}_{ALL}$
Real data	155.76	98.89	**162.42**	155.87

Table 4.3: J-divergence values obtained with real EEG data. We highlight with bold characters the highest J-divergence value.

In Table 4.3, we report J-divergence values related for each subspace configuration. Comparing all the cases, the highest J-divergence value is obtained with $\mathcal{U}_{L\cup H}$ case. This result is very important because it means that the subspace $\mathcal{U}_{L\cup H}$

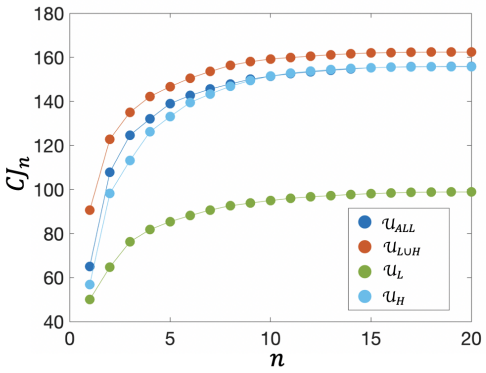

Figure 4.8: Results of J-divergence analysis for real EEG data. We report the cumulative J-divergence CJ_n as function of the first 20 variables. In the different colors (shown in the legend) we represent the different subspaces used to filter Laplacian.

is appropriate to separate real EEG data and it is useful to correctly identify the subject's mental state.

In order to understand the contributions of different variables, we firstly compute the J_n marginal contributions to associate a weight to each and every variable in the transformed domain. Then, we compute the cumulative sum of the first n variables. Specifically, once the J_n vector is sorted, we estimate the cumulative J-divergence CJ_n to quantify the impact of the variables to the J-divergence:

$$CJ_n = \sum_{k=1}^{n} J_k \tag{4.22}$$

Results in Fig. 4.8 demonstrate that the cumulative sum CJ_n of the first 20 variables is generally higher for $\mathcal{U}_{L\cup H}$ than all the other subspace cases. Express differently, if a given number of variables are retained, the overall achieved J-divergence is always larger using the proposed denoising algorithm. This result confirms the improvement to the discrimination of the two cognitive states achieved by the proposed Laplacian denoising.

4.7.3 Scoring of Laplacian coefficients in beta band

Given that the denoising with $\mathcal{U}_{L\cup H}$ allows a better discrimination between motor imagery and resting state, we now investigate the score performances to identify which Laplacian coefficients mostly contribute to separate the two mental states.

To proceed, it is important to remark that the brain response to cognitive tasks is in general not uniform across the frequencies, but it is mostly evident in α (8-13

Hz) or β (14-29 Hz) band, depending on the subject and the task [117].

Here, we perform the analysis in β frequency band, but in a training BCI scenario, the frequency band, or eventually the frequency bin, can be tuned according to the subject response. For this reason, we filter the connectivity matrix in β frequency band band:

$$\hat{A}_{ij} = \sum_{\omega_k / T_s \in \beta} C_{ij}(\omega_k) \tag{4.23}$$

After demonstrating that the denoising based on $\mathcal{U}_{L\cup H}$ subspace allows a better separability of connectivity states under $\mathcal{H}_1$ and $\mathcal{H}_0$, we limit the analysis to $\mathcal{U}_{L\cup H}$ and $\mathcal{U}_{ALL}$.

We compute the scores as explained in section 4.5A) and we report the associated results in Fig. 4.9. In the first row, we collect the results referring to extra

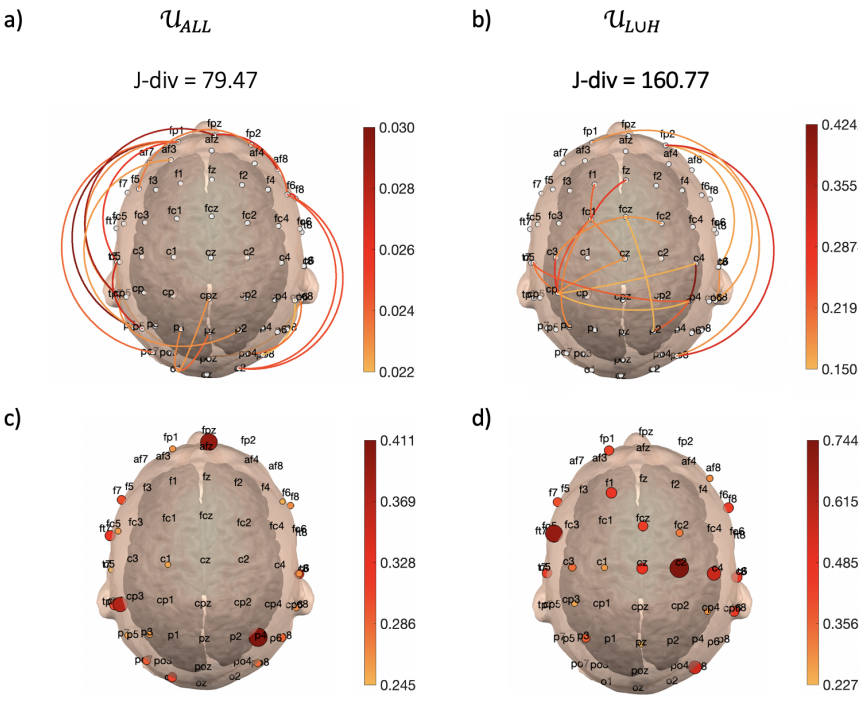

Figure 4.9: Results of score computation for real EEG data. All the eigenvectors are considered (i.e. $\mathcal{U}_{ALL}$) in panels a,c);and results associated to the proposed denoising algorithm (ie. $\mathcal{U}_{L\cup H}$) in panels b,d). In the first line, score values refer to links (i.e. extra-diagonal elements) and in the second line, they refer to elements in the principal diagonal (i.e. nodes). For sake of clarity, in all the figures we plot the 20 nodes or links with highest score.

diagonal elements of $\tilde{L}$, i.e. links, and in the second row, we have results associated to diagonal elements, i.e. node strength values. Besides, on the left and right

columns we report scores obtained without and with application of the proposed Laplacian denoising.

The first interesting result is that, even in the case of connectivity matrix restricted to β band, the proposed denoising improves the J-divergence of the two connectivity states (from 79.47 to 160.77).

Considering results from score analysis, different observations are in order.

In Fig. 4.9(a-b) the score associated to links' weigths (Laplacian extra- diagonal elements) is reported. If we observe results without denoising, it appears difficult to identify the contributions of different brain areas because the links' weights are generally low (between 0 and 0.035). The 20 links associated to highest score do not involve sensory-motor nodes. On the contrary, links' scores achieve higher values (0.42) in $\mathcal{U}_{L\cup H}$ case. Interestingly, the strongest links are located in sensory-motor areas, and links connecting contra-lateral motor areas, such as $CP_3 - C_3$ rank highest.

We focus on the score related to nodes weights (Laplacian diagonal elements) in Fig. 4.9(c-d). Firstly, the score range in absence of denoising is smaller compared to when the Laplacian denoising is applied, i.e. maximum values are 0.4 and 0.7. Then, the scores obtained without denoising are larger on nodes located in frontal, temporal or parietal area, such as FP_Z and P_4. After denoising, the score values are higher on sensory-motor areas, and we can recognize some more relevant nodes, such as C_2 and FC_5.

Thereby, the proposed score procedure together with the Laplacian denoising provides an original tool for the analysis and the interpretation of the brain cognitive states.

4.7.4 Short-time estimation of Laplacian coefficients in β band

BCI systems aim to realize a real time communication between the user and the interface [208, 210]; thereby, decreasing the observation time T_{oss} for Laplacian computation is beneficial for potential applicability to online motor-imagery BCI. In this direction, we test the Laplacian denoising when the window length of the observed signals is reduced to $T_{oss} = 1s$. For this analysis, we consider a moving window of length $T_{oss} = 1s$ and we shift it by $m\Delta t, m = 0 \cdots M-1$, with $M = 9$ $\Delta t = 0.5$s, in order to analyse the total available length of 5s over nine 50% overlapping temporal windows. [177].

In order to obtain a global information across the subjects, we take into consideration the 20 subjects of the experimental study. For each subject, we compute the spectral coherence on the m-th temporal interval, $m = 0 \cdots M-1$ as in Eq. (5.11) both for resting ($\mathcal{H}_1$) and motor imagery ($\mathcal{H}_0$) state. Then we compute the

conditional ($\mathcal{H}_1$, $\mathcal{H}_0$) estimated adjacency matrix $\hat{A}$ as in Eq.(5.12), the estimated graph laplacian $\hat{L}$ as in Eq. (4.4), and its denoised version $\tilde{L}$ as in Eq.(4.8). Then, we evaluate the J-divergence between the two hypotheses as in Eq. (4.16). Finally, we average the J obtained on the m-th window $m = 0 \cdots M-1$ in each time-interval across subjects. For comparison's sake, we repeat the above computations in absence of denoising (i.e. with $\mathcal{U}_{ALL}$ subspace).

Fig. 4.10 shows associated results by plotting the J-divergence, averaged across subject, as a function of the time window index m, $m = 0 \cdots M-1$. Our findings show that for almost all the time intervals m, i.e. on 7 intervals out of 9, the denoising algorithm leads to higher J-divergence compared to the absence of denoising. This result is really interesting because it shows that, even with short time-interval, our method succeeds in separating the two cognitive states.

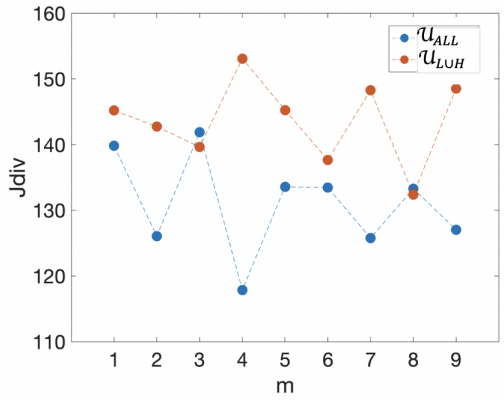

Figure 4.10: Results of J-divergence analysis over a moving window on real data. We plot the J-divergence over $M = 9$, 1s long, time intervals with 50% overlapping, versus the time interval index. The J-divergence is computed in β band and averaged across subjects.

Our findings on real EEG data show that the proposed Laplacian denoising applies also on short time-windows and improves the detectability of motor imagery states.

4.8 On the applicability in BCI systems: classification framework

In this chapter, we propose a denoising algorithm able to improve the connectivity state separability. In order to quantify class separability, we use the J-divergence, which has been defined in a transformed space, where observations under $\mathcal{H}_0$ are whitened and those under $\mathcal{H}_1$ are uncorrelated.We show an improvement of the

distance between two connectivity states in terms of J-divergence when the Laplacian denoising algorithm is applied on original data. In order to appreciate the potential of denoising in machine learning application, we present here an off-line classification scenario on one subject. This analysis is an proof-of-concept and other studies are needed to validate the off-line classification framework, schematically presented in Fig. 4.11.

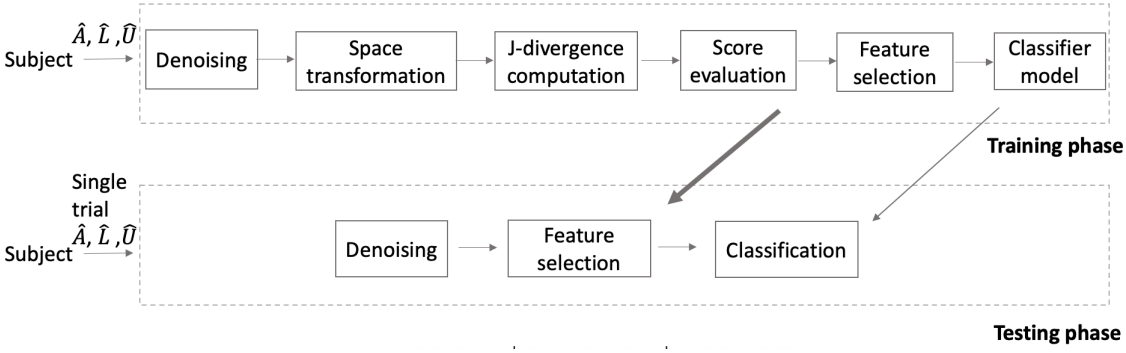

Figure 4.11: Procedure for classification with denoised data. The score computation is used to select features from training data to perform the classification in the testing phase. This scheme represent one fold and one repetition. In our classification, we perform a 10-repeated 10 fold LDA classification.

We perform a 10 repeated 10-fold cross-validation classification with linear discriminant analysis (LDA) [106, 107]. For each repetition, we firstly consider the training set and we perform the Laplacian denoising. Then, we compute the matrix T to transform original data in the transformed domain. Here, we evaluate the J-divergence and the score, which identifies the variables in the original space which mostly contributed to the state separability. The variables selected by the score procedure are used to select features in the testing set. In fact, variables in the testing set are firstly filtered with Laplacian denoising. Then, the first $\bar{N}$ variables selected according to the score procedure in the training set, are used for the classification. In this framework, the feature selection is performed thought the score computation.

For sake of simplicity, we perform this analysis in frequency bands (i.e. alpha (α) and beta (β)), and we report the results in terms of classification accuracy in Table 4.4. Our findings show a slight improvement of the accuracy, both in α and β bands when Laplacian denoising is applied (i.e. from 0.60 to 0.63 in β and from 0.57 to 0.67 in α).

This result reinforces the potential of the proposed algorithm to increase the detectability of connectivity states, albeit more studies will be needed to confirm the ability to discriminate mental states in practical BCI applications.

	$\mathcal{U}_{L\cup H}$	$\mathcal{U}_{ALL}$
β	**0.63**	0.60
α	**0.67**	0.57

Table 4.4: Accuracy values for 10-repeated 10 fold classification. We report results in absence of denoising ($\mathcal{U}_{ALL}$), and with our Laplacian denoising algorithm ($\mathcal{U}_{L\cup H}$).

From a theoretical perspective, a strong hypothesis that underlies the analysis is that the data are normally distributed. In principle, we obtain an improvement in the separation under this hypothesis, but if data are not Gaussian, the separability under the two hypothesis depends on their probability density function (PDF) [1]. Results of distance between connectivity states directly depend on the observed statistics, which change across subjects, across frequency bands, across time intervals. For each subject, we can derive a set of parameters (i.e. frequency bin, set of EEG channels, number of eigenvectors to eliminate) in which the Laplacian denoising is adapted and it can provide an improvement in the separability of connectivity states.

In this direction, we are currently implementing this framework (as in Chapter 6) in Openvibe [159], which is a software specifically designed for real-time BCI. It is generally used to visualize and process brain data. The development of a real BCI based on denoised connectivity features enables to adapt all the parameters in the training phase of the experiment. Then, during the testing, the classification can be performed with the parameters optimized for the specific case.

4.9 Conclusion and further work

In this chapter, we proposed a Laplacian denoising algorithm for the purpose of connectivity states detection. A novel formulation of the Jensen divergence has been derived to measure the performance of the denoising algorithm, as well as to attribute a score to the Laplacian coefficients. The Laplacian denoising performances are assessed by numerical simulations on synthetic data. Furthermore, the Laplacian denoising algorithm has been applied to real EEG data recorded during motor imagery BCI experiments. Our results show that the proposed denoising strategy improves the separation of the two cognitive states of motor imagery and resting, even under short time intervals. In addition, the J-divergence based scoring highlights the contribution of Laplacian coefficients to the separability between two cognitive states. A critical aspect in the actual implementation of our frame-

work will be the choice of parameters, such as the number of eigenvectors in each subspace or the frequency band of interest. One possibility to identify adapted parameters, consists in defining them for each specific subjects during the BCI training. Taken together, the proposed approach is promising for the robust detection of connectivity states while being appealing for application in real-time BCI systems.

Appendix E: Theorem 1

Let us consider the problem of binary classification of Gaussian variables $\mathcal{H}_0 : \mathbf{x} \sim \mathcal{N}(\mathbf{0}, \mathbf{I})$, $\mathcal{H}_1 : \mathbf{x} \sim \mathcal{N}\left(\boldsymbol{\eta}, \boldsymbol{\Sigma}^2\right)$, corresponding to the uncommon mean, uncommon covariance case, by means of the LLRT formulation in Eq.(4.12). By simple algebraic manipulation, we recognize that the test $\mathcal{R}(\mathbf{x}) \underset{\mathcal{H}_0}{\overset{\mathcal{H}_1}{\gtrless}} t'$ corresponds to:

$$\mathcal{R}'(\mathbf{x}) = \underbrace{\sum_{n=1}^{P} \frac{\sigma_n^2 - 1}{\sigma_n^2} \left| x_n + \frac{\eta_n}{\sigma_n^2 - 1} \right|^2}_{P \text{ quadratic terms}} + \underbrace{\sum_{n=P+1}^{N'} 2\eta_n \cdot x_n}_{N'-P \text{ linear terms}} \underset{\mathcal{H}_0}{\overset{\mathcal{H}_1}{\gtrless}} t'' \tag{4.24}$$

with $t'' = t' + \sum_{n=1}^{P} |\eta_n^2| \left[\sigma_n^2 \left(\sigma_n^2 - 1\right)\right]^{-1}$.

Let us consider the linear-quadratic observation space Ξ of the N-dimensional random vector $\boldsymbol{\xi} \overset{\text{def}}{=} [\xi_1 \dots \xi'_N]^{\mathrm{T}}$ defined as (see Eq. (4.15))

$$\begin{aligned} \xi_n &= \left(x_n + \frac{\eta_n}{\sigma_n^2 - 1} \right)^2 \\ &= x_n^2 + 2\, x_n \ \frac{\eta_n}{\sigma_n^2 - 1} + \left(\frac{\eta_n}{\sigma_n^2 - 1} \right)^2 ; n = 1, \dots, P \\ \xi_n &= x_n, \ n = P+1, \dots, N' \end{aligned} \tag{4.25}$$

In the space Ξ the LLRT $\mathcal{R}'(\mathbf{x}) \underset{\mathcal{H}_0}{\overset{\mathcal{H}_1}{\gtrless}} t''$ rewrites as follows:

$$\sum_{0}^{N-1} a_{\mathrm{LLR},n} \xi_n = \mathbf{a}_{\mathrm{LLR}}^{\mathrm{H}} \cdot \boldsymbol{\xi} \underset{\mathcal{H}_0}{\overset{\mathcal{H}_1}{\gtrless}} t'' \tag{4.26}$$

where the elements of $\mathbf{a}_{\mathrm{LLR}} \stackrel{\mathrm{def}}{=} [a_{\mathrm{LLR},1}, \ldots, a_{\mathrm{LLR},N'}]^{\mathrm{T}}$ are:

$$a_{\mathrm{LLR},n} \stackrel{\mathrm{def}}{=} \begin{cases} \dfrac{\sigma_n - \sigma_n^{-1}}{\sigma_n} & \text{for } n = 1, P \\ 2\eta_n & \text{for } n = P+1, N' \end{cases} \tag{4.27}$$

With these positions,

$$\begin{aligned} J &\stackrel{\mathrm{def}}{=} \mathbb{E}\left(\mathcal{R}(\mathbf{x})|\mathcal{H}_1\right) - \mathbb{E}\left(\mathcal{R}(\mathbf{x})|\mathcal{H}_0\right) \\ &= \mathbb{E}\left(\mathcal{R}'(\mathbf{x})|\mathcal{H}_1\right) - \mathbb{E}\left(\mathcal{R}'(\mathbf{x})|\mathcal{H}_0\right) \\ &= \sum_{n=0}^{N-1} a_{\mathrm{LLR},n}\left(\mathbb{E}\left(\xi_n|\mathcal{H}_1\right) - \mathbb{E}\left(\xi_n|\mathcal{H}_0\right)\right) \end{aligned} \tag{4.28}$$

By computing the above expectations it can be straightforwardly shown that the n-th term $a_{\mathrm{LLR},n}\left(\mathbb{E}\left(\xi_n|\mathcal{H}_1\right) - \mathbb{E}\left(\xi_n|\mathcal{H}_0\right)\right)$ of the above sum equals to

$$\begin{aligned} J_n{}^{(\sigma_n,\eta_n)} &= \frac{\sigma_n - \sigma_n^{-1}}{\sigma_n}\left(\sigma_n^2 + \eta_n^2 + 2\frac{\eta_n^2}{\sigma_n^2 - 1} - 1\right) \\ &= \left(\sigma_n - \sigma_n^{-1}\right)\left[\left(\sigma_n - \sigma_n^{-1}\right) + \frac{\eta_n^2}{\sigma_n}\frac{\sigma_n^2 + 1}{\sigma_n^2 - 1}\right] \\ &= \left(\sigma_n - \sigma_n^{-1}\right)^2\left[1 + \frac{\eta_n^2}{\sigma_n}\frac{\sigma_n^2 + 1}{\left(\sigma_n - \sigma_n^{-1}\right)\left(\sigma_n^2 - 1\right)}\right] \\ &= \left(\sigma_n - \sigma_n^{-1}\right)^2\left[1 + \frac{\eta_n^2}{\sigma_n}\frac{\sigma_n + \sigma_n^{-1}}{\left(\sigma_n - \sigma_n^{-1}\right)^2}\right], n = 1, \cdots P \\ J_n{}^{(\eta_n)} &= 2\eta_n^2,\ n = P, \cdots N-1. \end{aligned} \tag{4.29}$$

and

$$J_n^{(\eta_n)} = 2\eta_n^2,\ n = P, \cdots N-1. \tag{4.30}$$

QED.

Chapter 5

Framework for short-time graph connectivity estimation

Brain signals are time-varying and non-stationary, which means that the dynamic of the signals and their moments change over time. The development of a robust tool to estimate graph functional connectivity is crucial for BCI applications. L1-Principal Component Analysis (L1-PCA) is a state-of-the-art computational tool able to identify relevant components in data with noise and outliers. Significant efforts have been made in the direction of adapting the PCA to time-varying data. Here, we analyse a layered version of L1-PCA, which we refer to as Deep L1-PCA. Deep L1-PCA is obtained by recursive application of two steps: estimation of L1-PCA basis and extraction of the first rank projector. Deep L1-PCA is robust to outliers and it produces relevant components with a reduced computational cost. Here, we show how the Deep L1-PCA can be applied in a classification scheme of time-varying data. This framework is preliminarily applied to simulated graphs and then to EEG data recorded during motor imagery-based BCI experiments. The proposed approach shows potential in the application of real BCI systems for short-time connectivity estimation and discrimination of brain states.

This chapter contains part of the work from Orru, G., Cattai, T., Colonnese, S., Scarano, G., De Vico Fallani, F., Markopoulos, P., and Pados, D. (2019, September). Deep L1-PCA of Time-Variant Data with Application to Brain Connectivity Measurements. In 2019 27th European Signal Processing Conference (EUSIPCO) (pp. $1-5$*). IEEE. [134]*

5.1 Introduction

Brain signals are time-varying and non-stationary: the dynamic of the signals and their moments change over time [24, 36, 172]. The development of a robust tool to estimate graph functional connectivity is crucial for BCI applications, where a short-time feature extraction is needed to realize a real-time interaction between user and machine [209]. L1-Principal Component Analysis (L1-PCA) is a state-of-the-art computational tool able to extract relevant components from data with noise and outliers [114]. The idea of applying L1-PCA to capture the evolution of time-varying data has already been explored, for instance to track time-varying L1-PCA components [112]. A moving window is usually applied for tracking and it gains in computational cost because only the innovation components are computed at each new time interval. The disadvantage is that this method requires a preliminary selection of the window length, which is defined according to the time duration of the dynamic evolution to be analysed. Another possibility consists in applying a novel hierarchical approach, referred to as Deep L1-PCA. A deep computational architecture has already been investigated to extract Euclidean norm PCA in the context of face recognition in [104], even though the impact of layering parameters was not discussed. Our Deep L1-PCA algorithm is composed by the sequence of two recursive steps: data partitioning and L1-PCA analysis with first rank component extraction.

In this chapter, we firstly describe the mathematical formulation of the Deep L1-PCA method and its advantages in minimizing the effect of perturbations with decreasing computational cost. This approach is applied here to obtain an estimation of graph connectivity in short-time windows and to define a classification scheme to discriminate two connectivity states.

For sake of clarity, we report in Table 5.1 the list of the main notation used in this chapter.

5.2 Deep L1-PCA computational framework

Before detailing the mathematical formulation, a presentation of the key idea of the Deep L1-PCA is needed. At the first layer, the original data are partitioned, and for each partition the L1-Principal Component (L1-PC) is estimated. The principal components (L1-PCs) of all partitions are then organized to build a new group, which becomes the input of the second layer. The procedure at the second layer naturally follows: the input data are partitioned in subgroups and the L1-PCs extracted for each subgroup become the input for the next layer. This iterative

Notation	Description
Ξ	original data matrix
K	number of layers
M_K	number of batches at layer k
W_K	batch size at layer k
$\mathbf{R}_k$ ($\mathbf{r}_k$)	$L1-PC$ matrix (or vector) at layer k
$\mathbf{B}_k$ ($\mathbf{b}_k$)	optimal binary matrix (or vector) at layer k
$\hat{\mathbf{A}}$	estimated adjacency matrix)
$\hat{\mathbf{L}}$	estimated Laplacian matrix)
$\hat{\mathbf{D}}$	estimated degree matrix)

Table 5.1: Table of main notation in Chapter 5.

procedure can be repeated as many times as necessary to end up, eventually, with only one principal component, which we refer to as global L1-PC. For sake of clarity, we remark that from the second layer on, the input data are the unit-norm L1-PCs computed in the previous layer. It means that the input data at each layer after the first computation differ in nature and range from the original data. The Deep L1-PCA architecture is illustrated in Fig. 5.1, where the original input data are bidimensional series.

In the general case, input data are M samples of D-dimensional vectors, collected in the data matrix $\Xi = [\xi_1, \xi_2, \ldots, \xi_m \ldots, \xi_M] \in \mathbb{R}^{D \times M}$.

The input data in the k-th layer are grouped to create M_k size-W_k batches

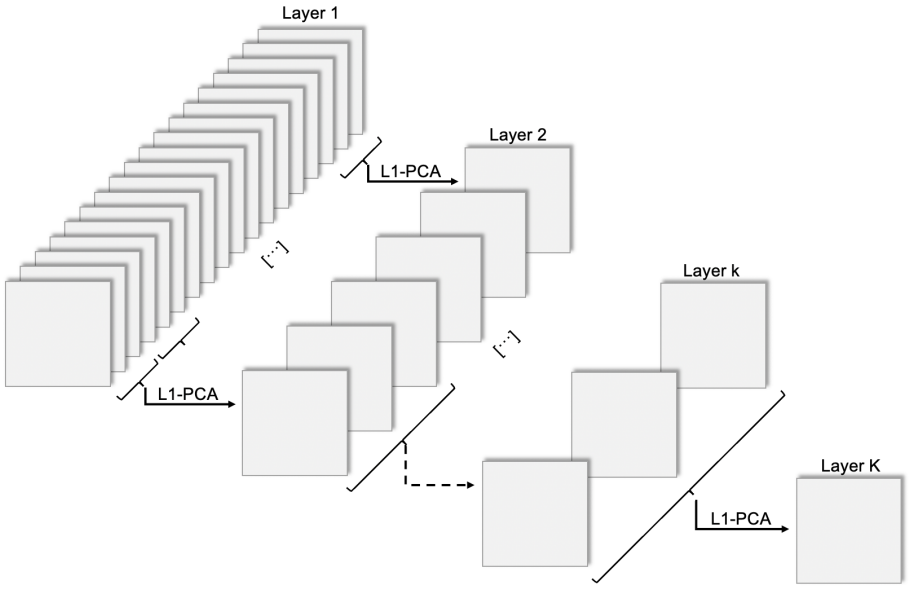

Figure 5.1: General Deep L1-PCA computation structure.

$\mathbf{R}_k(m), \quad m = 1, \ldots, M_k$. For the particular case of $k = 1$, the m-th batch $\mathbf{R}_1(m)$ contains the original data. In the case of $k > 1$, the generic batch $\mathbf{R}_k(m)$ contains the M_{k-1} principal components computed at the previous layer.

The computational procedure continues with the L1-PCA in the m-th batch, denoted as $\mathbf{R}_k(m)$ and the L1-PC $\mathbf{r}_k(m)$, $m = 1, \ldots, M_k$, is extracted as in (5.1).

Following this iterative procedure, data at each layer are progressively reduced by replacing each batch with the associated principal component. For the M_k batches at each layer k, it holds $M_k = M \cdot \prod_{j=1}^{k} \frac{1}{W_j}$.

We assume that iterative partitions of the data lead to a single global component, i.e. $M = \prod_{k=1}^{K} W_k$. This hypothesis is necessary because in some cases, the size M of the original dataset cannot be divided by the chosen W_k obtaining equal batches. As consequence, a number of elements $W_k - 1$ have to be separately analysed in some manner.

At the m-th batch and k-th layer, the L1-PC is computed using the fast estimator introduced by Markopoulos et al. [113]:

$$\mathbf{r}_k(m) = \mathbf{R}_k(m)\mathbf{b}_k(m) \cdot \Delta_k(m) \tag{5.1}$$

$\mathbf{b}_k(m)$ is the optimal binary vector, computed as:

$$\underset{b \in \{\pm 1\}^{W_k}}{\arg\max} \|\mathbf{R}_k(m)\mathbf{b}\|_2 \tag{5.2}$$

and $\Delta_k(m)$ comes from the equation that follows:

$$\Delta_k(m) = \frac{1}{\|\mathbf{R}_k(m)\mathbf{b}_k(m)\|_2} \tag{5.3}$$

As from the equations (5.1) and (5.3) , the $\mathbf{r}_k(m)$ is a normalized version of $\mathbf{R}_k(m)$ $\mathbf{b}_k(m)$.

These operations provide a set of M_k principal components, where each of them is the first L1-PC related to one batch m_k. The iterative repetition of this procedure finally reaches the last layer K.

The Deep L1-PCA can be written in a compact manner using the Khatri-Rao product *

To this aim, we define the matrices:
$\mathbf{B}_k = [\mathbf{b}_{k-1}(1),\ \mathbf{b}_{k-1}(2),\ \ldots,\ \mathbf{b}_{k-1}(m),\ \ldots,\ \mathbf{b}_{k-1}(M_{k-1})] \in \{\pm 1\}^{W_{k-1} \times M_{k-1}}$ which contains the optimal binary vectors $\mathbf{b}_{k-1}(m) \in \mathbb{R}^{W_k - 1}$

*The Khatri-Rao product of matrices $\mathbf{F} \in \mathbb{R}^{C \times E}$ and $\mathbf{G} \in \mathbb{R}^{D \times E}$ is written as $\mathbf{F} \odot \mathbf{G} = (F_1 \otimes G_1, \ldots, F_E \otimes G_E)$, where $\otimes$ is the Kronecker product [96], [42].

$\mathbf{R}_k = [\mathbf{r}_{k-1}(1),\ \mathbf{r}_{k-1}(2),\ \ldots,\ \mathbf{r}_{k-1}(m),\ \ldots,\ \mathbf{r}_{k-1}(M_{k-1})] \in \mathbb{R}^{D \times M_{k-1}}$ which collects the M_{k-1} L1-PCs computed in $k-1$ for $k > 1$ and for $k = 1$ it contains the original data $\mathbf{R}_1 = \Xi$
$\mathbf{\Delta}_k = \text{diag}([\Delta_{k-1}(1), \Delta_{k-1}(2), \ldots, \Delta_{k-1}(M_{k-1})])$
Applying the Khatri-Rao product to $\mathbf{B}_k \in \mathbb{R}^{W_{k-1} \times M_{k-1}}$, we derive

$$\mathbf{I}_{M_{k-1}} \odot \mathbf{B}_k = \begin{bmatrix} \mathbf{b}_{k-1}(1) & \mathbf{0}_{W_{k-1}} & \ldots & \mathbf{0}_{W_{k-1}} \\ \mathbf{0}_{W_{k-1}} & \mathbf{b}_{k-1}(2) & \ldots & \mathbf{0}_{W_{k-1}} \\ \vdots & \vdots & \ddots & \vdots \\ \mathbf{0}_{W_{k-1}} & \mathbf{0}_{W_{k-1}} & \ldots & \mathbf{b}_{k-1}(M_{k-1}) \end{bmatrix}$$

We write the whole set of projectors at the first layer as follows:

$$\begin{aligned} \mathbf{R}_2 &= [r_1(1), \ldots, r_1(M_1)] \\ &= [\mathbf{R}_1(1), \ldots, \mathbf{R}_1(M_1)] \cdot (\mathbf{I}_{M_1 \times M_1} \odot \mathbf{B}_2) \cdot \mathbf{\Delta}_2 \\ &= \Xi \cdot (\mathbf{I}_{M_1 \times M_1} \odot \mathbf{B}_2) \cdot \mathbf{\Delta}_2 \\ \mathbf{R}_{2_{D \times M_1}} &= \Xi_{D \times M} \Big(\underbrace{\mathbf{I}_{M_1 \times M_1} \odot \mathbf{B}_{2_{W_1 \times M_1}}}_{M_1 \cdot W_1 \times M_1 = M \times M_1} \Big) \cdot \mathbf{\Delta}_{2_{M_1 \times M_1}} \end{aligned} \tag{5.4}$$

and, for the other $k = 2, 3, \ldots, K$ layers:

$$\mathbf{R}_k = \mathbf{R}_{k-1} \cdot (\mathbf{I}_{N_{k-1}} \odot \mathbf{B}_k) \cdot \mathbf{\Delta}_k \qquad \in \mathbb{R}^{D \times W_{k-1}} \tag{5.5}$$

We can write $\mathbf{R}_k$ as:

$$\begin{aligned} \mathbf{R}_k &= \Xi \cdot (\mathbf{I}_{M_1 \times M_1} \odot \mathbf{B}_2) \cdot \mathbf{\Delta}_2 \cdot \ldots \cdot (\mathbf{I}_{M_{k-1} \times M_{k-1}} \odot \mathbf{B}_k) \cdot \mathbf{\Delta}_k \\ &= \Xi \cdot \prod_{j=2}^{k} [(\mathbf{I}_{M_{j-1} \times M_{j-1}} \odot \mathbf{B}_j) \cdot \mathbf{\Delta}_j] \end{aligned} \tag{5.6}$$

At the final layer K, the global principal component can be computed:

$$\mathbf{r}_K = \mathbf{R}_K \cdot (\mathbf{I}_{M_K \times M_K} \odot \mathbf{B}_{K+1}) \cdot \mathbf{\Delta}_{K+1} \tag{5.7}$$

where $M_K = 1$, $\mathbf{B}_{K+1} = \mathbf{b}_K(1) \in \{\pm 1\}^{M_{K-1} \times 1}$ and $\mathbf{\Delta}_{K+1} = \Delta_K(1) \in \mathbb{R}^+$.

Some considerations are in order: i) L1-PCA differs from the overall L1-PCA computed on the whole original data; ii) Deep L1-PCA intrinsically has an additional information, which is the relative distance of L1-PCA solutions computed at the intermediate layers.

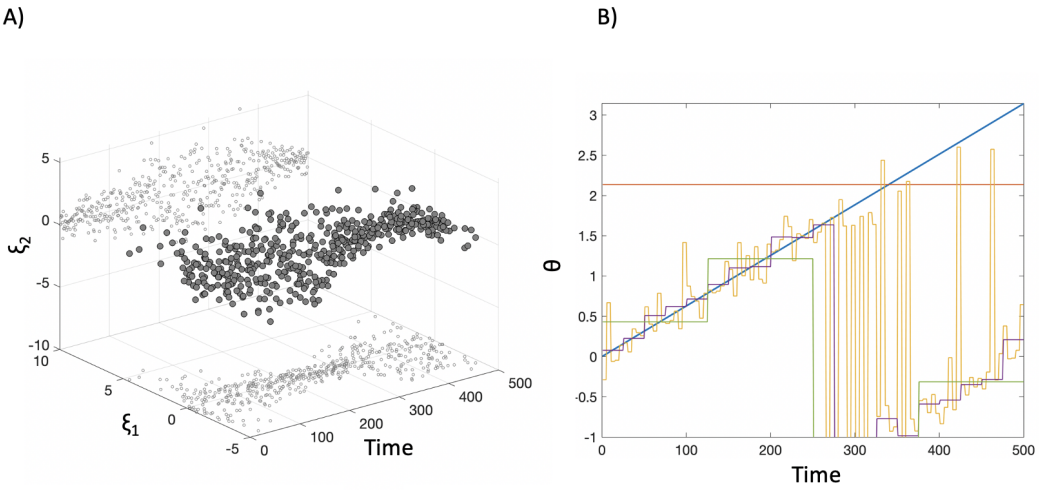

Figure 5.2: A) Time-variant bidimensional normal data and in B) the underlying probability density function (PDF) orientation.

One example of Deep L1-PCA is presented in Fig. 5.2, where we have 500 samples $\Xi = [\xi_1, \cdots, \xi_{500}]$ from a zero-mean bivariate normal distribution with marginal variances $1/4, 4$, whose principal axis rotates according to a linear $\theta(t)$ represented in Fig. 5.2, (blue line).

The original data Ξ are partitioned in batches to compute the L1-PCA basis vectors, represented with red arrows in Fig. 5.3 A). In Fig. 5.3 B,C) we report the other layers for $k = 2$ and layer $k = 3$.

5.3 Application to graph synthetic data

In this section, we test the ability of the Deep L1-PCA to characterize two estimated graph Laplacian matrices, related to two connectivity states.

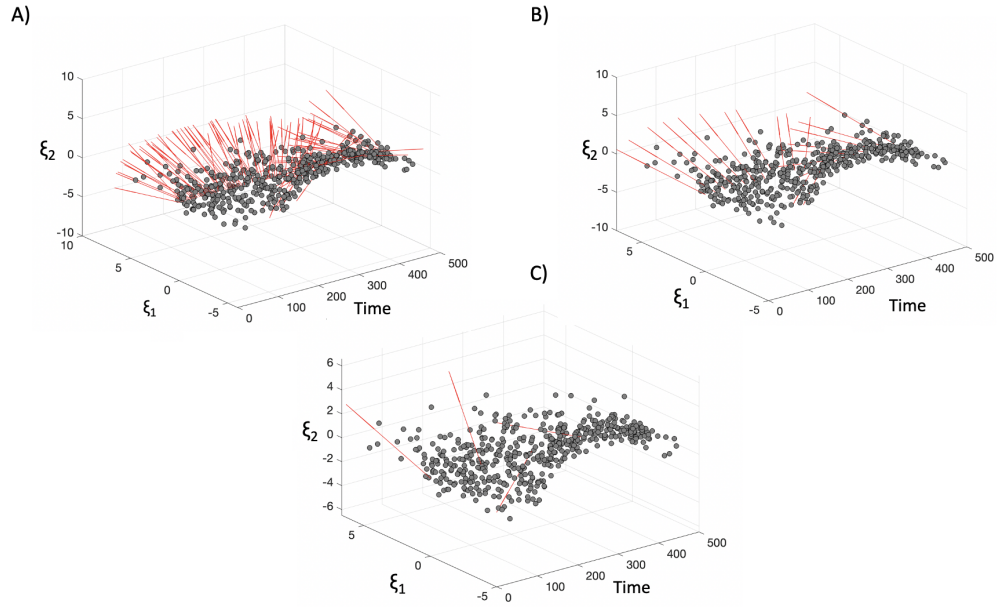

Figure 5.3: Time-variant data and first order L1-PCA approximation at different layers : layer 1 in A), layer 2 in B) and layer 3 in C).

To this aim, we firstly consider two graphs with the same nodes but different links' weights, to obtain two different connectivity matrices. This configuration models two functional connectivity matrices extracted by EEG signals. Real EEG signals will be used in the next section.

We test our approach measuring the mean-square error (MSE) -to quantify the robustness of the procedure- and implementing a classification scheme -to verify the ability of the L1-PCs to discriminate two connectivity states.

5.3.1 Connectivity matrices simulation

In order to validate our method on synthetic data, we define two adjacency matrices under the two hypotheses $\mathcal{H}_0$ and $\mathcal{H}_1$.

Under $\mathcal{H}_1$, we define an adjacency matrix characterized by all zero connections, except for H_c connections set at 1, to simulate strong links. A noise component is added to the adjacency matrix in order to simulate perturbations. Under $\mathcal{H}_0$, $H_c = 0$ (i.e. there are not strong connections) and there is only a noise contribution. We can write the estimated adjacency matrix $\hat{\mathbf{A}}(m)$ for each observation m as the sum of the real adjacency matrix $\mathbf{A}(m)$ and the noise contribution $\mathbf{w}(m)$:

$$\begin{aligned} \mathcal{H}_1 &: \hat{\mathbf{A}}(m) = \mathbf{A}^{(1)}(m) + \mathbf{w}(m) \\ \mathcal{H}_0 &: \hat{\mathbf{A}}(m) = \mathbf{A}^{(0)}(m) + \mathbf{w}(m) \end{aligned} \tag{5.8}$$

where $\mathbf{w}$ is the noise, which is a realization of a discrete, stationary, white Gaussian process, with $E\{\mathbf{w}\} = 0,\ E\{\mathbf{w}\mathbf{w}^T\} = \sigma_w^2 I\ \forall k$; $\mathbf{A}^{(0)}$ is a zero matrix; $\mathbf{A}^{(1)}$ is a zero-matrix containing ones for $h_C = 0, \cdots H_C - 1$ elements. Once obtained the synthetic adjacency matrices, we can derive the estimated Laplacians:

$$\hat{\boldsymbol{L}}(m) = \hat{\boldsymbol{D}}(m) - \hat{\boldsymbol{A}}(m) \tag{5.9}$$

where $\hat{\mathbf{D}}$ is the estimated degree matrix, whose generic diagonal element d_i is equal to the sum of the weights of all the edges incident to the node i. For each observation, and under each hypothesis, we derive the Laplacian matrix $\hat{\boldsymbol{L}}(m)$.

For the following analysis on those synthetic data, we consider $M = 8$ observations and $\sigma_w = 0.6$.

5.3.2 Robustness analysis via MSE

In the following, we will verify the robustness of the Deep L1-PCA. In order to do so, we will compute for each layer k and each observation m, the mean squared error between PCs obtained with synthetic data generated under two conditions : (1), the presence of noise; (1)REF, the reference case without perturbations.

Specifically, we consider the data matrices at each m observation $\xi_m^{(1)} = \hat{\mathbf{D}}^{(\mathbf{1})}(m)$ and $\xi_m^{(1)REF} = \hat{\mathbf{D}}^{(\mathbf{1})\mathbf{REF}}(m)$, where $\hat{\mathbf{D}}^{(\mathbf{1})}(m)$ is the degree matrix computed from $\hat{\mathbf{A}}^{(\mathbf{1})}(m)$ and $\hat{\mathbf{D}}^{(\mathbf{1})\mathbf{REF}}(m)$ is obtained from $\mathbf{A}^{(\mathbf{1})}$. We collect M= 8 degree matrices for each condition.

Following the procedure described in section 5.2, we perform two Deep L1-PC analyses with $W_K = 2$ and $M_k = 1$, for $k = 1$, and we obtain: $i)$ $\mathbf{R}_k^{(\mathbf{1})\mathbf{REF}}$ from $\Xi^{(1)}$ and $ii)$ $\mathbf{R}_k^{(\mathbf{1})\mathbf{REF}}$ from $\Xi^{(1)REF}$.

This procedure provides two Deep L1-PCA structures, one computed from data corrupted by noise and the other obtained from data without perturbations. For each set of original data, a general scheme of the Deep L1-PCA procedure is presented in Fig. 5.4.

After a preliminary normalization step, for each observation m and each layer k, we compute the mean squared error (MSE) as follows:

$$MSE_k(m) = min(||\mathbf{R}_k^{(\mathbf{1})\mathbf{REF}}(m) - \mathbf{R}_k^{(\mathbf{1})}(m)||^2, ||\mathbf{R}_k^{(\mathbf{1})\mathbf{REF}}(m) + \mathbf{R}_k^{(\mathbf{1})}(m)||^2) \tag{5.10}$$

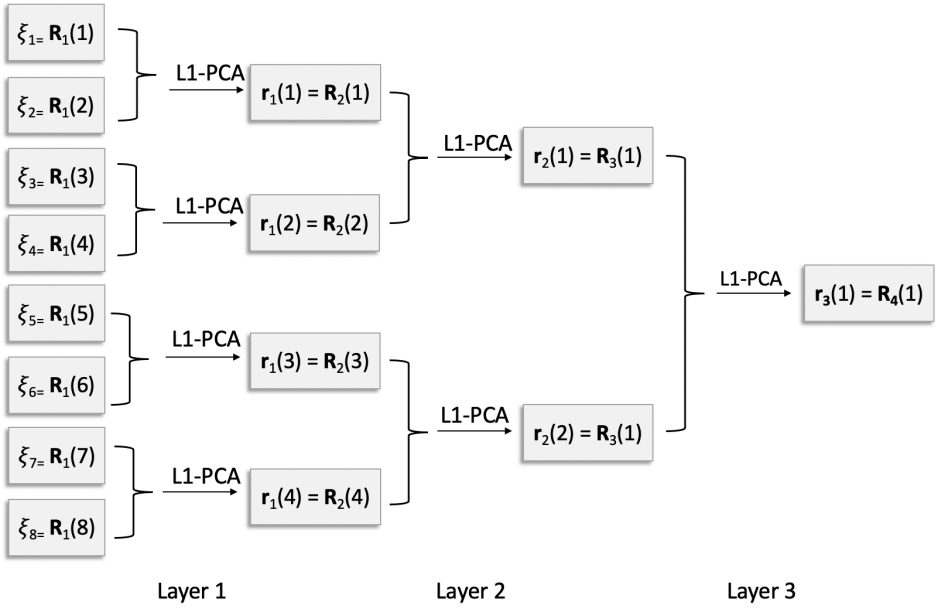

Figure 5.4: Graphical representation of Deep L1-PCA computation with an $M = 8$ original data Ξ. At each layer k ($k = 1, 2, 3$) the L1-PCAs $\mathbf{r}_k(m)$ are computed and they become the input in $\mathbf{R}_{k+1}(m)$ for the next layer.

Let us remark that the definition of the MSE is expressed as in (5.10) (i.e. with the alternative on the sign of the PC estimates) because the direction of principal components is not uniquely defined through the procedure in [114].

Results of the MSE computation are in Fig. 5.5, where MSE values are reported for each layer k and each observation m in a color scale. Our findings show that MSE values generally decrease by considering higher layers 19 to 9. This results is perfectly in line with a previous analysis in [134].

Since MSE values are computed between PCs obtained on noisy data with respect to those in absence of perturbations, results demonstrate that the impact of noise generally decreases in higher layers.

5.3.3 Classification framework

Here, we investigate the possibility to apply the Deep L1-PCA to obtain robust features to detect two connectivity states corresponding to $\mathcal{H}_1$ and $\mathcal{H}_0$.

In order to perform a classification procedure, we synthetically produce N_T repetitions, or trials, to obtain N_T adjacency matrices for $m = 1, .., M$ under each condition. In this manner, for each condition, we collect N_T trials for the M adjacency matrices to allows a classification analysis for each layer k and each observation m.

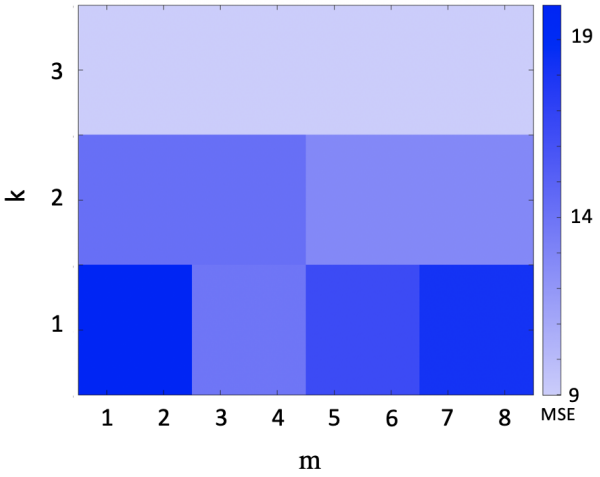

Figure 5.5: Mean squared error map computed on simulated data between the degree matrix corrupted by noise with $\sigma_w = 0.6$ and its reference version (i.e. without perturbations).

After matrices' generation, we follow the procedure presented in section 5.2 for each trial, in order to obtain for each condition a N_T-dimensional set of $\mathbf{R^{(1)}}_k$ and N_T-dimensional set of $\mathbf{R^{(0)}}_k$. $\mathbf{R^{(1)}}_k$ is the Deep L1-PCA estimation when the original data matrix corresponds to $\xi_m^{(1)} = \hat{\mathbf{D}}^{(\mathbf{1})}(m)$, with $m = 1, .., M$, while $\mathbf{R^{(0)}}_k$ is obtained when $\xi_m^{(0)} = \hat{\mathbf{D}}^{(0)}(m)$, with $m = 1, .., M$. For this analysis, we remind that $M = 8$.

In this study we perform one classification test for each observation (or batch) m and each layer k in order to quantify the discrimination power associated to each specific case. More in detail, we implement a classification using a 10 repeated 10-fold LDA classifier for each batch and each layer, with $N_T = 100$ for each connectivity state.

Results are presented in Fig. 5.6A), where we report the classification accuracy values. Interestingly, the accuracy, which randomly varies across batches of the same layer, generally increases considering higher layers (from $k = 1$ to $k = 3$). Specifically, results on the first layer oscillate around 65% while these values increase until reaching 78% in the final layer with $k = 3$.

In this first classification scenario, the feature vectors consist of the degree matrices under the two conditions. Another possibility is to build the feature vectors by means of the entire Laplacian matrices, taking into consideration both node strength and link values.

More formally, for each of the N_T trials, the $\mathbf{R^{(1)}}_k$ under $\mathcal{H}_1$ and $\mathbf{R^{0}}_k$ $\mathcal{H}_0$ are obtained from $\xi_m^{(1)} = \hat{\mathbf{L}}^{(\mathbf{1})}(m)$ and $\xi_m^{(0)} = \hat{\mathbf{L}}^{(0)}(m)$ for $m = 1, .., M$.

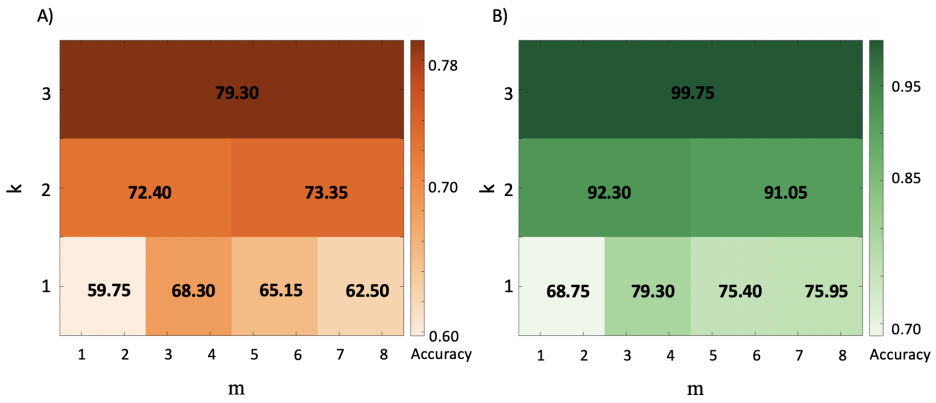

Figure 5.6: Accuracy of classification framework for synthetic data for each layer and each batch. In the rows we have the different layers and in the columns we have the batches, which are 4 at the first layer, 2 at the second and 1 batch at the final layer. In panel A), we report accuracy results when only the Laplacian diagonal elements are taken as classification features. In panel B) results are obtained when all the Laplacian elements are considered.

Fig. 5.6 B) presents associated classification results. The first consideration is that, as for Fig. 5.6 A), accuracy generally increases considering higher layers (from $k = 1$ to $k = 3$). Interestingly, batches associated to highest classification performances in Fig. 5.6 B) are the same of Fig. 5.6 A), meaning that Laplacian extra-diagonal elements do not add further information about data. Those elements fruitfully contribute to the classification since the accuracies are generally higher when all the Laplacian is considered.

For comparison's sake, we perform analogous classification tests for the 8 batches containing the original data (i.e. when no principal component analysis is applied). Results are presented in Table 5.2. The first row shows results obtained when feature vectors are built with degree matrices while the values on the second row are obtained using all the Laplacian matrices. Accuracy values obtained on the batches of original data are generally lower compared to those collected after Deep L1-PC analysis and, even in this case, Laplacian extra-diagonal elements generally improve the classification.

Our results on synthetic data show that in presence of perturbations Deep L1-PCA allows to separate graphs under two conditions. We reach this conclusion through two steps: i) a preliminary analysis of the mean squared error between a noisy graph and its ground truth counterpart to verify the robustness to noise of Deep L1-PCA; ii) a classification test to demonstrate the potential of Deep L1-PCA to separate two connectivity states.

	Time windows							
Accuracy	1	2	3	4	5	6	7	8
Laplacian diagonal elements	49.95	59.40	58.90	63.05	66.45	56.55	53.65	47.80
All Laplacian elements	58.00	60.45	67.30	62.05	58.20	69.30	62.45	62.05

Table 5.2: Classification accuracy for synthetic data related to the original $M = 8$ observations. In the first row, we have accuracies when only the Laplacian diagonal elements are taken as classification features. In the second row, accuracy values relates to when all the Laplacian elements are considered.

5.4 Results on real BCI data

In this section, we present experimental results on the application of the Deep L1-PCA framework to EEG data recorded during motor imagery experiments. Deep L1-PCA offer new tools in BCI data analysis in order to better identify mental states. For this analysis, $\mathcal{H}_1$ and $\mathcal{H}_0$ directly correspond to the hypotheses that subject performs motor imagery ($\mathcal{H}_1$) or resting state ($\mathcal{H}_0$).

5.4.1 Experimental Protocol and Preprocessing

The experimental protocol is constituted by twenty healthy subjects (aged 27.60 ± 4.01 years, 8 women), all right-handed. The study was approved by the ethical committee CPP-IDF-VI of Paris. The subjects, who did not have any physical or psychological disorder, received a financial compensation for their participation and they signed a informed consent.

During the experiments, the subject was seated in front of a screen, with a target. Specifically, when the target was up, subject has to perform a right hand motor imagery task and when it was down, he/she had to remain at rest [210] .

EEG data were recorded with a $74-$ channel system in a standard $10-10$ configuration. The sampling frequency was originally 1 kHz, and then downsampled to 250 Hz. Each subject performed several time the task, obtaining N_T trials of motor imagery and N_T trials of resting state. The trial length was 5s.

Before the following analyses, data were preliminarily preprocessed. An Independent Component Analysis (ICA) , through Infomax Algorithm [18] was performed with Fieldtrip toolbox [133] to eliminate artifacts, such as ocular and cardiac signals [54].

As a proof of concept, we only show results associated to one subject and $N_T = 74$.

5.4.2 Functional connectivity estimation procedure

In this subsection, we aim to demonstrate that the Deep L1-PCA is suitable to identify time-varying data related to two cognitive states.

The first step necessary to apply the Deep L1-PCA computation to brain EEG data consists in building the graph to finally estimate a Laplacian matrix. In this specific application, EEG data recorded at each trial directly constitute Signals on Graphs (SoGs).

In order to obtain M Laplacians for each condition, we split the total length of each trial into M time windows of length 500 ms each, obtaining 10 batches. Without loss of generality, we consider only $M_k = 8$ for $k = 1$ for sake of simplicity, but alternative strategies can be identified to manage the last 2 windows. For instance in real applications, the number of the original batches (i.e. time windows) can be tuned to not loose data and even an overlapping factor can be applied to increase the number of windows.

Once SoG samples belonging to each m window are identified, the adjacency matrices can be estimated. Among the state-of-the-art methods able to derive the estimation of the adjacency matrix, we use spectral coherence [30], which has already exhibited advantages in motor-imagery applications [31, 32]. It is computed for each pair of nodes i, j as follows, obtaining one estimate for each trial and each batch:

$$C_{ij}(\omega_k) = \frac{|\hat{P}_{ij}(\omega_k)|}{\sqrt{\hat{P}_i(\omega_k) \cdot \hat{P}_j(\omega_k)}} \tag{5.11}$$

In Eq. (5.11), $\hat{P}_i(\omega_k)$, $\hat{P}_j(\omega_k)$ and $\hat{P}_{ij}(\omega_k)$ are the estimated auto-spectra and cross-spectrum of the signals at the nodes i and j, computed using Welch method at the frequency bin $\omega_k = \frac{2\pi}{N_s}k$.

In order to derive the adjacency matrix it is possible to average $C_{ij}(\omega_k)$ across all the N_S frequency bins or to consider only some bins of interest depending on the application. Our strategy is to perform the analysis in precise frequency bands. Regarding the choice of the appropriate frequency band of interest, we underline that the brain activity in response to motor tasks varies in the frequencies and it is generally more evident in in α (8-13 Hz) or β (14-29 Hz) bands depending on the subject and on the task [117].

Here, we perform the analysis in β band, knowing that in a real BCI scenario,

the frequency band or the frequency bin of interest can be tuned during the calibration phase according to the subject characteristics. We compute the adjacency matrix by filtering the connectivity matrix in the selected frequency band:

$$\hat{A}_{ij}(m) = \sum_{\omega_k / T_s \in \beta} C_{ij}(\omega_k) \tag{5.12}$$

After the computation of the adjacency matrix for each trial and each time window, we estimate the Laplacian matrices $\hat{\mathbf{L}}$ as in (5.9) for motor imagery ($\mathcal{H}_1$) and for resting state ($\mathcal{H}_1$). The Deep L1-PCA structure can be computed as in sect.5.2, obtaining N_T repetitions of $\mathbf{R}_k^{(\mathbf{1})}$ and N_T repetitions of $\mathbf{R}_k^{(\mathbf{0})}$.

5.4.3 Classification analysis on real EEG data

In this subsection, we verify the ability of the Deep L1-PCA procedure to identify the two mental states of motor imagery and resting in an off-line classification scenario.

Similarly to synthetic data, we perform a a 10 repeated 10-fold LDA classification for each batch and each layer. In Fig. 5.7 we report the associated results. In Fig. 5.7 A) results are related to the case in which the feature vector is composed by only the Laplacian diagonal elements (i.e.node strength values). Fig. 5.7 B) presents findings obtained when the feature vector is build with all the Laplacian matrix. In both the cases, we can recognize a general accuracy improvement considering progressively higher layers from $k = 1$ to $k = 3$. Classification results generally improve when also extra-diagonal Laplacian elements are considered with respect to those obtained with only diagonal elements (maximum value of 82% compared to 75%).

For sake of completeness, we report in Table 5.3 results for the 8 observations on original data. Accuracy values are generally lower compared to those obtained after Deep L1-PC computations. Even for original data collected in short-time windows the inclusion of extra-diagonal elements helps the classification.

We demonstrate the potential of Deep L1-PCA to improve the discrimination of two mental states during motor imagery task. The most important contribution concerns the possibility to consider short-time intervals to obtain a robust connectivity estimation. This aspect is fundamental for BCI applicability in real scenario.

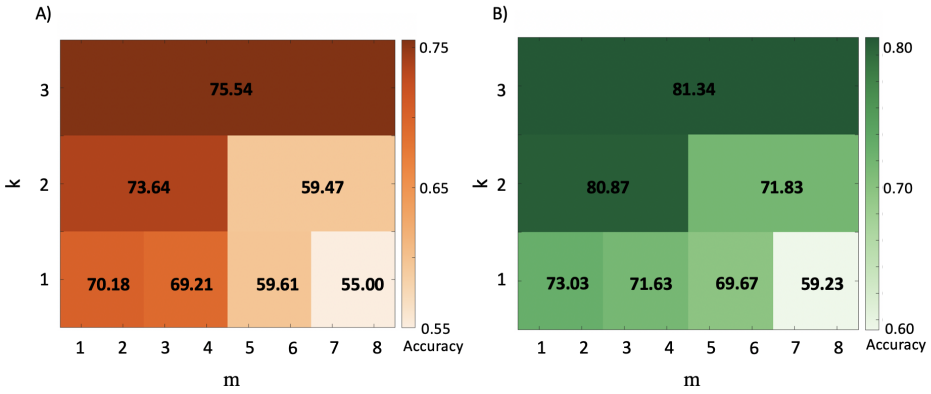

Figure 5.7: Accuracy of classification framework for real EEG data associated to each layer and each batch. In the rows we have the different layers and in the columns we have the batches, which are 4 at the first layer, 2 at the second and 1 batch at the final layer. In panel A), we report accuracy results when only the Laplacian diagonal elements are taken as classification features. In panel B) results are obtained when all the Laplacian elements are considered as features.

Time windows

Accuracy	1	2	3	4	5	6	7	8
Laplacian diagonal elements	62.02	63.86	59.59	65.64	56.03	53.46	57.04	57.62
All Laplacian elements	71.14	69.52	62.52	60.98	58.27	62.07	59.38	57.54

Table 5.3: Classification accuracy for real EEG data related to the original $M = 8$ observations. In the first row, we have accuracies when only the Laplacian diagonal elements are taken as classification features. In the second row, accuracy values relate to when all the Laplacian elements are considered as features.

5.5 Deep L1-PCA applicability in BCI systems

BCIs require real-time interaction between user and interface [207], which implies time-varying computation of the BCI features. Deep L1-PCA provides a useful tool to have robust short-time estimates of graph Laplacians with low computational cost. Novel techniques have been recently developed to capture temporal evolution of graphs. Tracking algorithms has been proposed in [176] and [137] under the hypothesis of low rank temporal dynamics of FC. Other state-of-the-art strategies require smoothness on time dimension to solve advanced regularization problems [92, 211]. Besides, techniques based on the estimation of spatio-temporal graphs describe the connectivity patterns across time but often the computation cost is really high [136, 161]. The advantage of Deep L1-PCA with respect to the other methods is that it is naturally suitable to deal with noisy data, it does not require any specific assumption and it has reduced computational cost.

We propose a scheme to actually apply the Deep L1-PCA to BCI scenarios.

In order to understand the potential of the Deep L1-PCA in BCIs, let us imagine to perform an online experiment, where time samples are progressively available and we suppose to have already trained the classifier. Once we have received all the samples in the first m time-interval, we can estimate functional connectivity and derive the Laplacian matrix. After first computation, the first classification can be done to give a feedback to the user. As the time passes, we collect other batches and we start to build the Deep structure. For instance, once the second Laplacian at $m = 2$ is estimated, we can compute the PC to obtain $\mathbf{r}_1(1)$. We can continue this procedure until the end of the trial, when we have the whole Deep structure. Since we verified that accuracy increases with higher layers, it is more convenient to perform classification at the highest available layer. The possibility of considering high layers depends on the available data already collected. In Fig.5.8 we have the M time intervals and we indicate with red arrows the time interval in which we have enough data to pass to the higher layers.

This procedure enables to simultaneously i) perform classification at each new short-time interval to immediately interact with the subject with a possible feedback ii) build the Deep structure to collect all the layers to obtain higher layer estimations, which can be progressively used to detect subject's mental state.

Let us remark that for this analysis we have one Laplacian computation each 500 ms but modifications can be done to have more frequent estimations. In real BCI applications, parameters can be tuned to change the length of the time-windows or to apply an overlap. These results pave the way for the application of Deep L1-PCA framework to EEG data to online control BCI systems.

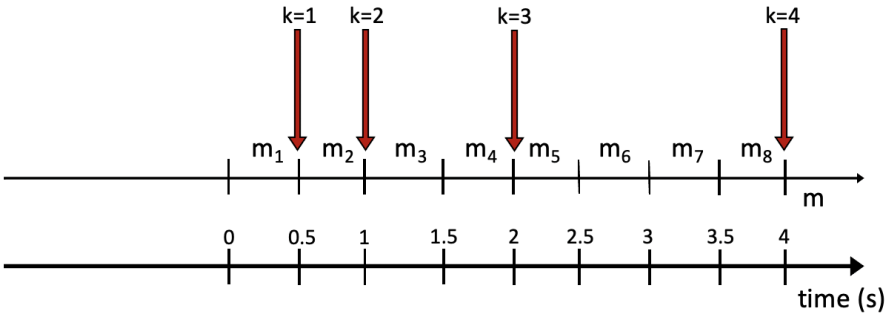

Figure 5.8: Graphical representation of data recordings. As the time passes, we collect m time-windows in which we can estimate the graph Laplacian. As soon as new time intervals are recorded we can compute the Deep L1-PCs at several layers. Here, we indicate with red arrows the time instant (and the associated time interval) in which we can reach an higher level. In fact, after 500ms, we have the first Laplacian estimation and the first classification can be performed. After the second interval (i.e. at 1s) the first L1-PCs can be computed. We have to wait until 2s (i.e. the $4th$ interval) to collect all the samples to complete the first layer with $k = 1$ and to perform the second L1-PCA, reaching the second layer. At 4s, we have all the samples needed to compute the last L1-PCA.

5.6 Conclusions

We proposed a novel formulation of the L1-PCA, to which we refer to as Deep L1-PCA. This is an iterative procedure, where in the first layer, original data are partitioned in batches and L1-PCs are extracted in each group. In the next layer, the input data are the L1-PCA bases obtained as output of the previous layer. With the recursive application of this method, original data are represented in a more compact way. The method ends with the possibility to extract one global PC. The Deep L1-PCA is applied to graph synthetic data to verify the robustness to noise and the applicability to classification scenarios. The last part of this work concerns results on real EEG data recorded during motor imagery-based BCI experiments. This method offers the possibility to realize a fast interaction between user and machine by improving the classification at higher layers. More research is needed to test this method in real-time applications as well as to compare it with other state-of-the-art techniques.

Comparing Laplacian denoising in Chapter 4 with Deep L1-PCA, it is clear that while the first requires training and a maximum likelihood estimator to optimally separate data, the latter is simple and fast and it is defined in the linear space. LWe remark that the Laplacian denoising algorithm can be improved for BCI purpose, by means of covariance matrix tracking, or learning techniques to

avoid the estimation of the transformation parameters [4]. One possibility to benefit of the two approaches is to integrate them to have a robust estimation of graph Laplacian and, simultaneously, to preserve the advantages of Deep L1-PCA. This can be done at the classification level, using fusion procedures [46, 164] or the two methods can be integrated to obtain another version of the graph Laplacian matrix, for instance, combining eigenvectors. In real BCI applications, an appropriate way to identify the most suitable features and the most appropriate strategy to obtain robust FC estimates for a specifc user consists in performing preliminary analyses during the calibration phase .

Chapter 6

Implementation of graph connectivity estimation on Inria OpenViBE software

BCI are communication systems that enable the interaction between subjects and external word through brain activity only. BCIs are gaining more and more interest because of their potential for control, communication and rehabilitation applications. In this scenario, many solutions have been developed to design and use BCI systems. Among the others, we use the Inria OpenViBE software. OpenViBE is a software platform which allows engineers and researchers to design and practically use a BCI systems. It is a free software distributed with an open-source license. Here, we develop a novel box into this software to implement connectivity estimation and Laplacian denoising. We test our algorithm on synthetic and real data, which are EEG signals recorded from 74 channels. We finally show the applicability of the new box in term of computational time. Our contribution is a step forward in the direction of the development of connectivity-based BCIs.

6.1 Introduction

Many solutions have been developed to design and use BCI systems. Generally, the task of designing a BCI systems needs expertise from different domain, from signal processing, computer programming, neuro-physiology. A software platform for BCIs has to provide the basic tools to easily design the BCI and to correctly use it in real-time scenarios.

Among the others [109, 118, 171], we use the Inria OpenViBE software [159]. OpenViBE is a software platform which allows engineers and researchers to design and practically use a BCI systems. It is a free software distributed with an open-source license and is entirely uses free and open source software.

Our theoretical framework presented in previous chapters provides an original method to include graph FC features in the identification and characterization of human mental states. To test the feasibility of our approach we are currently implementing it in OpenViBE. This work is a collaboration with the Inria engineer Arthur Desbois in the Aramis team. We develop a novel box into OpenViBE which enables the computation of the connectivity features, i.e. coherence and imaginary coherence. All the parameters needed to correctly specify the algorithms can be easily visualized and modified by the user. The novel OpenViBE box is tested with off-line experiments on simulated and real data. Real data are EEG recordings from 74 electrodes on one subject performing motor imagery tasks.

6.2 Implementation of connectivity box

OpenViBE is an Inria software that allows engineers and researchers to design BCI systems [159]. The way of programming this software consists in developing boxes, which are the key element of the platform. One box is the elementary component which controls a part of the pipeline. Each box takes inputs and subsequently gives outputs for the next box. Interestingly, new boxes are immediately available to the BCI community trough the plug-in system.

We implement a connectivity measurement box to perform the computation of connectivity estimators. In particular, the estimators that have been developed are the spectral coherence and the imaginary coherence, as described in the previous chapters with the differences that imaginary coherence is taken without the absolute value at this stage. Specifically, once signals are recorded (or generated) by the previous boxes, they become the input for the connectivity measurement box, which gives the adjacency matrix as output. In Fig. 6.1, we show an OpenViBE code, which includes connectivity estimation (highlighted in the red box). The

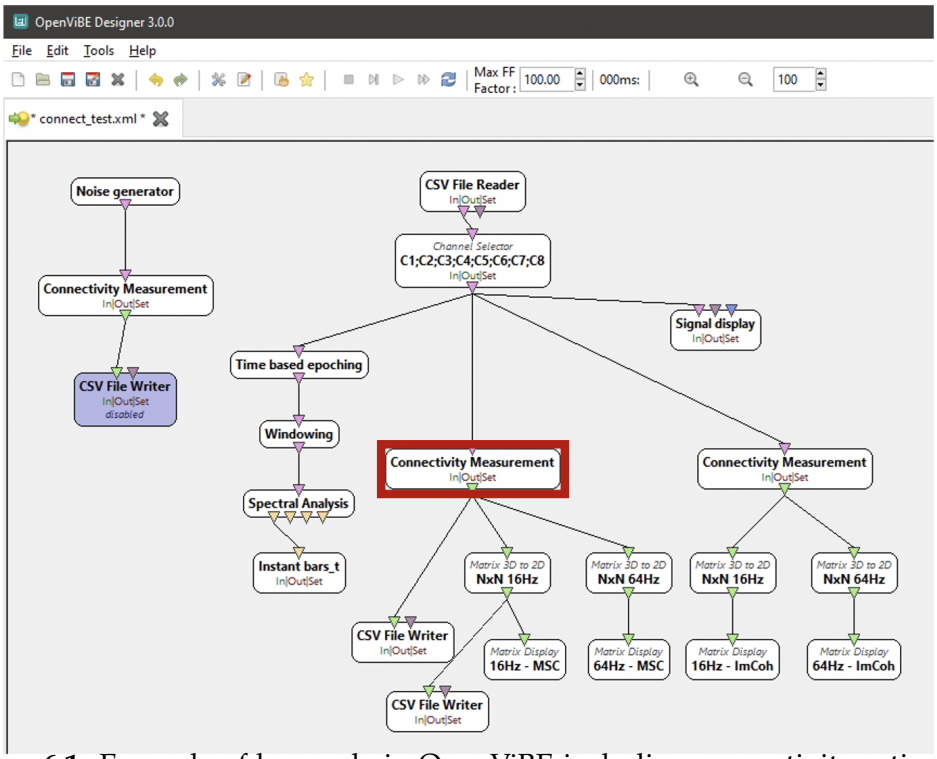

Figure 6.1: Example of box code in OpenViBE including connectivity estimation. The connectivity measurement box is highlighted in red.

box requires some fundamental parameters, i.e. the connectivity metric, the parameters for Welch estimation, the length of the windows to compute connectivity with a possible overlap and the number of FFT samples. All these parameters are shown in Fig.6.2, as they are presented in the platform.

6.3 Results of of connectivity box

In this section, we test the connectivity measurement box. We firstly define a set of signals able to generate a clear connectivity pattern, and then, we consider real EEG signals recorded during motor imagery tasks.

6.3.1 Connectivity estimation with synthetic data

In order to test the connectivity measurement box, we firstly consider 8 synthetic signal, generated at 8 nodes, identified with letters in alphabetic order from A to H. The signals are sine waves at two frequencies $f_1 = 16Hz$ and $f_2 = 64Hz$.

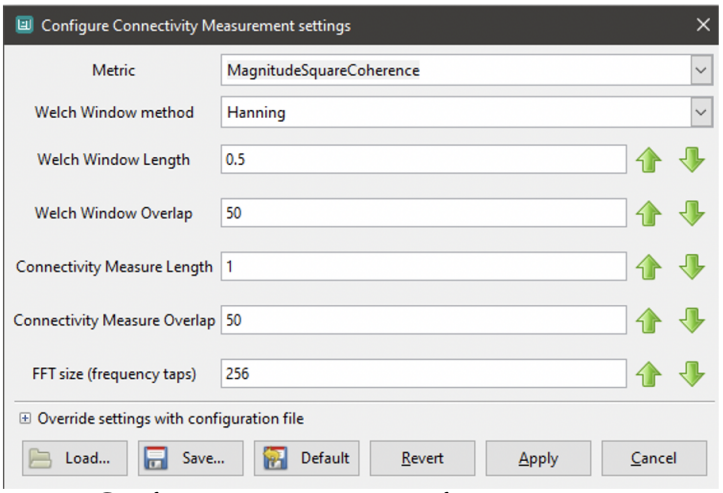

Figure 6.2: Configuration parameters for connectivity estimation.

$$
\begin{aligned}
y^1[\nu T_s] &= 10sin(2\pi f_1 t)|_{t=\nu T_s} + 8sin(2\pi f_2 t)|_{t=\nu T_s};\\
y^2[\nu T_s] &= 10sin(2\pi f_1 t - \pi/2)|_{t=\nu T_s} + 8sin(2\pi f 2_t)|_{t=\nu T_s};;\\
y^3[\nu T_s] &= 10sin(2\pi f_1 t)|_{t=\nu T_s} + 8sin(2\pi f_2 t - \pi/2)|_{t=\nu T_s};\\
y^4[\nu T_s] &= 10sin(2\pi f_1 t - \pi/2)|_{t=\nu T_s} + 8sin(2\pi f_2 t - \pi/2)|_{t=\nu T_s};\\
y^5[\nu T_s] &= 10sin(2\pi f_1 t|_{t=\nu T_s});\\
y^6[\nu T_s] &= 8sin(2\pi f_2 t)|_{t=\nu T_s};\\
y^7[\nu T_s] &= 10sin(2\pi f_1 t - \pi/2)|_{t=\nu T_s};\\
y^8[\nu T_s] &= 8sin(2\pi f_2 t - \pi/2)|_{t=\nu T_s};
\end{aligned}
\tag{6.1}
$$

Results in terms of connectivity matrices are shown in Fig. 6.4. Here, we have OpenViBE results of coherence and imaginary coherence computation in real time. In fact, as signals arrive, the connectivity matrices are dynamically computed. We can see in the first row the results of connectivity estimation (i.e. coherence in the right panel and imaginary coherence in the left panel) at 16Hz, while results (i.e. coherence in the right panel and imaginary coherence in the left panel) at 64 are reported in the second row. We notice that results change depending on the pair of nodes for connectivity estimation. For instance, if we take into consideration A and B nodes at 16 Hz, the coherence is high because signals at this frequency are only shifted one with respect to the other. At the same frequency, the signals at A and B nodes generates also high connectivity in terms of imaginary coherence, because of the presence of the phase difference.

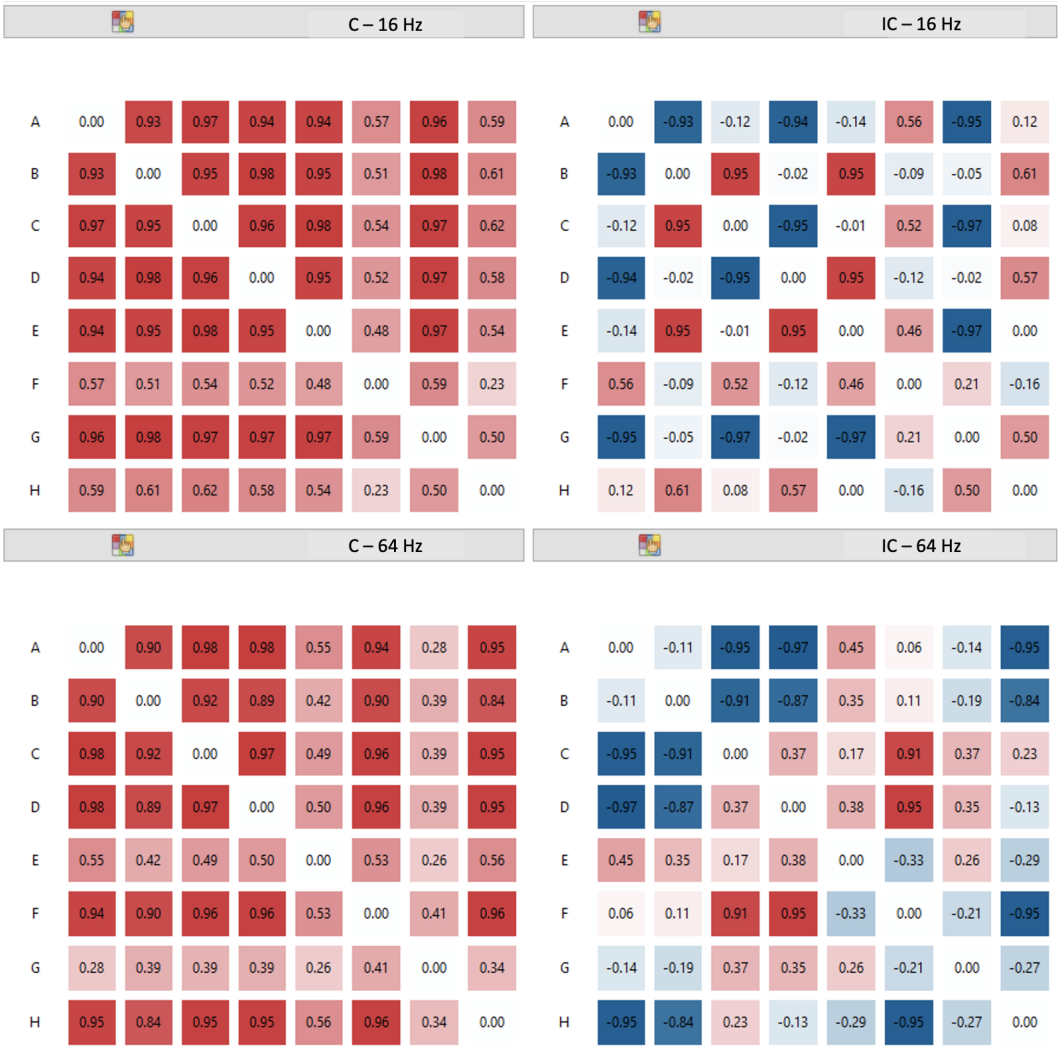

Figure 6.3: Results of OpenViBE connectivity estimation through a novel visualization box. In the first row, we have results at 16 Hz, while in the second row, we have results for 64Hz. Right panels report results for spectral coherence and left panels those related to imaginary coherence.

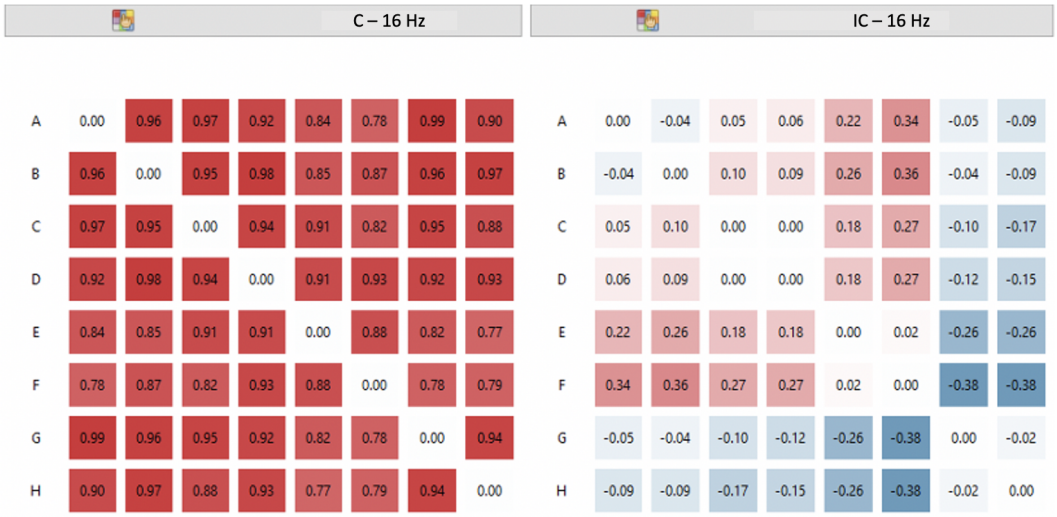

Figure 6.4: Results of OpenViBE connectivity estimation on real EEG data. We report results at 16 Hz. Left panel shows results for spectral coherence and right panel those related to imaginary coherence. In this representation; A: Cz;B: CPz;C: C2;D: CP2;E: C4;F: CP4; G: C1; H: CP1

6.3.2 Connectivity estimation with real EEG data

After testing the connectivity measurement box with synthetic data, we consider EEG signals recorded from one subject during motor imagery experiments. Since the connectivity visualization box, is not optimized and the representation of many channels can be confusing, we only consider 8 electrodes.

The connectivity measurement box is used to compute connectivity estimations in real time, which means that as the samples needed for one computation (which lasts 2 s in our example) arrive at the software, the box dynamically computes (and visualize) connectivity results. To perform this analysis, the time window to for the FC estimation lasts 2s; for what concerns the spectral estimates, we use Welch windows of 250 m with an overlap of 50%. An example is shown in Fig. **??** for coherence and imaginary coherence at 16 Hz.

6.4 Performance tests

The connectivity measurement box computes the connectivity in terms of coherence or imaginary coherence from a set of signals recorded (or generated) in a set a nodes. In other words, the novel box estimates connectivity from every pair of signals. One important aspect when considering real BCI systems is that all the estimates need to be performed online. For this reason, in this section we study

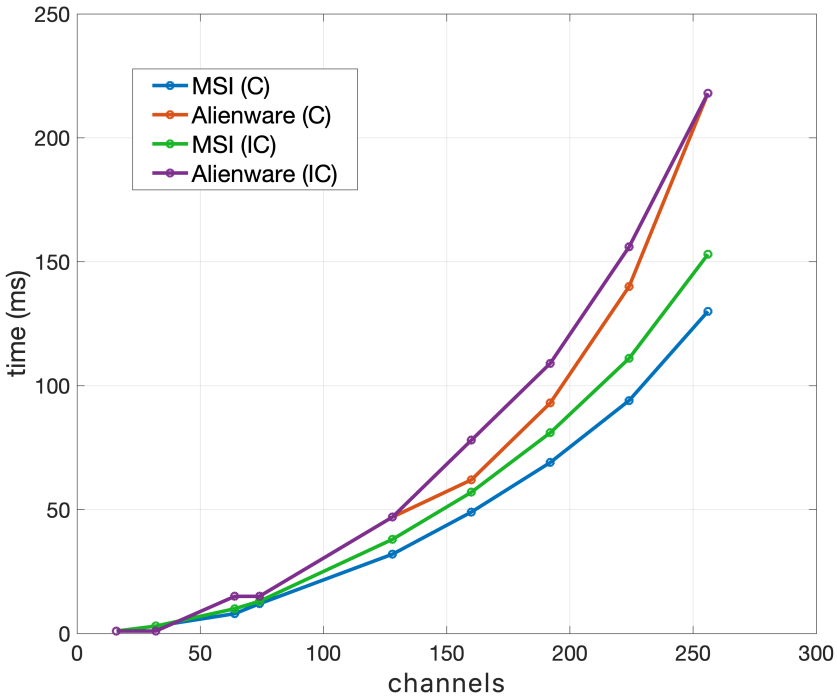

Figure 6.5: OpenViBE performance in terms of computational time for coherence (C) and imaginary coherence (IC)estimations. Results are shown for two computers (PC "Alienware" and PC "MSI").

the computational time necessary for connectivity estimation in OpenViBE varying the number of nodes. For this analysis, we consider two different computers: 1) PC "Alienware"; CPU : i7-8750H (6 cores @ 2.20GHz, hyper-thread with 12 virtual cores; Memory : 8 GB RAM HDD 1TB; OpenViBE 3.0.0 (Windows 10); 2) PC "MSI" : CPU : i7-9700K (8 cores @ 3.6GHz) Memory : 32 GB SSD : 500 GB (system & programs) HDD : 1TB (data storage) OpenViBE 3.0.0 (Windows 10).

Results of this study are reported in Fig. 6.5. We can see that until 50 channels, which is reasonable for BCI applications, the time delay for the connectivity estimation is lower than 50ms, while the time delay dramatically increases when the number of nodes increases . Interestingly, the time needed to compute spectral coherence is always lower compared to imaginary coherence. In addition, results obtained for "MSI" PC are always better than those obtained with "Alienware" PC.

6.5 Conclusions and future work

We proposed a novel development for OpenViBE platform in order to compute connectivity estimators and to visualize results in a dynamic way. We tested it

on synthetic and real EEG data recorded during motor imagery experiments. We demonstrated that, until a certain number of nodes, the computation is relatively fast and it enables to perform real-BCI experiments. The connectivity box has been tested by OpenViBE team and it will be available in the future release. Further study is needed to improve the visualization of adjacency matrices in order to have more readable results. In addition, the validation of the box in an experimental setting with online recording of EEG signals from healthy and diseased subjects is needed to fully investigate the performances of the box. This step has a crucial importance because it will unveil the actual potential of connectivity-based BCI. The other theoretical developments presented in this thesis (Laplacian denoising, Deep L1-PCA) , which constitute a fundamental part of this thesis, will be developed in the future.

Chapter 7

Conclusions and future perspectives

Conclusions

In this thesis, we investigated the potential of functional connectivity networks to characterize BCI related tasks. We proposed an original framework to adapt graph theory, signal processing and graph signal processing tools in order to have insight in brain processes during cognitive tasks.

By applying functional connectivity and network estimators to characterize brain states, we uncovered functional interaction changes between graph nodes during motor imagery tasks. In addition, we demonstrated that including FC-based features in the classification generally performs better than standard techniques alone in detecting the user's mental state [120]. Investigating motor imagery tasks, we discovered the presence of a twofold FC mechanism based on phase and amplitude synchronization between EEG signals.

We developed a novel algorithm to robustly estimate graph Laplacian and to improve the separability between two brain states. We introduced a denoising procedure to obtain a more robust graph FC estimation, based on tools from different domains, such as information theory and graph signal processing. In this context, the separability between two brain states was quantified by an original formulation of the Jensen divergence, which highlights the contribution of each Laplacian element to the final discrimination.

Finally, we presented a novel framework to obtain short-time estimates of graph connectivity using an innovative tool, named Deep L1-PCA. This method is able to capture the dynamic of time-varying signals and to rapidly identify the user's mental state with an iterative robust procedure, particularly appropriate for

BCI applications.

In the last part of our work, we present an ongoing work of implementing connectivity-based BCIs on Inria OpenViBE platform. We verified the feasibility of the approach in terms of computational time necessary to estimate connectivity features. This aspect is a crucial point to demonstrate the actual applicability of the whole work to real BCI systems.

Taken together, our findings pave the way for the development of alternative BCI systems, based on FC-related features. However, it is important to underline that particular attention should be devoted to the practical implementation of the whole framework. First of all, there are subjects for which connectivity is not useful for a classification perspective. For those subjects, FC gives description of the brain functioning but it is better not to include it in the classification framework. There are some parameters to be set, such as the number of eigenvectors needed to define the different subspaces for the Laplacian denoising algorithm. In the J-divergence analysis, a threshold has to be fixed to separate the Laplacian variables changing only in mean value from those changing also in variance. For what concerns the L1-PCA computation, the number of elements in each batch has to be set and it influences the number of observations necessary to perform the PCA analysis in higher layers. Since these values are intrinsically dependent on the subject and the task, we recommend to train the algorithms and set all the parameters before testing the experiments. This training step can be, for example, performed during the BCI calibration phase.

More in general, we estimated FC networks by computing coherence and imaginary coherence, but several other measures can be adopted to quantify brain interactions [16, 69, 77]. The choice of the FC estimator can, in principle, depend on the subject, because humans use different strategies to perform motor or cognitive tasks. In this thesis, we preferred FC with two characteristics, which are the simplicity and the interpretability, but subjects can develop different strategies to perform motor imagery tasks, which can be captured by other estimators [52]. More research is needed to generalize our entire method to more subjects by using, for instance, different databases [188]. Although our research demonstrates that FC features capture complementary information with respect to univariate features, the extent to which they can be applied to real BCI systems strongly depends on the subjects. This problem might be solved at the level of BCI design, in fact feature selection procedures can be performed during the calibration phase.

Future perspectives

Our proposed framework provides a practical approach to include graph FC features in the identification and characterization of human mental states. The research in this thesis aims to improve motor imagery-based BCI systems by taking into consideration informative features describing brain interaction mechanisms. To test the feasibility of our approach we are currently implementing it into the Inria Openvibe software [159]. This ongoing work is a collaboration with the Inria engineer Arthur Desbois in the Aramis team. The technical implementation have been developed and results on off-line tests demonstrate the applicability of our methods in real BCIs. Future work is needed to implement the Laplacian denoising and the Deep L1-PCA algorithms, which are the critical parts of the proposed theoretical framework. Finally, the actual improvement of connectivity-based BCI performance will be tested on healthy subjects and patiences.

The method introduced in Chapter 5 provided a framework to obtain a short-time graph connectivity estimation in a robust way, using an iterative algorithm for principal components analysis. This procedure is particularly appropriate for BCI applications because it gives as output both the estimations at each short-time interval and the whole Deep structure containing the computations at each layer. The proposed method does not model the time evolution of the graph, which can in principle offer new insight in brain (re)organization processes. In this direction, we proposed in [44], a compound Markov random field model, able to jointly model signal values, graph connectivity and the community structure. Our method, based on signal, connectivity and community fields, generalizes classical Markov model to simultaneously address problems of learning, signal recovery and community detection.
As future work we can further develop the model to describe time-varying SoG evolution. One possible strategy to adapt the model is to add a process to consider the temporal evolution of graph edges. In principle, the modified version of the Markov random field model has the potential to describe the temporal evolution of the graph and it might be applied in BCI to observe spatio-temporal changes during a motor or cognitive task.

Bibliography

[1] M.R.H. Abdalmoaty, H. Hjalmarsson, and B. Wahlberg. The gaussian maximum-likelihood estimator versus the optimally weighted least-squares estimator [lecture notes]. *IEEE Signal Processing Magazine*, 37(6):195–199, 2020.

[2] M. Ahn and S.C. Jun. Performance variation in motor imagery brain–computer interface: a brief review. *Journal of neuroscience methods*, 243:103–110, 2015.

[3] V. Alessandro. Twenty years of network science. *Nature*, 558(7711):528–529, 2018.

[4] A. Ali, M. Testa, T. Bianchi, and E. Magli. Biometricnet: deep unconstrained face verification through learning of metrics regularized onto gaussian distributions. *arXiv preprint arXiv:2008.06021*, 2020.

[5] B.Z. Allison and C. Neuper. Could anyone use a bci? In *Brain-computer interfaces*, pages 35–54. Springer, 2010.

[6] C. Andreou, H. Frielinghaus, J. Rauh, M. Mußmann, S. Vauth, P. Braun, G. Leicht, and C. Mulert. Theta and high-beta networks for feedback processing: a simultaneous eeg–fmri study in healthy male subjects. *Translational Psychiatry*, 7(1):e1016–e1016, 2017.

[7] K.K. Ang, Z.Y. Chin, C. Wang, C. Guan, and H. Zhang. Filter bank common spatial pattern algorithm on bci competition iv datasets 2a and 2b. *Frontiers in neuroscience*, 6:39, 2012.

[8] M.B. Arias, M. Kim, and S. Bae. Prediction of electric vehicle charging-power demand in realistic urban traffic networks. *Applied energy*, 195:738–753, 2017.

[9] S. Aydore, D. Pantazis, and R.M. Leahy. A note on the phase locking value and its properties. *Neuroimage*, 74:231–244, 2013.

[10] S. Baillet, J.C. Mosher, and R.M. Leahy. Electromagnetic brain mapping. *IEEE Signal processing magazine*, 18(6):14–30, 2001.

[11] H. Bakhshayesh, S.P. Fitzgibbon, A.S. Janani, T.S. Grummett, and K.J. Pope. Detecting synchrony in eeg: A comparative study of functional connectivity measures. *Computers in Biology and Medicine*, 105:1–15, 2019.

[12] O.M. Baksalary and G. Trenkler. On subspace distances determined by the frobenius norm. *Linear Algebra and its Applications*, 448:245–263, 2014.

[13] A. Barachant, S. Bonnet, M. Congedo, and C. Jutten. Riemannian geometry applied to bci classification. In *International Conference on Latent Variable Analysis and Signal Separation*, pages 629–636. Springer, 2010.

[14] D.S. Bassett and O. Sporns. Network neuroscience. *Nature neuroscience*, 20 (3):353–364, 2017.

[15] M. Basseville. Divergence measures for statistical data processing—an annotated bibliography. *Signal Processing*, 93(4):621–633, 2013.

[16] A.M. Bastos and J.M. Schoffelen. A tutorial review of functional connectivity analysis methods and their interpretational pitfalls. *Frontiers in systems neuroscience*, 9:175, 2016.

[17] O. Bazanova and D. Vernon. Interpreting eeg alpha activity. *Neuroscience & Biobehavioral Reviews*, 44:94–110, 2014.

[18] A.J. Bell and T.J. Sejnowski. An information-maximization approach to blind separation and blind deconvolution. *Neural computation*, 7(6):1129–1159, 1995.

[19] Y. Benjamini and Y. Hochberg. Controlling the false discovery rate: a practical and powerful approach to multiple testing. *Journal of the Royal statistical society: series B (Methodological)*, 57(1):289–300, 1995.

[20] B. Blankertz, G. Dornhege, M. Krauledat, K.R. Müller, and G. Curio. The non-invasive berlin brain–computer interface: fast acquisition of effective performance in untrained subjects. *NeuroImage*, 37(2):539–550, 2007.

[21] B. Blankertz, C. Sanelli, S. Halder, E.M. Hammer, A. Kübler, K.R. Müller, G. Curio, and T. Dickhaus. Predicting bci performance to study bci illiteracy. 2009.

[22] S. Boccaletti, V. Latora, Y. Moreno, M. Chavez, and D.U. Hwang. Complex networks: Structure and dynamics. *Physics reports*, 424(4-5):175–308, 2006.

[23] T.A. Bolton and D. van De Ville. Dynamics of brain activity captured by graph signal processing of neuroimaging data to predict human behaviour. In *2020 IEEE 17th International Symposium on Biomedical Imaging (ISBI)*, pages 549–553. IEEE, 2020.

[24] P. Boveroux, A. Vanhaudenhuyse, M.A. Bruno, Q. Noirhomme, S. Lauwick, A. Luxen, C. Degueldre, A. Plenevaux, C. Schnakers, C. Phillips, et al. Breakdown of within-and between-network resting state functional magnetic resonance imaging connectivity during propofol-induced loss of consciousness. *Anesthesiology: The Journal of the American Society of Anesthesiologists*, 113(5): 1038–1053, 2010.

[25] C. Brunner, B. Graimann, J.E. Huggins, S.P. Levine, and G. Pfurtscheller. Phase relationships between different subdural electrode recordings in man. *Neuroscience letters*, 375(2):69–74, 2005.

[26] C. Brunner, R. Scherer, B. Graimann, G. Supp, and G. Pfurtscheller. Online control of a brain-computer interface using phase synchronization. *IEEE Transactions on Biomedical Engineering*, 53(12):2501–2506, 2006.

[27] E. Bullmore and O. Sporns. Complex brain networks: graph theoretical analysis of structural and functional systems. *Nature reviews neuroscience*, 10 (3):186–198, 2009.

[28] N. Caramia, F. Lotte, and S. Ramat. Optimizing spatial filter pairs for eeg classification based on phase-synchronization. In *2014 IEEE International Conference on Acoustics, Speech and Signal Processing (ICASSP)*, pages 2049–2053. IEEE, 2014.

[29] T. Carlson and J.d.R. Millan. Brain-controlled wheelchairs: a robotic architecture. *IEEE Robotics & Automation Magazine*, 20(1):65–73, 2013.

[30] G.C. Carter. Coherence and time delay estimation. *Proceedings of the IEEE*, 75(2):236–255, 1987.

[31] T. Cattai, S. Colonnese, M.C. Corsi, D.S. Bassett, G. Scarano, and F.D.V. Fallani. Characterization of mental states through node connectivity between brain signals. In *2018 26th European Signal Processing Conference (EUSIPCO)*, pages 1377–1381. IEEE, 2018.

[32] T. Cattai, S. Colonnese, M.C. Corsi, D.S. Bassett, G. Scarano, and F. de Vico Fallani. Combination of connectivity and spectral features for motor-imagery bci. In *GBCIC*, 2019.

[33] T. Cattai, S. Colonnese, M.C. Corsi, D.S. Bassett, G. Scarano, and F. De Vico Fallani. Phase/amplitude synchronization of brain signals during motor imagery bci tasks. *arXiv preprint arXiv:1912.02745*, 2019.

[34] T. Cattai, G. Scarano, M.C. Corsi, D.S. Bassett, F. De Vico Fallani, and S. Colonnese. Improving j-divergence of brain connectivity states by graph laplacian denoising. *arXiv preprint arXiv:2012.11240*, 2020.

[35] E. Ceci and S. Barbarossa. Graph signal processing in the presence of topology uncertainties. *IEEE Transactions on Signal Processing*, 68:1558–1573, 2020.

[36] C. Chang and G.H. Glover. Time–frequency dynamics of resting-state brain connectivity measured with fmri. *Neuroimage*, 50(1):81–98, 2010.

[37] Y.M. Chang, N.J. Hsu, and H.C. Huang. Semiparametric estimation and selection for nonstationary spatial covariance functions. *Journal of Computational and Graphical Statistics*, 19(1):117–139, 2010.

[38] U. Chaudhary, N. Mrachacz-Kersting, and N. Birbaumer. Neuropsychological and neurophysiological aspects of brain-computer-interface (bci) control in paralysis. *The Journal of Physiology*, 2020.

[39] M. Chavez and B. Cazelles. Detecting dynamic spatial correlation patterns with generalized wavelet coherence and non-stationary surrogate data. *Scientific reports*, 9(1):1–9, 2019.

[40] M. Chen, R.T. Wakai, and B. Van Veen. Eigenvector based spatial filtering of fetal biomagnetic signals. *Journal of perinatal medicine*, 29(6):486–496, 2001.

[41] P. Chevalier and B. Picinbono. Complex linear-quadratic systems for detection and array processing. *IEEE transactions on signal processing*, 44(10): 2631–2634, 1996.

[42] A. Cichocki, D. Mandic, L. De Lathauwer, G. Zhou, Q. Zhao, C. Caiafa, and H.A. Phan. Tensor decompositions for signal processing applications: From two-way to multiway component analysis. *IEEE signal processing magazine*, 32(2):145–163, 2015.

[43] A.L. Cohen, D.A. Fair, N.U. Dosenbach, F.M. Miezin, D. Dierker, D.C. Van Essen, B.L. Schlaggar, and S.E. Petersen. Defining functional areas in

individual human brains using resting functional connectivity mri. *Neuroimage*, 41(1):45–57, 2008.

[44] S. Colonnese, P. Di Lorenzo, T. Cattai, G. Scarano, and F. De Vico Fallani. A joint markov model for communities, connectivity and signals defined over graphs. *IEEE Signal Processing Letters*, 27:1160–1164, 2020.

[45] M. Congedo. *Non-Parametric Synchronization Measures used in EEG and MEG*. PhD thesis, GIPSA-lab, 2018.

[46] M.C. Corsi, M. Chavez, D. Schwartz, L. Hugueville, A.N. Khambhati, D.S. Bassett, and F. De Vico Fallani. Integrating eeg and meg signals to improve motor imagery classification in brain–computer interface. *International journal of neural systems*, 29(01):1850014, 2019.

[47] N.E. Crone, A. Sinai, and A. Korzeniewska. High-frequency gamma oscillations and human brain mapping with electrocorticography. *Progress in brain research*, 159:275–295, 2006.

[48] I. Daly, S.J. Nasuto, and K. Warwick. Brain computer interface control via functional connectivity dynamics. *Pattern recognition*, 45(6):2123–2136, 2012.

[49] C.M. Davidson, A.M. de Paor, and M.M. Lowery. Application of describing function analysis to a model of deep brain stimulation. *IEEE Transactions on Biomedical Engineering*, 61(3):957–965, 2013.

[50] F. De Vico Fallani and D.S. Bassett. Network neuroscience for optimizing brain–computer interfaces. *Physics of life reviews*, 31:304–309, 2019.

[51] F. De Vico Fallani, L. Astolfi, F. Cincotti, D. Mattia, D. La Rocca, E. Maksuti, S. Salinari, F. Babiloni, B. Vegso, G. Kozmann, et al. Evaluation of the brain network organization from eeg signals: a preliminary evidence in stroke patient. *The Anatomical Record: Advances in Integrative Anatomy and Evolutionary Biology: Advances in Integrative Anatomy and Evolutionary Biology*, 292 (12):2023–2031, 2009.

[52] F. De Vico Fallani, J. Richiardi, M. Chavez, and S. Achard. Graph analysis of functional brain networks: practical issues in translational neuroscience. *Phil. Trans. R. Soc. B*, 369(1653):20130521, 2014.

[53] F. De Vico Fallani, V. Latora, and M. Chavez. A topological criterion for filtering information in complex brain networks. *PLoS computational biology*, 13(1):e1005305, 2017.

[54] A. Delorme, T. Sejnowski, and S. Makeig. Enhanced detection of artifacts in eeg data using higher-order statistics and independent component analysis. *Neuroimage*, 34(4):1443–1449, 2007.

[55] M. Denker, L. Zehl, B.E. Kilavik, M. Diesmann, T. Brochier, A. Riehle, and S. Grün. Lfp beta amplitude is linked to mesoscopic spatio-temporal phase patterns. *Scientific reports*, 8(1):5200, 2018.

[56] B.J. Edelman, B. Baxter, and B. He. Eeg source imaging enhances the decoding of complex right-hand motor imagery tasks. *IEEE Transactions on Biomedical Engineering*, 63(1):4–14, 2015.

[57] G. Edlinger, B.Z. Allison, and C. Guger. How many people can use a bci system? In *Clinical systems neuroscience*, pages 33–66. Springer, 2015.

[58] F. Ferri, P. Pudil, M. Hatef, and J. Kittler. Comparative study of techniques for large-scale feature selection. In *Machine Intelligence and Pattern Recognition*, volume 16, pages 403–413. Elsevier, 1994.

[59] A. Fornito, A. Zalesky, and M. Breakspear. The connectomics of brain disorders. *Nature Reviews Neuroscience*, 16(3):159–172, 2015.

[60] A. Fornito, A. Zalesky, and E. Bullmore. *Fundamentals of brain network analysis*. Academic Press, 2016.

[61] M.D. Fox and M.E. Raichle. Spontaneous fluctuations in brain activity observed with functional magnetic resonance imaging. *Nature reviews neuroscience*, 8(9):700–711, 2007.

[62] F. Freyer, K. Aquino, P.A. Robinson, P. Ritter, and M. Breakspear. Bistability and non-gaussian fluctuations in spontaneous cortical activity. *Journal of Neuroscience*, 29(26):8512–8524, 2009.

[63] K.J. Friston. Functional and effective connectivity: a review. *Brain connectivity*, 1(1):13–36, 2011.

[64] G. Frusque, J. Jung, P. Borgnat, and P. Gonçalves. Multiplex network inference with sparse tensor decomposition for functional connectivity. *IEEE transactions on Signal and Information Processing over Networks*, 6:316–328, 2020.

[65] P. Gaur, R.B. Pachori, H. Wang, and G. Prasad. A multi-class eeg-based bci classification using multivariate empirical mode decomposition based

filtering and riemannian geometry. *Expert Systems with Applications*, 95:201–211, 2018.

[66] N. Ghoroghchian, D.M. Groppe, R. Genov, T.A. Valiante, and S.C. Draper. Node-centric graph learning from data for brain state identification. *IEEE Transactions on Signal and Information Processing over Networks*, 6:120–132, 2020.

[67] J. Giles, K.K. Ang, L.S. Mihaylova, and M. Arvaneh. A subject-to-subject transfer learning framework based on jensen-shannon divergence for improving brain-computer interface. In *ICASSP 2019-2019 IEEE International Conference on Acoustics, Speech and Signal Processing (ICASSP)*, pages 3087–3091. IEEE, 2019.

[68] F.Z. Göğüş, G. Tezel, S. Özşen, S. Küççüktürk, H. Vatansev, and Y. Koca. Identification of apnea-hypopnea index subgroups based on multifractal detrended fluctuation analysis and nasal cannula airflow signals identification of apnea-hypopnea index subgroups based on multifractal detrended fluctuation analysis and nasal cannula airflow signals. 2020.

[69] J. Gonzalez-Astudillo, T. Cattai, G. Bassignana, M.C. Corsi, and F. De Vico Fallani. Network-based brain computer interfaces: principles and applications. *Journal of Neural Engineering*, 2020.

[70] C. Gouy-Pailler, S. Achard, B. Rivet, C. Jutten, E. Maby, A. Souloumiac, and M. Congedo. Topographical dynamics of brain connections for the design of asynchronous brain-computer interfaces. In *2007 29th Annual International Conference of the IEEE Engineering in Medicine and Biology Society*, pages 2520–2523. IEEE, 2007.

[71] M. Greco, S. Fortunati, and F. Gini. Maximum likelihood covariance matrix estimation for complex elliptically symmetric distributions under mismatched conditions. *Signal Processing*, 104:381–386, 2014.

[72] M. Grosse-Wentrup. Understanding brain connectivity patterns during motor imagery for brain-computer interfacing. In *Advances in neural information processing systems*, pages 561–568, 2009.

[73] A.G. Guggisberg, P.J. Koch, F.C. Hummel, and C.M. Buetefisch. Brain networks and their relevance for stroke rehabilitation. *Clinical Neurophysiology*, 130(7):1098–1124, 2019.

[74] P. Guttorp and A.M. Schmidt. Covariance structure of spatial and spatiotemporal processes. *Wiley Interdisciplinary Reviews: Computational Statistics*, 5(4): 279–287, 2013.

[75] E. Gysels and P. Celka. Phase synchronization for the recognition of mental tasks in a brain-computer interface. *IEEE Transactions on neural systems and rehabilitation engineering*, 12(4):406–415, 2004.

[76] M. Hamedi, S.H. Salleh, S.B. Samdin, and A.M. Noor. Motor imagery brain functional connectivity analysis via coherence. In *2015 IEEE International conference on signal and image processing applications (ICSIPA)*, pages 269–273. IEEE, 2015.

[77] M. Hamedi, S.H. Salleh, and A.M. Noor. Electroencephalographic motor imagery brain connectivity analysis for bci: a review. *Neural computation*, 28 (6):999–1041, 2016.

[78] B. He, L. Astolfi, P.A. Valdés-Sosa, D. Marinazzo, S.O. Palva, C.G. Bénar, C.M. Michel, and T. Koenig. Electrophysiological brain connectivity: theory and implementation. *IEEE transactions on biomedical engineering*, 66(7):2115–2137, 2019.

[79] L. Hedayatifar, R.A. Rigg, Y. Bar-Yam, and A.J. Morales. Us social fragmentation at multiple scales. *Journal of the Royal Society Interface*, 16(159):20190509, 2019.

[80] W. Huang, L. Goldsberry, N.F. Wymbs, S.T. Grafton, D.S. Bassett, and A. Ribeiro. Graph frequency analysis of brain signals. *IEEE journal of selected topics in signal processing*, 10(7):1189–1203, 2016.

[81] W. Huang, T.A. Bolton, J.D. Medaglia, D.S. Bassett, A. Ribeiro, and D. Van De Ville. A graph signal processing perspective on functional brain imaging. *Proceedings of the IEEE*, 106(5):868–885, 2018.

[82] R.M. Hutchison, T. Womelsdorf, E.A. Allen, P.A. Bandettini, V.D. Calhoun, M. Corbetta, S. Della Penna, J.H. Duyn, G.H. Glover, J. Gonzalez-Castillo, et al. Dynamic functional connectivity: promise, issues, and interpretations. *Neuroimage*, 80:360–378, 2013.

[83] E. Isufi, P. Banelli, P. Di Lorenzo, and G. Leus. Observing and tracking bandlimited graph processes from sampled measurements. *Signal Processing*, 177:107749, 2020.

[84] S. Itani and D. Thanou. A graph signal processing framework for the classification of temporal brain data. In *2020 28th European Signal Processing Conference (EUSIPCO)*, pages 1180–1184. IEEE, 2020.

[85] M.A. Jatoi, N. Kamel, A.S. Malik, I. Faye, and T. Begum. A survey of methods used for source localization using eeg signals. *Biomedical Signal Processing and Control*, 11:42–52, 2014.

[86] C. Jeunet, F. Lotte, J. Batail, P. Philip, and J. Micoulaud Franchi. Using recent bci literature to deepen our understanding of clinical neurofeedback: A short review. neuroscience [internet]. 2018 may 15 [cited 2018 jul 24];(378): 225–33.

[87] B. Jiang, A. Panahi, H. Krim, Y. Yu, and S.L. Smith. Dynamic graph learning based on graph laplacian. *arXiv preprint arXiv:2002.07044*, 2020.

[88] T. Jiang, Y. He, Y. Zang, and X. Weng. Modulation of functional connectivity during the resting state and the motor task. *Human brain mapping*, 22(1): 63–71, 2004.

[89] J. Jin, C. Liu, I. Daly, Y. Miao, S. Li, X. Wang, and A. Cichocki. Bispectrum-based channel selection for motor imagery based brain-computer interfacing. *IEEE Transactions on Neural Systems and Rehabilitation Engineering*, 28(10): 2153–2163, 2020.

[90] E.R. John. The neurophysics of consciousness. *Brain Research Reviews*, 39(1): 1–28, 2002.

[91] Y. Jonmohamadi, G. Poudel, C. Innes, and R. Jones. Source-space ica for eeg source separation, localization, and time-course reconstruction. *NeuroImage*, 101:720–737, 2014.

[92] V. Kalofolias, A. Loukas, D. Thanou, and P. Frossard. Learning time varying graphs. In *2017 IEEE International Conference on Acoustics, Speech and Signal Processing (ICASSP)*, pages 2826–2830. Ieee, 2017.

[93] M.J. Kaminski and K.J. Blinowska. A new method of the description of the information flow in the brain structures. *Biological cybernetics*, 65(3):203–210, 1991.

[94] A.Y. Kaplan, A.A. Fingelkurts, A.A. Fingelkurts, S.V. Borisov, and B.S. Darkhovsky. Nonstationary nature of the brain activity as revealed by eeg/meg: methodological, practical and conceptual challenges. *Signal processing*, 85 (11):2190–2212, 2005.

[95] Y. Kim, S. Han, S. Choi, and D. Hwang. Inference of dynamic networks using time-course data. *Briefings in bioinformatics*, 15(2):212–228, 2014.

[96] T.G. Kolda and B.W. Bader. Tensor decompositions and applications. *SIAM review*, 51(3):455–500, 2009.

[97] A. Krakovská, J. Jakubík, M. Chvosteková, D. Coufal, N. Jajcay, and M. Paluš. Comparison of six methods for the detection of causality in a bivariate time series. *Physical Review E*, 97(4):042207, 2018.

[98] D.J. Krusienski, D.J. McFarland, and J.R. Wolpaw. Value of amplitude, phase, and coherence features for a sensorimotor rhythm-based brain–computer interface. *Brain research bulletin*, 87(1):130–134, 2012.

[99] S. Kullback. *Information theory and statistics*. Courier Corporation, 1997.

[100] D. La Rocca, P. Campisi, B. Vegso, P. Cserti, G. Kozmann, F. Babiloni, and F. De Vico Fallani. Human brain distinctiveness based on eeg spectral coherence connectivity. *IEEE transactions on Biomedical Engineering*, 61(9):2406–2412, 2014.

[101] M. Lai, M. Demuru, A. Hillebrand, and M. Fraschini. A comparison between scalp-and source-reconstructed eeg networks. *Scientific reports*, 8(1): 1–8, 2018.

[102] M. Le Van Quyen, J. Foucher, J.P. Lachaux, E. Rodriguez, A. Lutz, J. Martinerie, and F.J. Varela. Comparison of hilbert transform and wavelet methods for the analysis of neuronal synchrony. *Journal of neuroscience methods*, 111(2):83–98, 2001.

[103] J. Li, P. Shang, and X. Zhang. Time series irreversibility analysis using jensen–shannon divergence calculated by permutation pattern. *Nonlinear Dynamics*, 96(4):2637–2652, 2019.

[104] V.E. Liong, J. Lu, and G. Wang. Face recognition using deep pca. In *2013 9th International Conference on Information, Communications & Signal Processing*, pages 1–5. IEEE, 2013.

[105] Y. Liu, L. Yang, K. You, W. Guo, and W. Wang. Graph learning based on spatiotemporal smoothness for time-varying graph signal. *IEEE Access*, 7: 62372–62386, 2019.

[106] F. Lotte, M. Congedo, A. Lécuyer, F. Lamarche, and B. Arnaldi. A review of classification algorithms for eeg-based brain–computer interfaces. *Journal of neural engineering*, 4(2):R1, 2007.

[107] F. Lotte, L. Bougrain, A. Cichocki, M. Clerc, M. Congedo, A. Rakotomamonjy, and F. Yger. A review of classification algorithms for eeg-based brain–computer interfaces: a 10 year update. *Journal of neural engineering*, 15(3):031005, 2018.

[108] M.E. Lynall, D.S. Bassett, R. Kerwin, P.J. McKenna, M. Kitzbichler, U. Muller, and E. Bullmore. Functional connectivity and brain networks in schizophrenia. *Journal of Neuroscience*, 30(28):9477–9487, 2010.

[109] L. Maggi, S. Parini, P. Perego, and G. Andreoni. *BCI++: an object-oriented BCI prototyping framework*. Citeseer, 2008.

[110] K. Mahjoory, V.V. Nikulin, L. Botrel, K. Linkenkaer-Hansen, M.M. Fato, and S. Haufe. Consistency of eeg source localization and connectivity estimates. *Neuroimage*, 152:590–601, 2017.

[111] D. Marinazzo, W. Liao, H. Chen, and S. Stramaglia. Nonlinear connectivity by granger causality. *Neuroimage*, 58(2):330–338, 2011.

[112] P.P. Markopoulos, S. Kundu, S. Chamadia, and D.A. Pados. L1-norm principal-component analysis via bit flipping. In *2016 15th IEEE International Conference on Machine Learning and Applications (ICMLA)*, pages 326–332. IEEE, 2016.

[113] P.P. Markopoulos, S. Kundu, S. Chamadia, and D.A. Pados. Efficient l1-norm principal-component analysis via bit flipping. *IEEE Transactions on Signal Processing*, 65(16):4252–4264, 2017.

[114] P.P. Markopoulos, M. Dhanaraj, and A. Savakis. Adaptive l1-norm principal-component analysis with online outlier rejection. *IEEE Journal of Selected Topics in Signal Processing*, 12(6):1131–1143, 2018.

[115] J.D. Medaglia, W. Huang, E.A. Karuza, A. Kelkar, S.L. Thompson-Schill, A. Ribeiro, and D.S. Bassett. Functional alignment with anatomical networks is associated with cognitive flexibility. *Nature human behaviour*, 2(2):156–164, 2018.

[116] J.D. Medaglia, F. Pasqualetti, R.H. Hamilton, S.L. Thompson-Schill, and D.S. Bassett. Brain and cognitive reserve: translation via network control theory. *Neuroscience & Biobehavioral Reviews*, 75:53–64, 2017.

[117] Y. Meirovitch, H. Harris, E. Dayan, A. Arieli, and T. Flash. Alpha and beta band event-related desynchronization reflects kinematic regularities. *Journal of Neuroscience*, 35(4):1627–1637, 2015.

[118] J. Mellinger and G. Schalk. 21 bci2000: A general-purpose software platform for bci. *Toward Brain-Computer Interfacing*, page 359, 2007.

[119] C.M. Michel, M.M. Murray, G. Lantz, S. Gonzalez, L. Spinelli, and R.G. de Peralta. Eeg source imaging. *Clinical neurophysiology*, 115(10):2195–2222, 2004.

[120] K.J. Miller, G. Schalk, E.E. Fetz, M. den Nijs, J.G. Ojemann, and R.P. Rao. Cortical activity during motor execution, motor imagery, and imagery-based online feedback. *Proceedings of the National Academy of Sciences*, 107(9):4430–4435, 2010.

[121] S. Mortaheb, J. Annen, C. Chatelle, H. Cassol, G. Martens, A. Thibaut, O. Gosseries, and S. Laureys. A graph signal processing approach to study high density eeg signals in patients with disorders of consciousness. In *2019 41st Annual International Conference of the IEEE Engineering in Medicine and Biology Society (EMBC)*, pages 4549–4553. IEEE, 2019.

[122] K.R. Müller, M. Tangermann, G. Dornhege, M. Krauledat, G. Curio, and B. Blankertz. Machine learning for real-time single-trial eeg-analysis: from brain–computer interfacing to mental state monitoring. *Journal of neuroscience methods*, 167(1):82–90, 2008.

[123] G. Müller-Putz, R. Leeb, M. Tangermann, J. Höhne, A. Kübler, F. Cincotti, D. Mattia, R. Rupp, K.R. Müller, and J.d.R. Millán. Towards noninvasive hybrid brain–computer interfaces: framework, practice, clinical application, and beyond. *Proceedings of the IEEE*, 103(6):926–943, 2015.

[124] V.N. Murthy and E.E. Fetz. Coherent 25-to 35-hz oscillations in the sensorimotor cortex of awake behaving monkeys. *Proceedings of the National Academy of Sciences of the United States of America*, 89(12):5670, 1992.

[125] A. Natali, M. Coutino, E. Isufi, and G. Leus. Online time-varying topology identification via prediction-correction algorithms. *arXiv preprint arXiv:2010.11634*, 2020.

[126] T.I. Netoff, T.L. Carroll, L.M. Pecora, and S.J. Schiff. 11 detecting coupling in the presence of noise and nonlinearity. *Handbook of Time Series Analysis: Recent Theoretical Developments and Applications*, 2006.

[127] C. Neuper and W. Klimesch. *Event-related dynamics of brain oscillations*, volume 159. Elsevier, 2006.

[128] C. Neuper and G. Pfurtscheller. Event-related dynamics of cortical rhythms: frequency-specific features and functional correlates. *International journal of psychophysiology*, 43(1):41–58, 2001.

[129] M. Newman. Networks: an introduction: Oxford university press, inc. *Nielsen, M., Elmes, G. and Kipyatkov*, 1999, 2010.

[130] F. Nielsen. On a generalization of the jensen-shannon divergence. *arXiv preprint arXiv:1912.00610*, 2019.

[131] G. Nolte, O. Bai, L. Wheaton, Z. Mari, S. Vorbach, and M. Hallett. Identifying true brain interaction from eeg data using the imaginary part of coherency. *Clinical neurophysiology*, 115(10):2292–2307, 2004.

[132] E. Ollila, D.E. Tyler, V. Koivunen, and H.V. Poor. Complex elliptically symmetric distributions: Survey, new results and applications. *IEEE Transactions on signal processing*, 60(11):5597–5625, 2012.

[133] R. Oostenveld, P. Fries, E. Maris, and J.M. Schoffelen. Fieldtrip: open source software for advanced analysis of meg, eeg, and invasive electrophysiological data. *Computational intelligence and neuroscience*, 2011:1, 2011.

[134] G. Orrú, T. Cattai, S. Colonnese, G. Scarano, F. De Vico Fallani, P. Markopoulos, and D. Pados. Deep ll-pca of time-variant data with application to brain connectivity measurements. In *2019 27th European Signal Processing Conference (EUSIPCO)*, pages 1–5. IEEE, 2019.

[135] A. Ortega, P. Frossard, J. Kovačević, J.M. Moura, and P. Vandergheynst. Graph signal processing: Overview, challenges, and applications. *Proceedings of the IEEE*, 106(5):808–828, 2018.

[136] G. Ortiz-Jiménez, M. Coutino, S.P. Chepuri, and G. Leus. Sampling and reconstruction of signals on product graphs. In *2018 IEEE Global Conference on Signal and Information Processing (GlobalSIP)*, pages 713–717. IEEE, 2018.

[137] A. Ozdemir, E.M. Bernat, and S. Aviyente. Recursive tensor subspace tracking for dynamic brain network analysis. *IEEE Transactions on Signal and Information Processing over Networks*, 3(4):669–682, 2017.

[138] H. Padole, S.D. Joshi, and T.K. Gandhi. Early detection of alzheimer's disease using graph signal processing on neuroimaging data. In *2018 2nd European Conference on Electrical Engineering and Computer Science (EECS)*, pages 302–306. IEEE, 2018.

[139] Y. Park and W. Chung. Frequency-optimized local region common spatial pattern approach for motor imagery classification. *IEEE Transactions on Neural Systems and Rehabilitation Engineering*, 27(7):1378–1388, 2019.

[140] R.D. Pascual-Marqui. Coherence and phase synchronization: generalization to pairs of multivariate time series, and removal of zero-lag contributions. *arXiv preprint arXiv:0706.1776*, 2007.

[141] R.D. Pascual-Marqui. Instantaneous and lagged measurements of linear and nonlinear dependence between groups of multivariate time series: frequency decomposition. *arXiv preprint arXiv:0711.1455*, 2007.

[142] E. Pereda, R.Q. Quiroga, and J. Bhattacharya. Nonlinear multivariate analysis of neurophysiological signals. *Progress in neurobiology*, 77(1-2):1–37, 2005.

[143] L. Pessoa. Understanding brain networks and brain organization. *Physics of life reviews*, 11(3):400–435, 2014.

[144] P.C. Petrantonakis and I. Kompatsiaris. Single-trial nirs data classification for brain–computer interfaces using graph signal processing. *IEEE Transactions on Neural Systems and Rehabilitation Engineering*, 26(9):1700–1709, 2018.

[145] M. Petrovic, R. Liegeois, T.A. Bolton, and D. Van De Ville. Community-aware graph signal processing: Modularity defines new ways of processing graph signals. *IEEE Signal Processing Magazine*, 37(6):150–159, 2020.

[146] A. Pezeshki, L.L. Scharf, J.K. Thomas, and B.D. Van Veen. Canonical coordinates are the right coordinates for low-rank gauss–gauss detection and estimation. *IEEE Transactions on Signal Processing*, 54(12):4817–4820, 2006.

[147] G. Pfurtscheller. Spatiotemporal erd/ers patterns during voluntary movement and motor imagery. In *Supplements to Clinical neurophysiology*, volume 53, pages 196–198. Elsevier, 2000.

[148] G. Pfurtscheller. Eeg event-related desynchronization (erd) and synchronization (ers). *Electroencephalography and Clinical Neurophysiology*, 1(103):26, 1997.

[149] G. Pfurtscheller and F.L. Da Silva. Event-related eeg/meg synchronization and desynchronization: basic principles. *Clinical neurophysiology*, 110(11): 1842–1857, 1999.

[150] F. Pichiorri, G. Morone, M. Petti, J. Toppi, I. Pisotta, M. Molinari, S. Paolucci, M. Inghilleri, L. Astolfi, F. Cincotti, et al. Brain–computer interface boosts motor imagery practice during stroke recovery. *Annals of neurology*, 77(5): 851–865, 2015.

[151] B. Picinbono and P. Duvaut. Detection and contrast. In *Stochastic processes in underwater acoustics*, pages 181–203. Springer, 1986.

[152] B. Picinbono. On deflection as a performance criterion in detection. *IEEE Transactions on Aerospace and Electronic Systems*, 31(3):1072–1081, 1995.

[153] B. Picinbono and P. Devaut. Optimal linear-quadratic systems for detection and estimation. *IEEE Transactions on Information Theory*, 34(2):304–311, 1988.

[154] H.V. Poor. *An introduction to signal detection and estimation*. Springer Science & Business Media, 2013.

[155] E.A. Power. Collective ritual and social support networks in rural south india. *Proceedings of the Royal Society B: Biological Sciences*, 285(1879):20180023, 2018.

[156] M.G. Preti, T.A. Bolton, and D. Van De Ville. The dynamic functional connectome: State-of-the-art and perspectives. *Neuroimage*, 160:41–54, 2017.

[157] M. Rabbat, M. Coates, and S. Blouin. Graph laplacian distributed particle filtering. In *2016 24th European Signal Processing Conference (EUSIPCO)*, pages 1493–1497. IEEE, 2016.

[158] S. Ramon-y Cajal, N. Swanson, L.W. Swanson, and R. Guillery. Histology of the nervous system. *Trends in Neurosciences*, 19(4):156–156, 1996.

[159] Y. Renard, F. Lotte, G. Gibert, M. Congedo, E. Maby, V. Delannoy, O. Bertrand, and A. Lécuyer. Openvibe: An open-source software platform to design, test, and use brain–computer interfaces in real and virtual environments. *Presence: teleoperators and virtual environments*, 19(1):35–53, 2010.

[160] A. Roc, L. Pillette, J. Mladenovic, C. Benaroch, B. N'Kaoua, C. Jeunet, and F. Lotte. A review of user training methods in brain computer interfaces based on mental tasks. *Journal of Neural Engineering*, 2020.

[161] D. Romero, V.N. Ioannidis, and G.B. Giannakis. Kernel-based reconstruction of space-time functions on dynamic graphs. *IEEE Journal of Selected Topics in Signal Processing*, 11(6):856–869, 2017.

[162] M.G. Rosenblum, A.S. Pikovsky, and J. Kurths. Phase synchronization of chaotic oscillators. *Physical review letters*, 76(11):1804, 1996.

[163] L. Rui, H. Nejati, and N.M. Cheung. Dimensionality reduction of brain imaging data using graph signal processing. In *2016 IEEE International Conference on Image Processing (ICIP)*, pages 1329–1333. IEEE, 2016.

[164] D. Ruta and B. Gabrys. An overview of classifier fusion methods. *Computing and Information systems*, 7(1):1–10, 2000.

[165] R. Salazar-Varas and D. Gutiérrez. Feature extraction for multi-class bci using eeg coherence. *2015 7th International IEEE/EMBS Conference on Neural Engineering (NER)*, pages 94–97, 2015.

[166] R. Salvador, J. Suckling, M.R. Coleman, J.D. Pickard, D. Menon, and E. Bullmore. Neurophysiological architecture of functional magnetic resonance images of human brain. *Cerebral cortex*, 15(9):1332–1342, 2005.

[167] A. Sandryhaila and J.M. Moura. Discrete signal processing on graphs. *IEEE transactions on signal processing*, 61(7):1644–1656, 2013.

[168] S. Sanei. *Adaptive processing of brain signals*. John Wiley & Sons, 2013.

[169] L. Scharf and B. Van Veen. Low rank detectors for gaussian random vectors. *IEEE Transactions on Acoustics, Speech, and Signal Processing*, 35(11):1579–1582, 1987.

[170] L.L. Scharf. *Statistical signal processing*, volume 98. Addison-Wesley Reading, MA, 1991.

[171] A. Schlögl and C. Brunner. Biosig: a free and open source software library for bci research. *Computer*, 41(10):44–50, 2008.

[172] J. Schrouff, V. Perlbarg, M. Boly, G. Marrelec, P. Boveroux, A. Vanhaudenhuyse, M.A. Bruno, S. Laureys, C. Phillips, M. Pélégrini-Issac, et al. Brain functional integration decreases during propofol-induced loss of consciousness. *Neuroimage*, 57(1):198–205, 2011.

[173] J. Schumacher, C. Jeunet, and F. Lotte. Towards explanatory feedback for user training in brain-computer interfaces. In *2015 IEEE International Conference on Systems, Man, and Cybernetics*, pages 3169–3174. IEEE, 2015.

[174] J. Schürmann. *Pattern classification: a unified view of statistical and neural approaches*. John Wiley & Sons, Inc., 1996.

[175] S. Segarra, S.P. Chepuri, A.G. Marques, and G. Leus. Statistical graph signal processing: Stationarity and spectral estimation. In *Cooperative and Graph Signal Processing*, pages 325–347. Elsevier, 2018.

[176] Y. Shen, B. Baingana, and G.B. Giannakis. Tensor decompositions for identifying directed graph topologies and tracking dynamic networks. *IEEE Transactions on Signal Processing*, 65(14):3675–3687, 2017.

[177] P. Shenoy, M. Krauledat, B. Blankertz, R.P. Rao, and K.R. Müller. Towards adaptive classification for bci. *Journal of neural engineering*, 3(1):R13, 2006.

[178] D.I. Shuman, S.K. Narang, P. Frossard, A. Ortega, and P. Vandergheynst. The emerging field of signal processing on graphs: Extending high-dimensional data analysis to networks and other irregular domains. *IEEE signal processing magazine*, 30(3):83–98, 2013.

[179] R.E. Smith, J.D. Tournier, F. Calamante, and A. Connelly. Sift: Spherical-deconvolution informed filtering of tractograms. *Neuroimage*, 67:298–312, 2013.

[180] S.R. Soekadar, N. Birbaumer, M.W. Slutzky, and L.G. Cohen. Brain–machine interfaces in neurorehabilitation of stroke. *Neurobiology of disease*, 83:172–179, 2015.

[181] L. Song, E. Gordon, and E. Gysels. Phase synchrony rate for the recognition of motor imagery in brain-computer interface. In *Advances in neural information processing systems*, pages 1265–1272, 2006.

[182] M.E. Spencer, R.M. Leahy, J. Mosher, and P. Lewis. Adaptive filters for monitoring localized brain activity from surface potential time series. In *ASILOMAR CONFERENCE ON SIGNALS SYSTEMS AND COMPUTERS*, pages 156–156. COMPUTER SOCIETY PRESS, 1992.

[183] O. Sporns. Graph theory methods: applications in brain networks. *Dialogues in clinical neuroscience*, 20(2):111, 2018.

[184] C.J. Stam, G. Nolte, and A. Daffertshofer. Phase lag index: assessment of functional connectivity from multi channel eeg and meg with diminished bias from common sources. *Human brain mapping*, 28(11):1178–1193, 2007.

[185] P. Strobach, K. Abraham-Fuchs, and W. Harer. Event-synchronous cancellation of the heart interference in biomedical signals. *IEEE transactions on biomedical engineering*, 41(4):343–350, 1994.

[186] S.H. Strogatz. Exploring complex networks. *nature*, 410(6825):268–276, 2001.

[187] Y. Tanaka. Spectral domain sampling of graph signals. *IEEE Transactions on Signal Processing*, 66(14):3752–3767, 2018.

[188] M. Tangermann, K.R. Müller, A. Aertsen, N. Birbaumer, C. Braun, C. Brunner, R. Leeb, C. Mehring, K.J. Miller, G. Mueller-Putz, et al. Review of the bci competition iv. *Frontiers in neuroscience*, 6:55, 2012.

[189] P. Tewarie, L. Liuzzi, G.C. O'Neill, A.J. Quinn, A. Griffa, M.W. Woolrich, C.J. Stam, A. Hillebrand, and M.J. Brookes. Tracking dynamic brain networks using high temporal resolution meg measures of functional connectivity. *Neuroimage*, 200:38–50, 2019.

[190] S. Theodoridis and K. Koutroumbas. Pattern recognition, edition, 2009.

[191] M.C. Thompson. Critiquing the concept of bci illiteracy. *Science and Engineering Ethics*, 25(4):1217–1233, 2019.

[192] L. Torres, A.S. Blevins, D.S. Bassett, and T. Eliassi-Rad. The why, how, and when of representations for complex systems. *arXiv preprint arXiv:2006.02870*, 2020.

[193] V. Trees and L. Harry. *Detection, Estimation, and Modulation Theory-Part l-Detection, Estimation, and Linear Modulation Theory*. John Wiley & Sons New York, 2001.

[194] M. Tumminello, T. Aste, T. Di Matteo, and R.N. Mantegna. A tool for filtering information in complex systems. *Proceedings of the National Academy of Sciences*, 102(30):10421–10426, 2005.

[195] A.L.E. van Delden, C.L.E. Peper, J. Harlaar, A. Daffertshofer, N.I. Zijp, K. Nienhuys, P. Koppe, G. Kwakkel, and P.J. Beek. Comparing unilateral and bilateral upper limb training: the ultra-stroke program design. *BMC neurology*, 9(1):57, 2009.

[196] P. Van Mierlo, M. Papadopoulou, E. Carrette, P. Boon, S. Vandenberghe, K. Vonck, and D. Marinazzo. Functional brain connectivity from eeg in epilepsy: Seizure prediction and epileptogenic focus localization. *Progress in neurobiology*, 121:19–35, 2014.

[197] B. van Wijk, P.J. Beek, and A. Daffertshofer. Neural synchrony within the motor system: what have we learned so far? *Frontiers in human neuroscience*, 6:252, 2012.

[198] V.M. Vergara, R. Miller, and V. Calhoun. An information theory framework for dynamic functional domain connectivity. *Journal of neuroscience methods*, 284:103–111, 2017.

[199] C. Vidaurre and B. Blankertz. Towards a cure for bci illiteracy. *Brain topography*, 23(2):194–198, 2010.

[200] C. Vidaurre, C. Sannelli, K.R. Muller, and B. Blankertz. Co-adaptive calibration to improve bci efficiency. *Journal of neural engineering*, 8(2):025009, 2011.

[201] A. Vinayagam, T.E. Gibson, H.J. Lee, B. Yilmazel, C. Roesel, Y. Hu, Y. Kwon, A. Sharma, Y.Y. Liu, N. Perrimon, et al. Controllability analysis of the directed human protein interaction network identifies disease genes and drug targets. *Proceedings of the National Academy of Sciences*, 113(18):4976–4981, 2016.

[202] U. Von Luxburg. A tutorial on spectral clustering. *Statistics and computing*, 17(4):395–416, 2007.

[203] H.E. Wang, C.G. Bénar, P.P. Quilichini, K.J. Friston, V.K. Jirsa, and C. Bernard. A systematic framework for functional connectivity measures. *Frontiers in neuroscience*, 8:405, 2014.

[204] J. Wang, D.B. Aydogan, R. Varma, A.W. Toga, and Y. Shi. Topographic regularity for tract filtering in brain connectivity. In *International Conference on Information Processing in Medical Imaging*, pages 263–274. Springer, 2017.

[205] Q. Wei, Y. Wang, X. Gao, and S. Gao. Amplitude and phase coupling measures for feature extraction in an eeg-based brain–computer interface. *Journal of Neural Engineering*, 4(2):120, 2007.

[206] P. Welch. The use of fast fourier transform for the estimation of power spectra: a method based on time averaging over short, modified periodograms. *IEEE Transactions on audio and electroacoustics*, 15(2):70–73, 1967.

[207] J. Wolpaw, J.R. Millán, and N. Ramsey. Brain-computer interfaces: Definitions and principles. *Handbook of clinical neurology*, 168:15–23, 2020.

[208] J. Wolpaw and E.W. Wolpaw. *Brain-computer interfaces: principles and practice*. OUP USA, 2012.

[209] J.R. Wolpaw, N. Birbaumer, D.J. McFarland, G. Pfurtscheller, and T.M. Vaughan. Brain–computer interfaces for communication and control. *Clinical neurophysiology*, 113(6):767–791, 2002.

[210] J.R. Wolpaw, D.J. McFarland, T.M. Vaughan, and G. Schalk. The wadsworth center brain-computer interface (bci) research and development program. *IEEE Transactions on Neural Systems and Rehabilitation Engineering*, 11(2):1–4, 2003.

[211] K. Yamada, Y. Tanaka, and A. Ortega. Time-varying graph learning based on sparseness of temporal variation. In *ICASSP 2019-2019 IEEE International Conference on Acoustics, Speech and Signal Processing (ICASSP)*, pages 5411–5415. IEEE, 2019.

[212] K. Yamada, Y. Tanaka, and A. Ortega. Time-varying graph learning with constraints on graph temporal variation. *arXiv preprint arXiv:2001.03346*, 2020.

[213] V. Youssofzadeh, G. Prasad, M. Naeem, and K. Wong-Lin. Partial granger causality analysis for brain connectivity based on event related potentials. In *Front. Neuroinform. Conference Abstract: Neuroinformatics 2013*, number 114, 2013.

[214] H. Yuan and B. He. Brain–computer interfaces using sensorimotor rhythms: current state and future perspectives. *IEEE Transactions on Biomedical Engineering*, 61(5):1425–1435, 2014.

[215] J.H. Zar. *Biostatistical analysis*. Pearson Education India, 1999.

[216] Y. Zhang, D.H. Brooks, M.A. Franceschini, and D.A. Boas. Eigenvector-based spatial filtering for reduction of physiological interference in diffuse optical imaging. *Journal of biomedical optics*, 10(1):011014, 2005.